Cell and nuclear packing during tissue growth

Dominik Schienstock

Imperial College London, Crick Doctoral Centre

Thesis submission for MPhil in Biology

September 2017

Declaration of originality

I hereby certify that this thesis contains my own work. Experimental and intellectual work from others is referenced accordingly.

Copyright declaration

The copyright of this thesis rests with the author and is made available under a Creative Commons Attribution Non-Commercial No Derivatives licence. Researchers are free to copy, distribute or transmit the thesis on the condition that they attribute it, that they do not use it for commercial purposes and that they do not alter, transform or build upon it. For any reuse or redistribution, researchers must make clear to others the licence terms of this work.

Abstract

Highly proliferative tissues require an optimal cellular organisation to use the available space most effectively. One such organisation is pseudostratification, where cells are tightly packed within a monolayer and their nuclei stack on top of each other. This cellular packing enables, for example, the production of numerous neurons in the brain. Although high proliferation is desired, growth needs to terminate eventually. The mechanisms of growth termination are however complex and largely unknown.

The distal part of the *Drosophila* wing imaginal disc, which gives rise to the adult wing blade, is a model for growth of pseudostratified epithelia. In this tissue, mechanical compression of the apical domain was proposed to cause growth termination. Crucially, nuclei have to undergo apical migration for mitosis. Thus, the packing of nuclei might mechanically influence growth as well. My aim was therefore to quantify nuclei packing (density, volume and position) on a tissue wide scale at different growth stages.

An imaging pipeline and a complementary user-guided segmentation program were developed to quantify nuclear packing. The thick and highly folded shape of the wing imaginal disc was preserved and imaged using agarose embedding and a tissue clearing solution, respectively. The nuclear envelope served as a marker to extract 2D shapes which were merged as 3D objects and manually corrected. Local averaging of tiled segmented images was used to compare nuclear parameters of mid and late developmental stages. The analysis indicated that nuclei moved closer together and packed more volume in the available space.

My hypothesis is that this close packing of nuclei could contribute to growth termination. While the developed imaging and segmentation pipeline was optimised to extract nuclear parameters, it could also be utilised for other tightly packed tissues, such as tumour spheroids, to extract cells in 3D.

Table of Contents

List of Tables **6**

List of Figures **7**

Abbreviations **9**

1. Introduction **10**

1.1. Role of nuclear movement during growth of pseudostratified epithelia 12

1.2. Rules of cell packing 14

1.3. Cell packing in the wing imaginal disc 15

1.4. Imaging and segmentation of thick tissue samples 16

1.5. Biological motivation and project aims 18

2. Materials and Method **19**

2.1. Fly stocks 19

2.2. Larvae staging 19

2.3. Antibody staining 19

2.4. Wing imaginal disc dissection, mounting, and clearing 20

2.5. Confocal microscopy 20

2.6. Main classes of image segmentation 21

2.7. Defining the region of interest 22

2.8. Defining the processing parameters 22

2.9. Merging labels and filtering nuclei 23

2.10. Correcting nuclei 25

2.11. Quantifying segmented nuclei 30

3. Results **31**

3.1. Preserving tissue shape during preparation 31

3.2. Nuclei staining was optimised 33

3.3. Time course under optimal mounting conditions 36

3.4. Optimisation of segmentation parameters 38

3.5. Nuclear segmentation 42

3.6. Quantification of nuclei packing 43

4. Discussion **52**

4.1. Nuclear volume has to be normalised 53

4.2. The need for a topographical marker 54

4.3. Estimating nuclei shape 55
4.4. Stacking could limit proliferation efficiency 56
4.5. Confocal imaging and tissue clearing have limitations 58
4.6. Strengths and weaknesses of the segmentation 59
4.7. Conclusions 60

5. References 61

6. Supplementary information 67

6.1. Sequence for Tubulin-Myristoylated-mCherry-2A-Citrine-Lamin 69
6.2. Code 70
6.3. Morphological features of moulting 80
6.4. Images 81

List of Tables

Table 1: Overview of tissue height, nuclei stacking and proteins involved in interkinetic nuclear migration (IKNM).....12

List of Figures

Figure 1: Tissues with pseudostratified epithelia.....11
Figure 2: Main classes for NucleoSegment. 21
Figure 3: User interface to define the input file and its channels and region of interest. 22
Figure 4: Defining processing steps.....23
Figure 5: Filtering labels.....24
Figure 6: Filtering merged nuclei. 25
Figure 7: Deleting nuclei not in the region of interest. 26
Figure 8: Deleting non-nuclei. 27
Figure 9: Checking nuclei in the gallery mode. 28
Figure 10: Detection and correction of segmentation errors. 28
Figure 11: Segmentation as TIFF file in Fiji. 29
Figure 12: Quantification of segmentation by tiling combination. 30
Figure 13: Nuclei appeared to increase in density and decrease in smoothness during growth. 32
Figure 14: Preserving tissue shape. 33
Figure 15: Increasing triton concentration resulted in a uniform Lamin staining. 34
Figure 16: Construct enabled simultaneous imaging of nuclei and membrane. 35
Figure 17: FocusClear enabled a homogenous signal along the apical-basal axis. 35
Figure 18: Developed imaging pipeline. 36
Figure 19: Time-course of wing imaginal disc growth with established protocol. 37
Figure 20: Segmentation workflow. 38
Figure 21: Testing parameters for morphological filters. 40
Figure 22: Typical correction for nuclei. 41
Figure 23: Segmentation for tested regions. 41
Figure 24: Segmented nuclei from time-course. 42
Figure 25: Examples of missed and excluded nuclei. 43
Figure 26: Total nuclei volume increases. 45
Figure 27: Nuclei volume fraction increased. 46
Figure 28: (previous page) Total nuclei volume per stacking height increased. 48
Figure 29: Contact of nuclei for 5 days A. 48
Figure 30: Nuclei contact increased. 49
Figure 31: Nuclei volume was independent of apical distance. 50

Figure 32: Contact was independent of apical distance. 51
Figure 33: Nuclei pack uniformly closer during growth. 53

Abbreviations

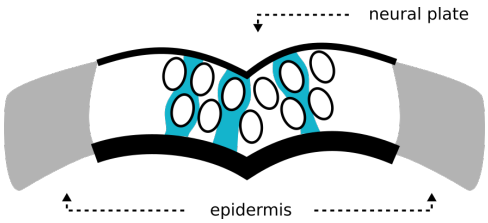
Abbreviation	Description
BSA	Bovine serum albumin
CDK1	Cyclin-dependent kinase 1
dAEL	Days after egg laying
DAPI	4',6-diamidino-2-phenylindole
Dpp	Decapentaplegic
IKNM	Interkinetic nuclear migration
PBS	Phosphate-buffered saline
RACE	Real-time Accurate Cell-shape Extractor
TAG-1	Transient axonal glycoprotein–1

1. Introduction

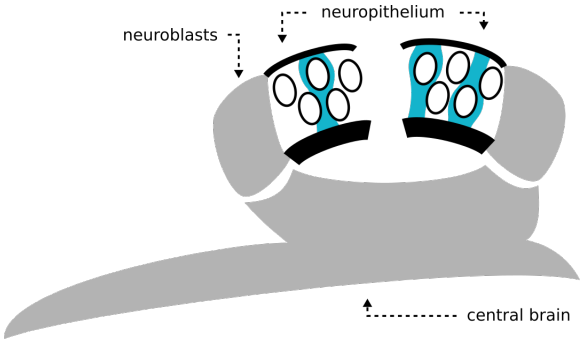
Tissues with large surface areas, such as the brain, require numerous progenitor cells. To produce this large number, cells have to pack tightly together to optimise the use of space. The tight packing is evident from their pseudostratified organisation where nuclei stack on top of each other while maintaining a single monolayer. This conformation was proposed to increase the number of cell divisions per surface area (Miyata et al., 2014). Nuclei within this tissue organisation undergo apical migration during division, termed interkinetic nuclear migration (IKNM) (Strzyz et al., 2016). The reason for apical division is not known (Norden, 2017); however, it is crucial to preserve tissue integrity (Baffet et al., 2015, Okamoto et al., 2013, Strzyz et al., 2015). Optimal packing of nuclei must therefore support these cell cycle dynamics to use the available space most effectively. How nuclear packing is organised on a tissue-wide scale is largely unknown; yet, descriptive and functional studies in different species and tissues indicate a functional organisation of cells to support efficient growth (Fish et al., 2008, Sauer, 1935, Smart, 1972b).

Different forms of pseudostratified epithelia exist (Figure 1). Most studies focussed on nuclear dynamics within progenitors of neural tissues. For example, the neural plate gives rise to the neural tube, the precursor for the central nervous system (Sauer, 1935). The optic lobe of *Drosophila* (Rujano et al., 2013) and the neural epithelium of zebrafish and mice (Okamoto et al., 2013, Strzyz et al., 2015) give rise to the adult eye. The purpose of these tissues is to produce as many neurons as possible to optimise signal processing. Cells of the distal region of the *Drosophila* wing imaginal disc, called the pouch, also need to proliferate as much as possible to produce as much mass as possible (Meyer et al., 2011). This tissue eventually undergoes a dramatic eversion to form the adult wing blade (Aldaz et al., 2010).

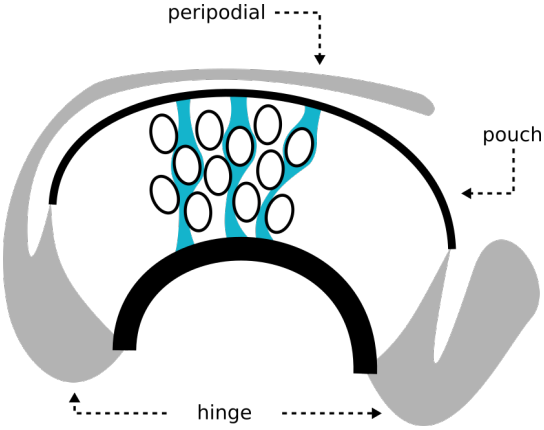
a) Quail neural plate



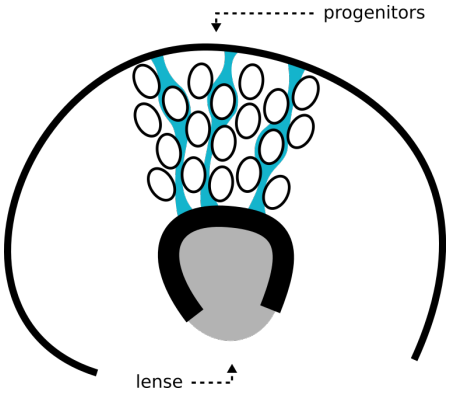
b) *Drosophila* optic lobe



c) *Drosophila* wing imaginal disc



d) Zebrafish neuroepithelium



e) Mouse/Ferret neuroepithelium

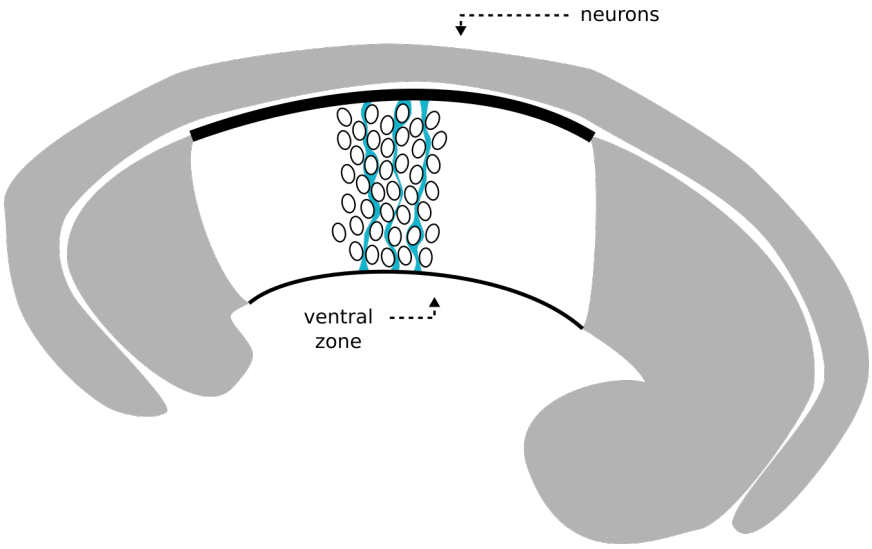


Figure 1: Tissues with pseudostratified epithelia. Basal side drawn thicker than apical side. Cytoplasm in turquoise and nucleus outlined in black. a) Mouse/Quail neural plate (Schoenwolf and Alvarez, 1989). b) *Drosophila* optic lobe (Rujano et al., 2013). c) *Drosophila* wing imaginal disc (Meyer et al., 2011). d) Zebrafish neuroepithelium (Weber et al., 2014). e) Mouse/Ferret neuroepithelium (Miyata et al., 2014, Nagasaka et al., 2016, Okamoto et al., 2014). Not drawn to scale.

1.1. Role of nuclear movement during growth of pseudostratified epithelia

The purpose of pseudostratified tissues is to use their limited space most productively. Different molecular machines are used to drive cell division depending on the thickness of the tissue (Table 1). The *Drosophila* optic lobe (Rujano et al., 2013) and mouse neural plate (Sauer, 1935) are approximately 20-30μm thick and have 2-3 nuclei layers. In these tissues, actomyosin contraction is sufficient for apical cell division (Strzyz et al., 2016). When basal myosin contraction was inhibited in the *Drosophila* optic lobe (Rujano et al., 2013), nuclei division was disrupted and resulted in loss of tissue integrity. In thicker tissues, such as the zebrafish neural epithelium (Strzyz et al., 2015) or the mouse intestine (Grosse et al., 2011), the number of nuclei layers is higher with 4-5. Again, actomyosin contraction was proposed to be the primary force to push nuclei to the apical domain (Strzyz et al., 2016).

In even thicker tissues of up to 100μm, such as the mouse neural epithelium, IKNM is a two-step process (Spear and Erickson, 2012). Nuclei are pulled by the minus-end directed microtubule motor dynein up to 50μm to the apical domain and the last 50μm are facilitated by actomyosin contraction. When inhibiting dynein with Colcemid, nuclei were not able any more to reach the top, whereas inhibition of myosin with Chytochalasin B still allowed apical migration but cells failed to divide (Spear and Erickson, 2012).

Table 1: Overview of tissue height, nuclei stacking and proteins involved in interkinetic nuclear migration (IKNM). Examples taken from (Strzyz et al., 2016). (*) In the neocortex, nuclei stack within the first 150μm of the apical tissue domain.

Species	Tissue	Height (μm)	Layers	IKNM	Reference
Quail	Neural plate	20-30	2-3	Actomyosin contraction	(Schoenwolf and Alvarez, 1989)
Fly	Optic lobe				(Rujano et al., 2013)
Mouse	Neural tube	30-59	4-5	Actomyosin contraction	(Smart, 1972b)
Zebrafish	Neural epithelium				(Strzyz et al., 2015)
Mouse	Intestine				(Grosse et al., 2011)
Fly	Imaginal discs				(Meyer et al., 2011)
Mouse	Neural tube	Up to 100	>= 8	Dynein pulling and actomyosin contraction	(Spear and Erickson, 2012)
	Neural epithelium				(Okamoto et al., 2013)
Ferret	Neural epithelium				(Okamoto et al., 2014, Nagasaka et al., 2016)
Mouse	Neocortex/radial glia	> 1,000s	> 10*	Dynein pulling	(Taverna and Huttner, 2010)

In the ferret neural epithelium, nuclei stacking and tissue thickness is even higher (Okamoto et al., 2014). There, after the first tissue region, termed ventricular zone, is fully packed with cells, progenitor cells enter the next region, termed outer subventricular zone, to continue to proliferate (Okamoto et al., 2014). Mouse and ferret neural epithelia also show different dynamics of IKNM and subapical nuclei density. While apical nuclei migration is more directional than basal migration in mouse neural epithelial cells, it is the reverse in ferrets (Okamoto et al., 2014, Nagasaka et al., 2016). Subapical nuclear density in ferrets is also decreased compared to mouse neural epithelia; yet, apical stiffness is increased as measured by atomic force microscopy (Nagasaka et al., 2016). Therefore, increasing tissue thickness correlates with increasing nuclei stacking and altered cell cycle dynamics. The causality between these measures remains however contested. Nevertheless, it is reasonable to propose that optimal packing might increase the efficiency of tissue productivity.

In the zebrafish (Leung et al., 2011, Strzyz et al., 2015) and rat (Baffet et al., 2015, Hu et al., 2013) neural epithelium, apical migration is linked to the cell cycle. CDK1 (Cyclin-dependent kinase 1) phosphorylates nuclear envelope proteins which enable docking of dynein and dynactin. Subsequently, the nucleus moves apically via the minus-end directed microtubule motor dynein (Baffet et al., 2015, Hu et al., 2013). Conversely, while apical migration is important to enable division, nuclei have to clear the apical area to avoid congestion. Nuclei clearance from the apical domain was suggested to be facilitated by passive nuclei displacement (Strzyz et al., 2015) and also by the plus-end directed microtubule motor kinesin (Okamoto et al., 2013).

During mitosis in the mouse neural epithelium, cells lose their basal contact. After division, one daughter cell regains the contact earlier than the other; a mechanism likened to “priority boarding” (Okamoto et al., 2013). The former will lead the way to the basal side while the latter follows (Baffet et al., 2015, Okamoto et al., 2013). Inhibition of this mechanism, by genetic deletion of Transient axonal glycoprotein–1 (TAG-1), a basal membrane associated anchor protein required for basal-ward movement, caused overcrowding (Okamoto et al., 2013). Incoming wildtype cells, not able to reach the apical side, delaminated or prematurely differentiated into neurons (Okamoto et al., 2013). While the cell cycle dynamics have been well studied in various tissues and species, nuclei packing has not been quantified on a tissue-wide scale during development.

1.2. Rules of cell packing

Tissue integrity in epithelial tissues is crucially dependent on apical-basal polarity. For example, the characteristic columnar organisation of the cellularised *Drosophila* embryo is severely disrupted by a mutation in the apical transmembrane protein Crumbs; the columnar structure of the developing embryo changes to a highly disorganised epithelium with cells stacking on top of each other (Knust et al., 1993). In pseudostratified epithelia, nuclei stack on top of each other while still maintaining an epithelial monolayer. How nuclei pack in these tissues to maintain tissue integrity and to enable IKNM during division is not known.

The limiting factor for tight cell packing in pseudostratified epithelia is the bulky nucleus (Miyata et al., 2014, Strzyz et al., 2016). Packing of nuclei like soap bubbles (Kraynik et al., 2003) is unlikely as the cell membranes separate nuclei from each other and the cytoskeleton gives structural support to the cell and its organelles (Norden, 2017). How nuclei pack within these tissues has been of interest since the 1930s where Sauer (1935) analysed nuclei shapes within the chick neural tube. In the 1970s, Smart (1972b) carefully examined nuclei stacking and shapes in the developing mouse neural tube. These initial observations suggested, that nuclei stack, on average, into column-like structures. The size of a mitotic cell at the top and the time required for the cell cycle might determine the optimal number of nuclei and layers that can be accommodated without wasting space or causing congestion (Fish et al., 2008). In theory, the more nuclei layers, the longer the cell cycle and, conversely, the shorter the cell cycle, the less layers.

Crucial to this thought is that the number of layers depends on the number of nuclei that fit beneath one mitotic cell. If mitotic cells in a tissue were twice as big than interphase nuclei, the optimal number of layers would be higher compared to a tissue with bigger mitotic cells (Strzyz et al., 2016). The number of layers compared to this optimum might give an indication of the proliferative state of the tissue. Tissues with less layers than optimal would be able to continue to proliferate, while tissues with more layers might slow down their cell cycle to prevent overcrowding (Strzyz et al., 2016). Cells of the telencephalon, for example, start to divide basally and produce neurons once the optimal number of layers is reached (Fish et al., 2008). Theoretically, in wing imaginal discs, which undergo eversion at the end of the third larval instar (Aldaz et al., 2010), cells could stop proliferation once their maximum proliferation efficiency is reached and start further morphogenetic processes.

1.3. Cell packing in the wing imaginal disc

Live cell imaging studies of IKNM in the wing imaginal disc have so far been limited due to restricted culturing conditions (Strassburger et al., 2017). Despite this limitation, many studies focussed on the apical cell area where adherens junctions reside (Aegerter-Wilmsen et al., 2012, Mao et al., 2013) and the main stress sensors, such as the Hippo pathway (Aegerter-Wilmsen et al., 2007), are located. Theoretical (Shraiman, 2005) and experimental studies (Pan et al., 2016) proposed that mechanical compression in the centre of the pouch could lead to decreased proliferation. These studies were supported by measurements of decreasing apical cell area in the centre of the pouch (Aegerter-Wilmsen et al., 2012, Mao et al., 2013). Reduced growth rate at the edge compared to cells in the centre could result in compression. These changes were shown to correlate with myosin accumulation in the middle of the cell's apical domain which induced Hippo signalling and decreased growth (Pan et al., 2016). The apical cell area might also be related to the height of a cell (Miyata et al., 2014).

The height of the cells in the pouch has been proposed to depend on the morphogen Decapentaplegic (Dpp) which is expressed along the anterior-posterior axis (Widmann and Dahmann, 2009). Dpp was proposed to activate the small GTPase Rho1 which in turn shifted the activity of the non-muscle myosin II regulatory light chain from lateral to apico-lateral sides (Widmann and Dahmann, 2009). This shift resulted in increasing myosin contraction and cell lengthening. Cells still appeared pseudostratified (Widmann and Dahmann, 2009); yet, the authors did not comment or investigate the packing of nuclei within this tissue. Cell height therefore seems to be linked to the contraction state of the cell. How nuclei are affected by this increasing constriction has not been addressed.

In vitro studies showed that compressed nuclei increased in heterochromatin and decreased in division (Versaevel et al., 2012). Nuclei could therefore be *in situ* sensors of mechanical stress (Cho et al., 2017), akin to synthetic oil-droplet based methods (Campas et al., 2014). Therefore, the shape of nuclei, which was originally proposed to change over the course of the cell cycle (Sauer, 1935, Smart, 1972a), could serve as a readout for compression (Rohde et al., 2008). Additionally, accumulation of the nuclear envelope protein Lamin was proposed to correlate with cellular stresses (Philip and Dahl, 2008). Therefore, individual nuclei shapes and stacking on a tissue-wide scale might correlate with the cell cycle, apical cell area and tissue thickness.

Although nuclei shapes have not been investigated in 3D, there is a growing interest to characterise nuclei in the study of cancer (Zink et al., 2004). Nuclei morphology is often

disrupted in cancer cells and their aberrant shapes, which are associated with specific disease types, are used for diagnostics (Zink et al., 2004). Several computational approaches have been proposed to aid manual scoring by clinicians (Gardner et al., 2005, Lesty et al., 1989, Verschuuren et al., 2017). HeLa cells, for example, were scored for their bending and elongation of nuclei to calculate shape changes (Rohde et al., 2008) which were also correlated with cell shape changes (Johnson et al., 2015). Using such an approach, Verschuuren et al. (2017) classified nuclei according to their morphology. In this study, machine learning algorithms were used to score nuclei for their dysmorphy in order to detect aberrant shapes in tissue samples (Verschuuren et al., 2017). Such algorithms could aid clinicians to diagnose patients more efficiently and effectively (Meaburn, 2016, Verschuuren et al., 2017).

Similarly, nuclei deformation in pseudostratified epithelia could be occurring in situations of increasing cell density, as observed in the ferret neural epithelium (Okamoto et al., 2014), and during IKNM (Sauer, 1935). To investigate this possibility, high resolution images of the whole tissue have to be obtained; however, the wing imaginal disc has a considerable thickness (Meyer et al., 2011) which makes imaging difficult (Richardson and Lichtman, 2015) and most segmentation methods are based on 2D segmentation of the apical cell area (Heller et al., 2016).

1.4. Imaging and segmentation of thick tissue samples

Thick tissues have high light scattering properties (Richardson and Lichtman, 2015). Tissues, such as the mouse (Chung et al., 2013), zebrafish (Hildebrand et al., 2017) or fly (Zheng et al., 2017) brain have been imaged and their neurons mapped; however, often manually. Thick mouse brains were imaged by hydrogel embedding for structural support which allowed the removal of lipids (Chung et al., 2013). Thus, tissue sectioning was not needed and the brain was imaged as a whole using light microscopy. An alternative approach combined electron microscopy with serial sectioning which provided a high resolution and enabled imaging of the whole sample. Though this approach is laborious to gain high resolution images, it was successfully used to map the zebrafish (Hildebrand et al., 2017) and fly (Zheng et al., 2017) brain. The combination of electron and light microscopy also provided high resolution images while enabling labelling of, for example, specific neuronal subtypes (Zheng et al., 2017). Other approaches focused on imaging slices while serial sectioning was performed using light (Osten and Margrie, 2013) or electron (Russell et al., 2017) microscopy. These approaches remove the requirement of error-prone manual section alignment.

While deep imaging approaches are constantly being developed with increasing resolution and depth (Power and Huisken, 2017), these are often home-built solutions. A big challenge is also the subsequent data analysis. Most studies focussed on 2D segmentation in the wing imaginal disc (Heller et al., 2016). While these approaches were used to extract apical cell areas and dynamic cell movements (Etournay et al., 2016, Julicher and Eaton, 2017), they cannot accommodate 3D information. Several approaches have been developed to extract cells in 3D (Khan et al., 2014, Stegmaier et al., 2016). These are however based on big cells in embryos which are more amenable to segmentation compared to tightly packed cells of pseudostratified epithelia. Machine learning algorithms (Kreshuk et al., 2011) were also utilised to detect, for example, synapses in electron microscopy samples (Kreshuk et al., 2014) and cells of the developing *Drosophila* embryo (Fabrowski et al., 2013). Segmentation programs are also mostly purpose-built to provide, for example, fast real-time segmentation (Stegmaier et al., 2016) or carefully curated segmentation (Hildebrand et al., 2017). A major caveat with all these segmentation methods is the need for validation and correction. In most instances, the resulting segmentation requires manual correction (Heller et al., 2016). Therefore, although various tools and techniques are available for segmentation, their use is mostly restricted to specific applications and scientific questions.

For example, the shoot apical meristem of plants (Beauzamy et al., 2015) has an overall similar tissue shape to wing imaginal discs (Meyer et al., 2011). Flowers and leaves bud from the meristem, which was likened to a shell under pressure (Beauzamy et al., 2015). Superficially, this process could resemble the eversion of the wing imaginal disc (Aldaz et al., 2010). Further, the developing flower buds of the meristem could also represent a limiting structure for cell growth (Beauzamy et al., 2015) as proposed for the pouch of the wing imaginal disc (Hariharan, 2015). Different segmentation approaches have been developed to extract 3D cell shapes in the plant meristem (Barbier de Reuille et al., 2015, Chakraborty et al., 2013) and to study the effect of cell packing changes on growth in time (Jones et al., 2017). One such approach was employed to quantify cell shape changes in the wing imaginal disc (Aegerter-Wilmsen et al., 2012, Barbier de Reuille et al., 2015). Although both tissues are structurally similar, the same segmentation program could not be used to extract 3D cell shapes from both tissues. Plant cells are readily discernible by their rigid cell wall, which cells of the wing imaginal disc lack. Therefore, the 3D shape information could only be used to account for the curved surface of the wing imaginal disc and the authors focussed on measurements of the apical cell area (Aegerter-Wilmsen et al., 2012). Other examples of shape reconstruction include EDGE4D (Khan et al., 2014) and Real-time Accurate Cell-shape Extractor (RACE)

(Stegmaier et al., 2016) which focus on columnar cells in the *Drosophila* embryo. Again, these cells are readily discernible compared to cells of wing imaginal discs.

1.5. Biological motivation and project aims

Sauer (1935) and Smart (1972b) carefully mapped the shape and stacking of nuclei by hand in the chick neural tube and mouse neural epithelia respectively. Their illustrations highlight that nuclei change their shape during the cell cycle, appearing like tear-drops (Sauer, 1935), and are, on average, arranged into column-like structures (Smart, 1972b). In the wing imaginal disc specifically, increasing cell compression was proposed to occur (Aegerter-Wilmsen et al., 2012, Mao et al., 2013) during its development into a highly folded tissue (Meyer et al., 2011). In this context, it is interesting to note that confined mammalian tissue culture cells showed compression of nuclei which increased heterochromatin and decreased cell proliferation (Versaevel et al., 2012). Studies of neural epithelia highlighted the importance of nuclei stacking for growth and the cell cycle (Miyata et al., 2014, Strzyz et al., 2015). Displacement of nuclei was proposed to be facilitated by apically migrating mitotic cells (Strzyz et al., 2016). Also, studies in tissue culture cells highlighted the exertion of significant forces onto the immediate environment during mitotic rounding (Sorce et al., 2015).

This project aimed to consolidate these observations and proposals by mapping nuclei packing (density, volume and position) on a tissue-wide scale using the pouch of the *Drosophila* wing imaginal disc as a model for tightly packed pseudostratified epithelia. The challenge was to maintain the highly folded tissue structure while enabling high-resolution imaging for subsequent segmentation and feature extraction. Because most segmentation programs are purpose-built, the challenge was to adapt available frameworks to enable segmentation and to provide an interface for correction and validation.

2. Materials and Method

2.1. Fly stocks

Tubulin-Myristoylated-mCherry and Tubulin-Gal4 > UAS-CD8-GFP flies were used for the initial time-course and to test the mounting strategy and anti-Lamin staining protocol. Tubulin-Myristoylated-mCherry-2A-Citrine-Lamin (annotated sequence in Supplementary Information 6.1) flies were created using a tubulin promoter SV40 vector and standard molecular cloning with subsequent injection into *w118* flies and balancing with TM3.

2.2. Larvae staging

Small dishes with grape juice and a drop of baker's yeast or melted standard fly food were used to collect eggs from around 50 flies in a cage. Food dishes were changed every 2 hrs and kept in box with wet towels at 25°C. Larvae were selected for L2-L3 moult after 72 hrs by morphological features (small "fists" anterior and faint yellow shadow posterior; Supplementary Figure 1), transferred to a new food plate and either dissected directly (3 days after egg laying (dAEL)) or stored as before and dissected after 24 hrs (4 dAEL) or 48 hrs (5 dAEL).

2.3. Antibody staining

Staged larvae, usually 10-12, were inverted in cold PBS and fixed with 3.7% Formaldehyde for 20 min in dark on shaker. Samples were washed twice with PBT (Phosphate buffered saline (PBS) and 0.5% Triton) and kept on shaker for 30 min. Samples were washed with PBTB (PBT and 2% Bovine serum albumin (BSA)) and kept on shaker for 15 min. Primary antibody against Lamin (1:200, ADL67.10-s or ADL84.12-s, DSHB) was added to the samples and kept in dark on shaker at 4°C overnight.

Samples were washed four times with PBT for 15 min. Secondary antibody anti-mouse 488 (1:1000, ab150105, Abcam) and 4',6-diamidino-2-phenylindole (DAPI; 1:1000) were added and samples were kept at room temperature on shaker for 2-3 hrs or overnight at 4°C in dark. Samples were washed four times in PBS and kept at 4°C until dissected.

2.4. Wing imaginal disc dissection, mounting, and clearing

Wing imaginal discs from inverted larvae were dissected with forceps in PBS. Dissected wing imaginal discs were mixed in low melting point agarose (1%), transferred in 10µl onto a coverslip (631-0136, VWR) and adjusted with a fine tungsten needle to position the apical side of the pouch facing the coverslip. Each agarose drop was surrounded with high-vacuum silicone grade grease (Z273554-1EA, Dow Corning).

10µl FocusClear (F101-KIT, CellExplorer) was transferred to each drop and kept in a box with wet towels at room temperature for 1hr to allow tissues to clear. FocusClear was replaced by 10µl MountClear (F101-KIT, CellExplorer). The coverslip was inverted, placed on a microscope slide and the edges sealed with grease to prevent evaporation. Samples were kept at 4°C until imaged.

Where indicated, wing imaginal discs were instead embedded in gelatin albumin and sectioned (40µm) with a vibratome. Sections were mounted using Vectashield (H-1200, Vector Laboratories). Alternatively, dissected wing imaginal discs were mounted with two layers of tape or 250µm gelatinin albumin spacers and mounted in Vectashield or mounted in a drop of Vectashield on a coverslip coated with poly-lysine.

2.5. Confocal microscopy

Samples were imaged on Leica TCS SP5 with 20x immersion (1.0 NA) or 63x glycerol (1.3 NA) objectives with oil or Immersion Solution-M (F101-KIT, CellExplorer), 12 bits per pixel, 4 line averages, scanning speed 400Hz, bidirectional scan and voxel size of 240x240x500nm.

2.6. Main classes of image segmentation

A user-guided segmentation program was developed to segment and correct nuclei. The program was developed and tested on a standard laptop (MacBook Pro, 2.2GHz Intel Core i7, 16GB DDR3 RAM) with Python 3.5.1 and PyCharm Edu 3.0.1.

The program was divided into three main components for processing the images, storing the data and providing a user interface (Figure 2). "Segmentation" was the main class, holding all information regarding a specific segmentation. The program code and tutorial is accessible through Github (github.com/baemms/NucleoSegment).

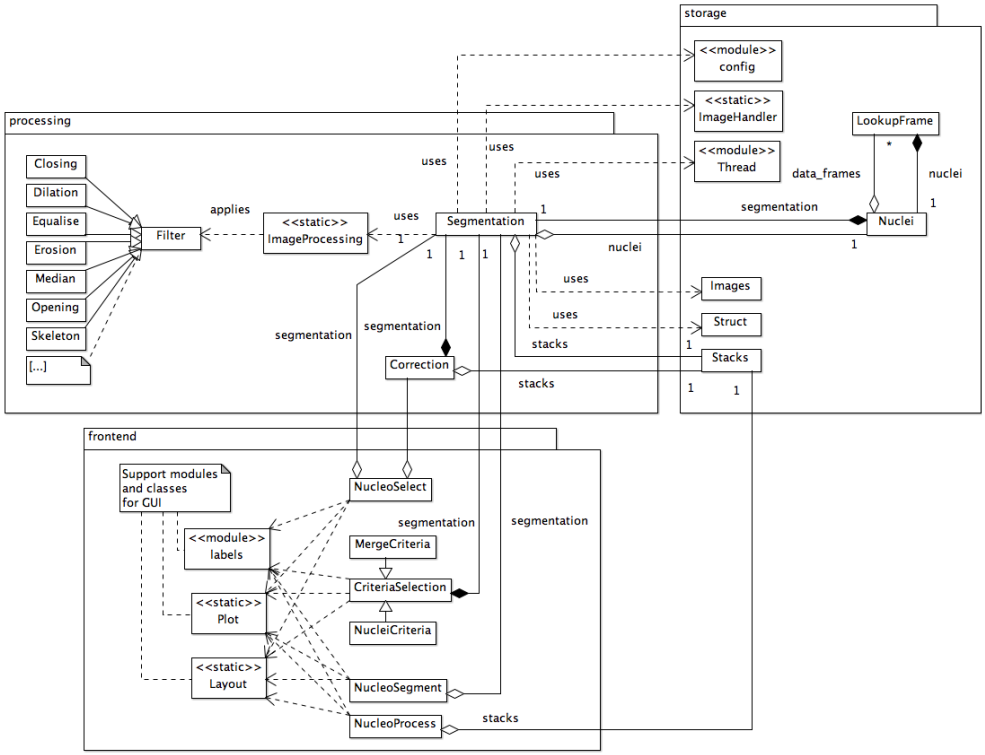


Figure 2: Main classes for NucleoSegment. "Segmentation" was the main class from which all other classes were accessed. "ImageProcessing" was a static class providing all functions to process images. "Nuclei" stored nuclei in "LookupFrame" which used Pandas data-frames. "Correction" organised corrections made to nuclei in lists which were stored as Python objects using "pickle". All classes in "frontend" used Qt to provide a user interface.

2.7. Defining the region of interest

The segmentation was started from “nucleo_segment.py” with an array to define the desired processing steps (Code 1). The image to be processed was selected and its channels and region of interest defined (Figure 3). The defined settings were stored in a CSV file (Code 2).

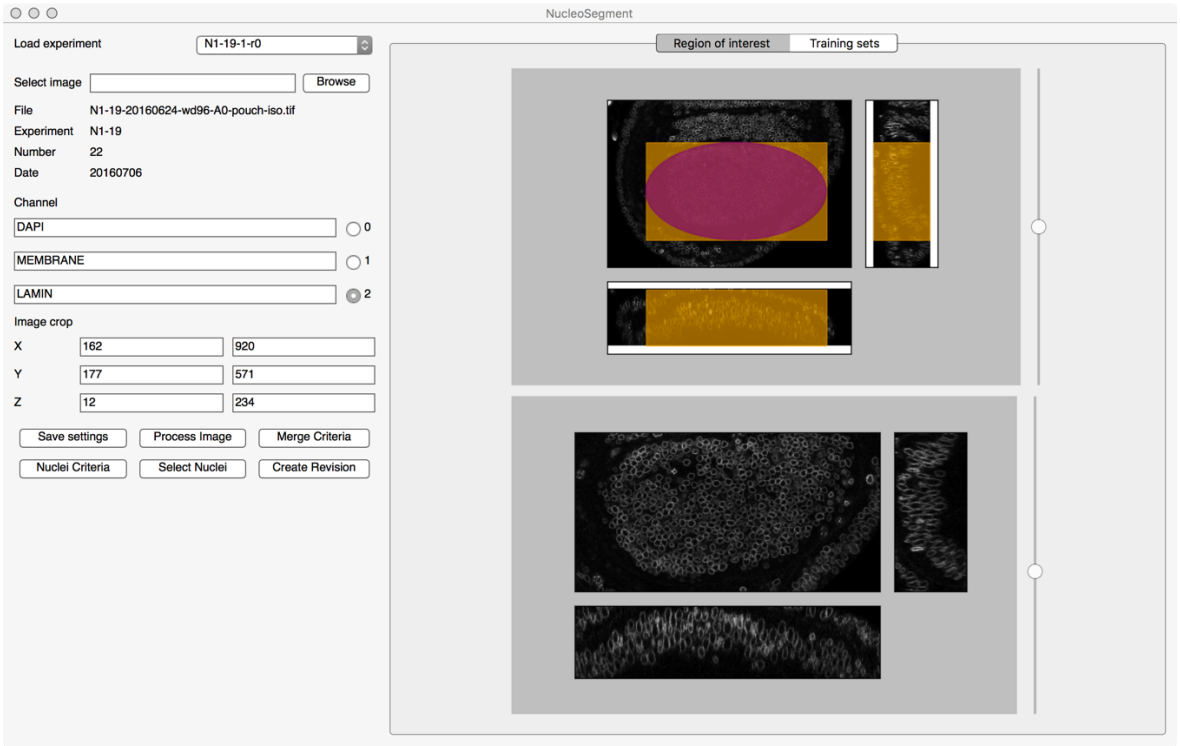


Figure 3: User interface to define the input file and its channels and region of interest.

2.8. Defining the processing parameters

The processing steps were defined by testing different filter combinations (Figure 4). The filters were represented by strings which were mapped in “config/filter_mapping.csv” to corresponding classes in “processing/filter.py” (Code 3). Every filter was a class with a defined “apply” function which required an image (2D or 3D) and corresponding parameters as input and returned the processed image (Code 4).

Based on the defined processing parameters (Code 5), the image stack was processed using the “process” function within the “Segmentation” class. This function invoked the static function “apply_filters_by_image_info” from “ImageProcessing” which in turn read the defined processing steps into a list of processing steps with their respective parameters. This

list was passed to the function “apply_filters” together with the image data for processing (Code 6).

The function cycled through all defined processing steps and created classes from the defined filters. Parameters were read into a dictionary which was passed to the “apply” function together with the image data. Filters were applied to each plane individually, unless the function supported the processing of a full image stack. The properties of the labels were extracted from each label in each plane and stored in a list (Code 7) which were saved to Python objects using “pickle”.

The aim of the processing steps was to extract individual nuclei labels. For all images, the following morphological filters were used in sequence: Equalize, Homogenize (disk: 10), Median (disk: 1), Enhance (disk: 5), Otsu threshold, Skeletonize, Closing (disk:3), Inverse, Convert to 16 bit and Label.

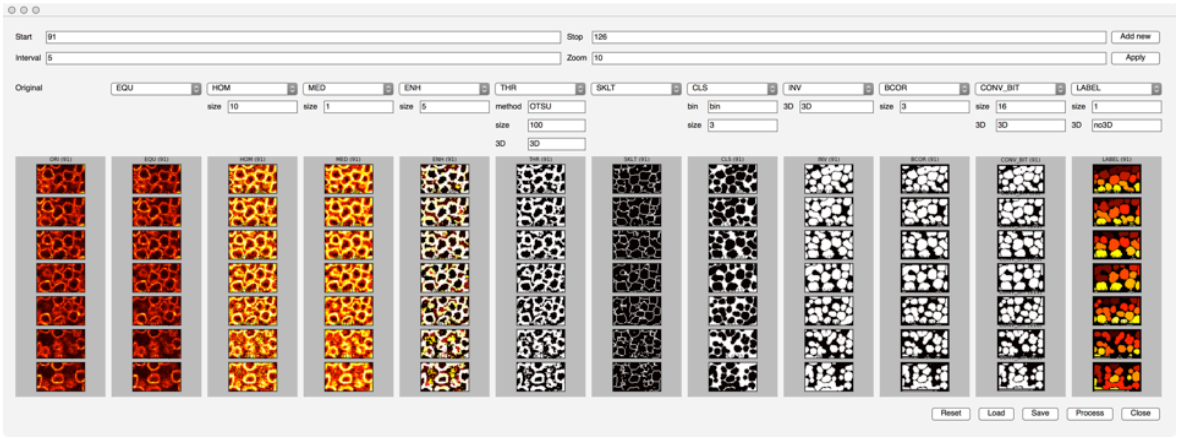


Figure 4: Defining processing steps. Combination of individual processing steps were tested for their ability to extract nuclei labels.

2.9. Merging labels and filtering nuclei

Labels were filtered using area and circularity (perimeter/$\sqrt{\text{area}}$) of the identified labels. The properties used to filter labels were defined in the configuration file “config/nuc_seg.ini” (Code 8). The minimum and maximum limits of the filters were set by visually assessing which labels were potential nuclei shapes and which not (Figure 5). After defining the filters, the settings were stored (Code 9) and labels filtered (Code 10). Filtered labels were merged across planes by calculating the overlap of all labels, at least 80%. For each plane, all labels were cycled through (Code 11) and tested for overlap in the next plane (Code 12). If no overlap was found in this plane, the following plane was tested. This search was repeated until an overlap

was found or the defined "merge depth" was reached. "Sandwiched" planes, where no overlap was found, were approximated by calculating the overlap between the current label and the overlapping label. The loop was iterated until all labels of all planes had been tested.

The merging process created a list of nuclei. Parameters of each nucleus were calculated using "calc_nucleus_params" in the "Nuclei" class and stored using the "LookupFrame" class which saved data in Pandas data-frames in CSV format for each experiment. Nucleus parameters were calculated based on the individual label properties. Volume was calculated by adding all label areas (Code 13). Apical distance was measured by calculating the direction vector from the bottom to the top centroid. With this direction vector, the distance from the nucleus centre to the last membrane signal was calculated. The contact area of nuclei was calculated by dilating nuclei with a factor of 2 and calculating the overlap with surrounding nuclei. The contact area was then divided by the surface area of the nucleus. Contacting nuclei were counted as neighbours.

Merged nuclei were filtered by size and depth (z-planes). Thresholds were defined visually and stored in the same way as label filters (Figure 6). Nuclei were filtered (Code 10) and removed nuclei were added to the "Correction" class which stored deleted nuclei within lists and Python objects using "pickle".

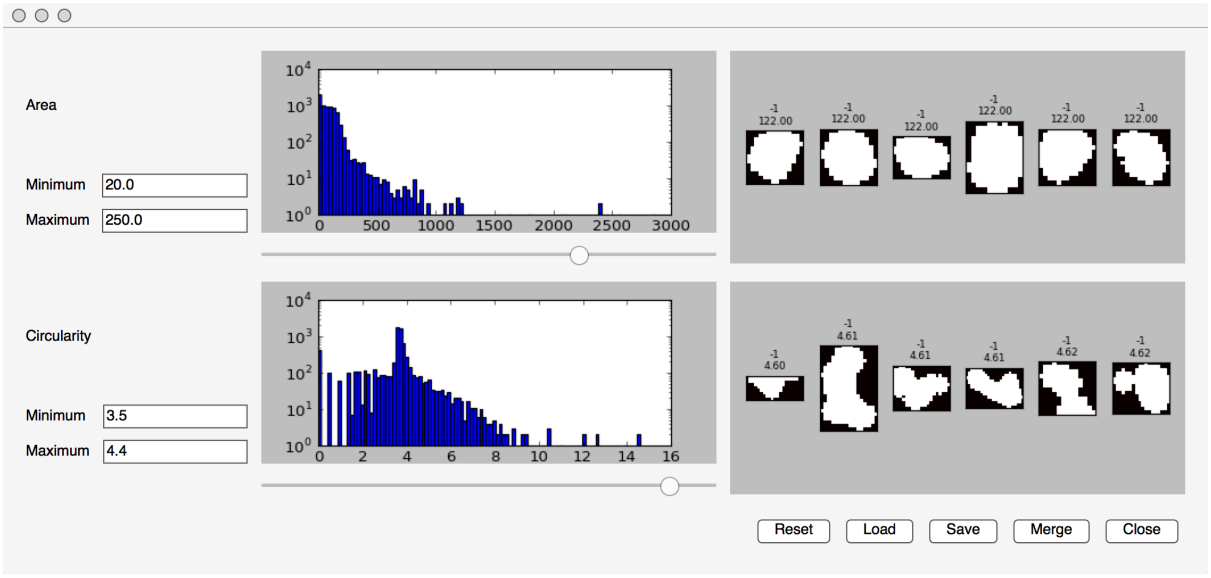


Figure 5: Filtering labels. Labels were filtered by visually inspecting minimum and maximum values for area and circularity (perimeter/$\sqrt{\text{area}}$).

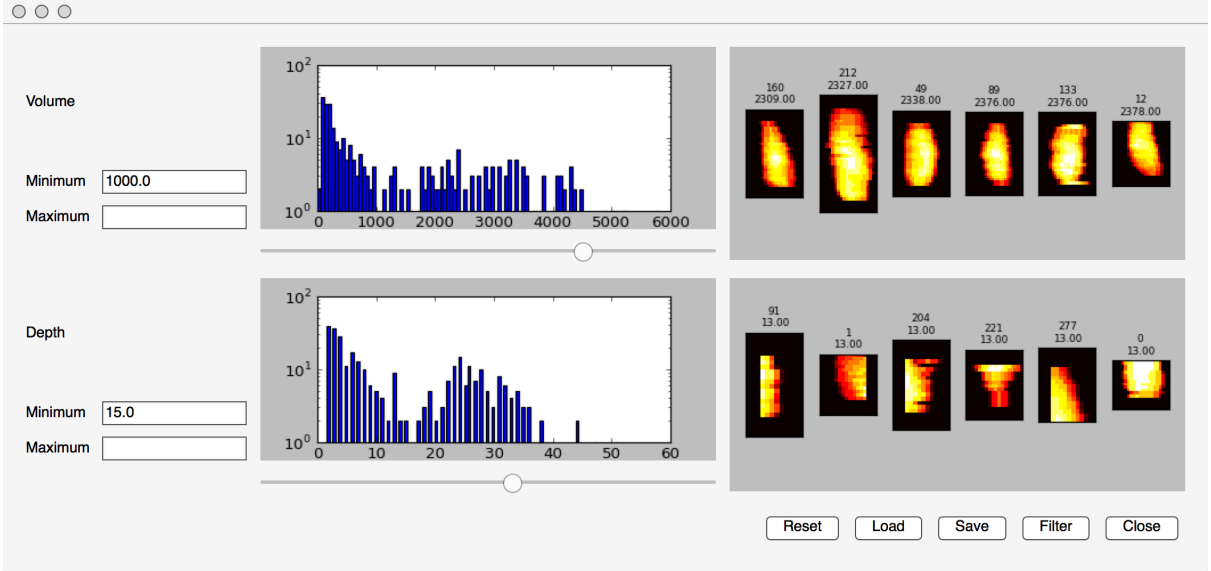


Figure 6: Filtering merged nuclei. Nuclei thresholds for volume and depth (z-planes) were determined visually based on z-projections.

2.10. Correcting nuclei

Nuclei outside the pouch were determined visually and deleted (Figure 7). Deleted nuclei were flagged as removed and added to the correction lists (Code 14). Remaining nuclei were assessed using the "Select non nuclei" interface (Figure 8a, b) which marked nuclei centres with a red cross. Ambiguous nuclei were visualised with a pseudo 3D box (Figure 8c, d) and judged based on Lamin and membrane signals. The remaining nuclei were checked visually by their cross-sections in a gallery mode (Figure 9) and deleted if necessary, for example when nuclei were merged together (Figure 10a). Nuclei were also corrected by redefining the top and bottom planes (Figure 10b) and remerged by using the remaining labels as starting points for the merging function. The final segmentation was exported to TIFF files and visually checked in Fiji (Figure 11).

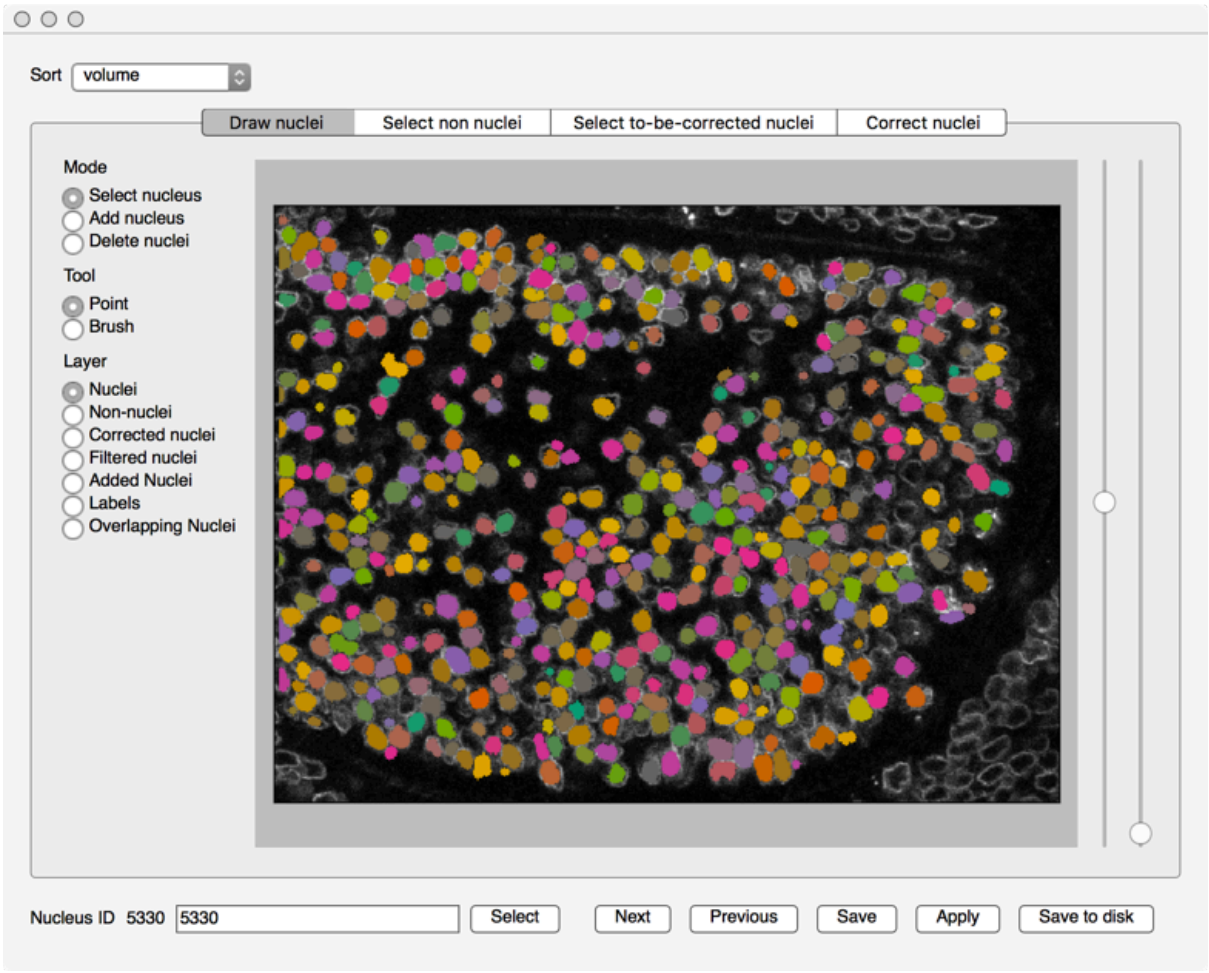
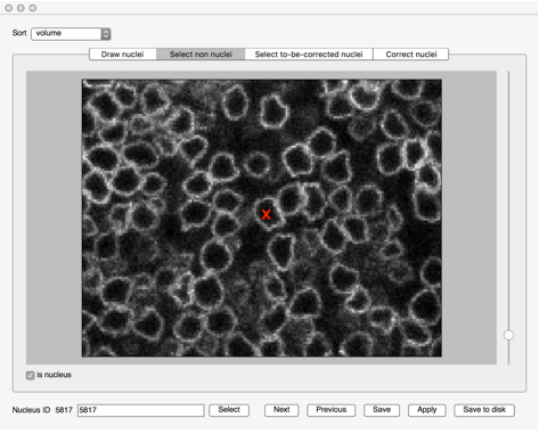
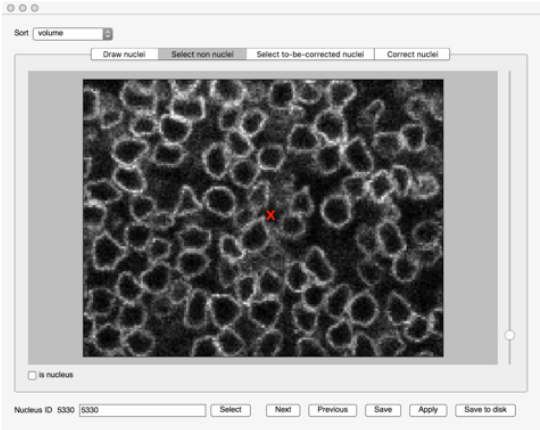


Figure 7: Deleting nuclei not in the region of interest. The user interface provided options to select, add and delete individual nuclei.

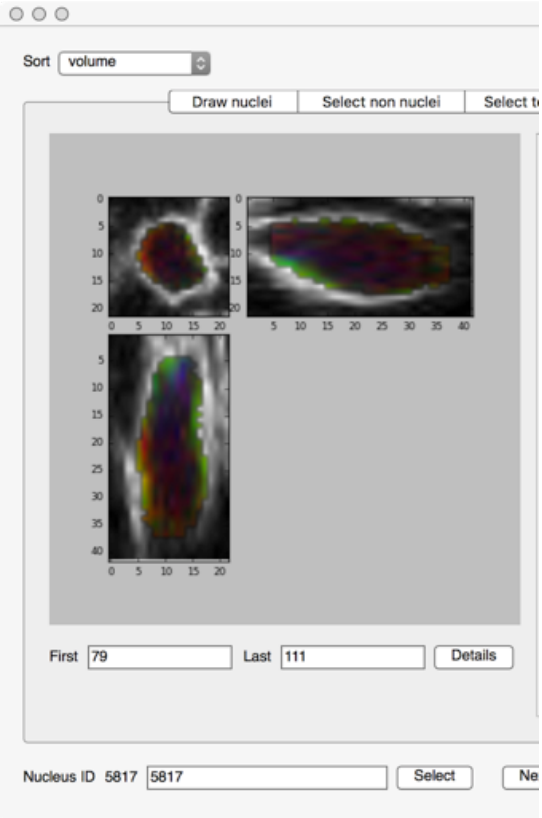
a) Nucleus



b) No nucleus



c) 3D box of nucleus



d) 3D box of non-nucleus

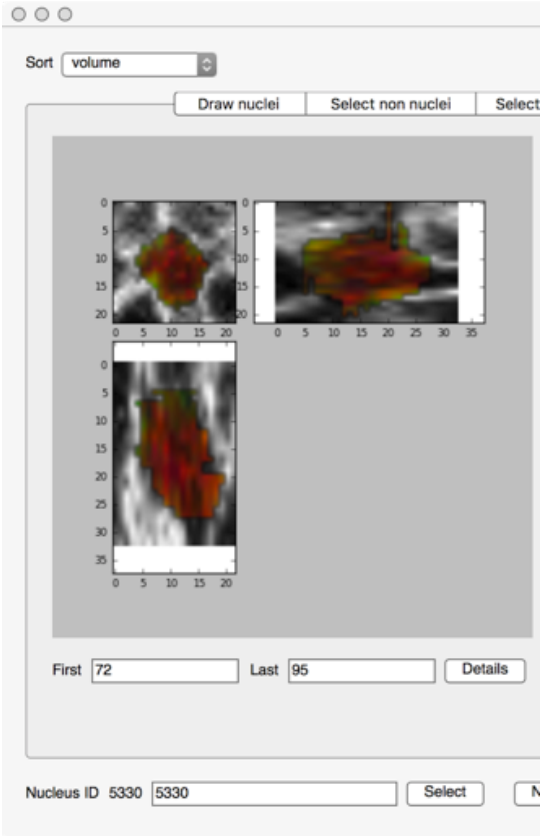


Figure 8: Deleting non-nuclei. a, b) The "Select non nuclei" interface enabled cycling through all nuclei by marking their centre with a red cross. c, d) 3D nuclei boxes with Lamin (green), membrane (red) and DAPI (blue) as overlays.

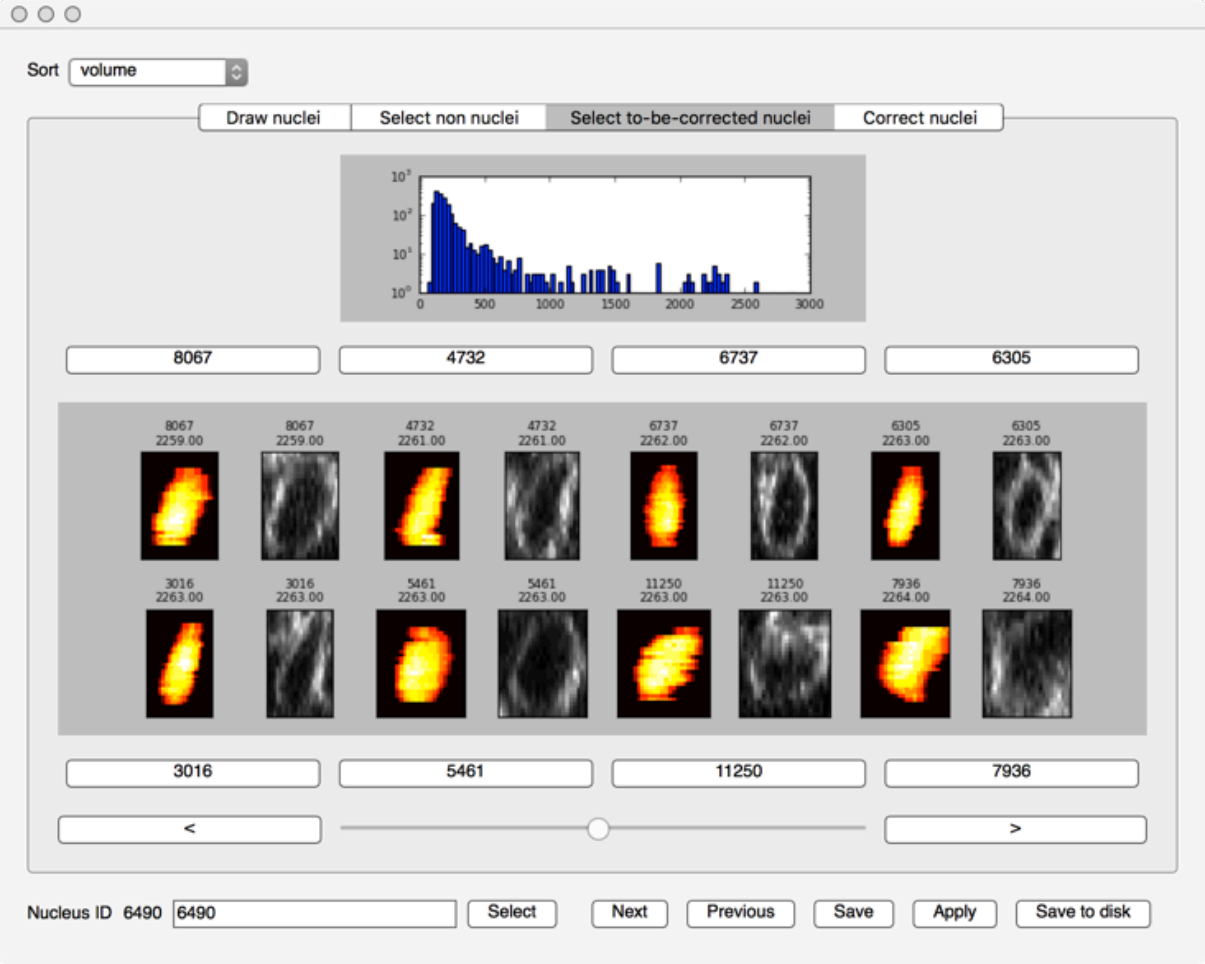


Figure 9: Checking nuclei in the gallery mode. Nuclei were shown as z-projections and visually judged for their appearance as elliptical nuclei.

a) Gallery

b) Nuclei correction

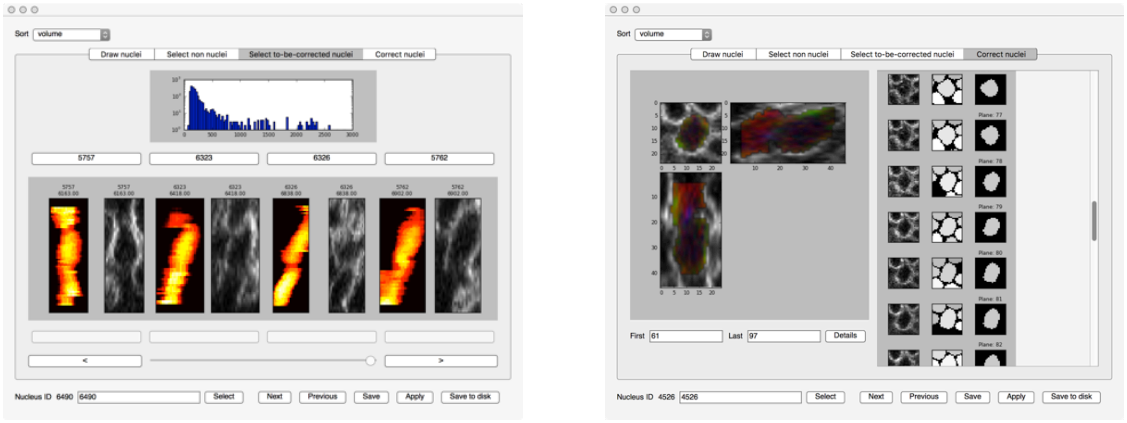


Figure 10: Detection and correction of segmentation errors. a) Nucleus gallery of z-projections. Example shows merged nuclei. b) Correction of nuclei by visually checking start and stop planes of each nucleus.

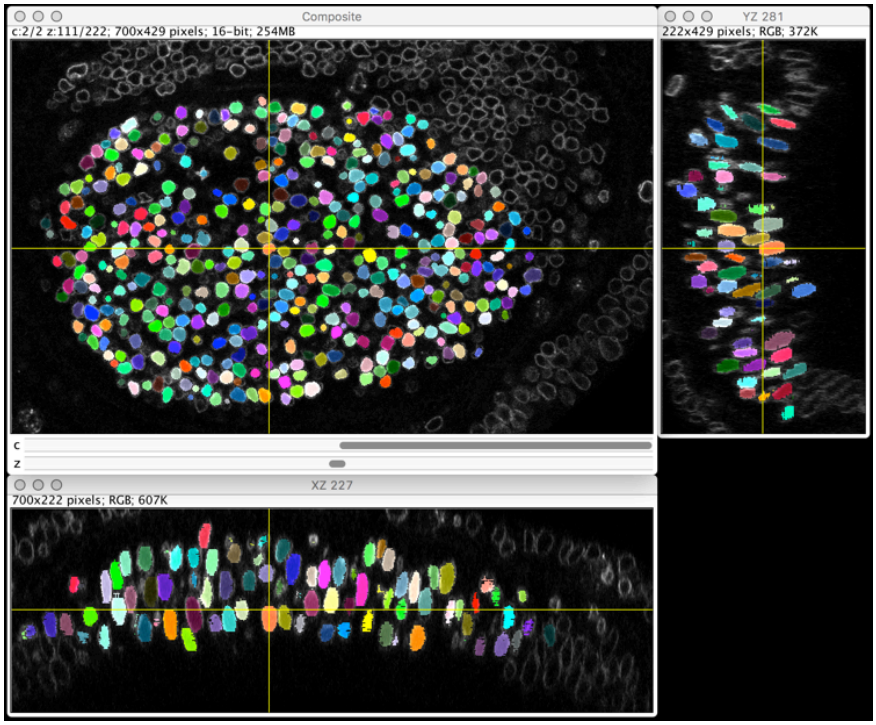


Figure 11: Segmentation as TIFF file in Fiji. The segmented nuclei image was overlain with the Lamin signal. Orthogonal views shown.

2.11. Quantifying segmented nuclei

The segmented nuclei images were tiled into five 50x50px tiles which were sampled with 10px offsets and averaged (Figure 12; “nucleo_quant.py”). Only nuclei with their centre within a tile were included to calculate densities, volumes and positions. The volume fraction was calculated by the ratio of the summed pixels from the binarised membrane signal (Code 15) and the nuclei segmentation. Values from heatmaps were stored as CSV lists and analysed with GraphPad Prism 7.

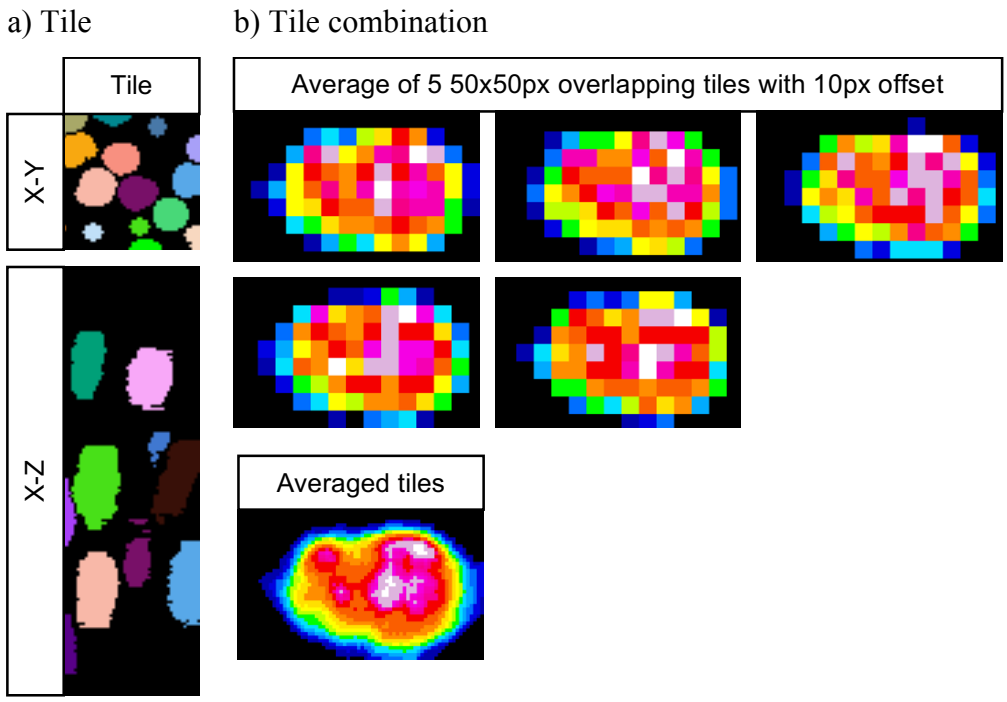


Figure 12: Quantification of segmentation by tiling combination. a) Segmented images were separated into 50x50px tiles and all nuclei with their centre within a tile were used for calculations. b) Averaging of tiled images with an offset of 10px.

3. Results

The wing imaginal disc is a highly proliferative tissue, growing from 50 cells, during embryonic stages, to 50,000 cells, during the third larval instar (Mandaravally Madhavan and Schneiderman, 1977). Studies measuring the apical cell area indicated increasing compression in the middle of the pouch (Aegerter-Wilmsen et al., 2012, Mao et al., 2013). As an alternative means of estimating compression, nuclear packing was assessed in larvae synchronised using morphological features of the L2-L3 moult (Supplementary Figure 1) and timed for 3 dAEL (72 hrs), 4 dAEL (96 hrs) and 5 dAEL (120 hrs). The membrane of wing imaginal discs was visualised using a Tubulin-Myristoylated-mCherry reporter and nuclei were stained with anti-Lamin. Discs grew significantly over time (Figure 13a) while nuclei appeared more dense and less round (Figure 13b). The mounting conditions did however not preserve the overall shape of the disc, as they were mounted flat on the coverslip (Figure 13b).

3.1. Preserving tissue shape during preparation

To determine tissue-wide properties, all nuclei of the pouch had to be captured while preserving tissue shape. Thick sections (40µm) cut from discs embedded in gelatin albumin preserved the highly folded shape of the disc and the characteristic dome structure of the pouch (Figure 14a; compare to Figure 13b). However, this approach can inherently only capture part of the pouch. Alternative strategies were tested to preserve the shape while allowing imaging of the whole pouch area. Spacers (two layers of tape or 250µm gelatin albumin blocks) preserved the shape of the tissue (Figure 14b). However, handling was difficult as discs sometimes moved during imaging as high numeral aperture objectives pushed against the coverslip. To prevent movement and enable close imaging, discs were attached to poly-lysine coated coverslips (Figure 14b). However, this led to considerable tissue flattening, which might disturb the packing of nuclei.

Studies investigating the zebrafish eye (Nikolaou et al., 2012) regularly use agarose embedding to immobilise fish and enable close imaging. Discs were therefore dipped in 1% low melting agarose and transferred in a 10µl drop onto the coverslip (Figure 14b). This strategy, combined with a 63x glycerol objective with a working distance of 280µm and a numerical aperture of 1.3, preserved the tissue shape and enabled imaging of the whole disc close to the coverslip at a high resolution. However, signal intensity decreased along the apical-

basal axis, at increasing depth. To enable uniform signal acquisition, the staining protocol for nuclei was optimised and a tissue clearing solution was tested.

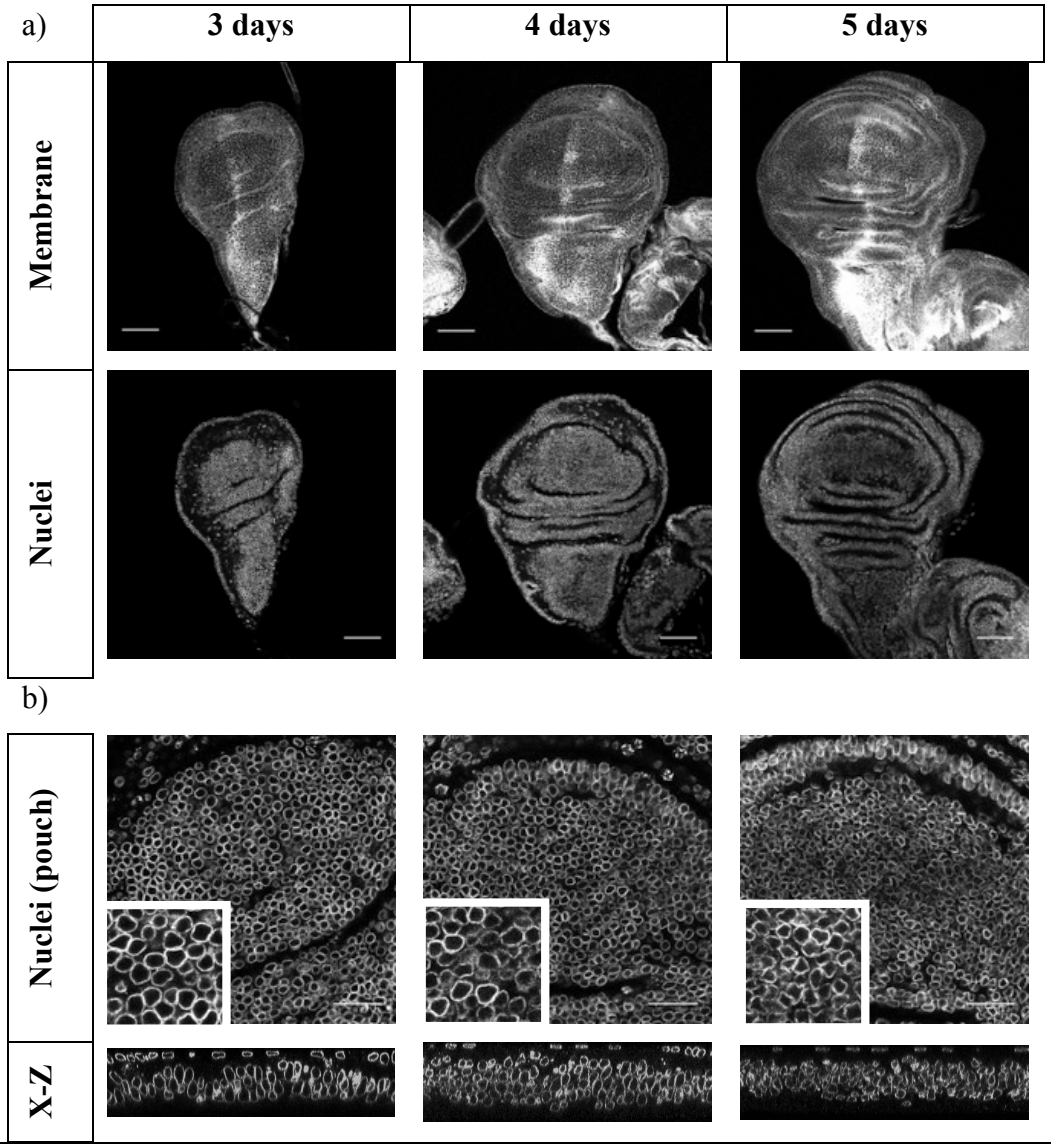


Figure 13: Nuclei appeared to increase in density and decrease in smoothness during growth. Third instar Tubulin-Myristoylated-mCherry/TM3 larvae were staged by collecting eggs on grape juice plates and a drop of baker's yeast in cages for 2hrs. Larvae were staged by morphological features for 3 (n=6), 4 (n=6) and 5 (n=6) days after egg laying. Larvae were inverted, fixed and stained with anti-Lamin and 488 anti-mouse secondary antibody. Wing imaginal discs were dissected in PBS and mounted in a drop of Mowiol with larval mouthparts or brains as spacers. Images were acquired on confocal microscope. Scale bars 50μm (a; disc) and 20μm (b; pouch). Further examples are shown in Supplementary Figure 2 and Supplementary Figure 3.

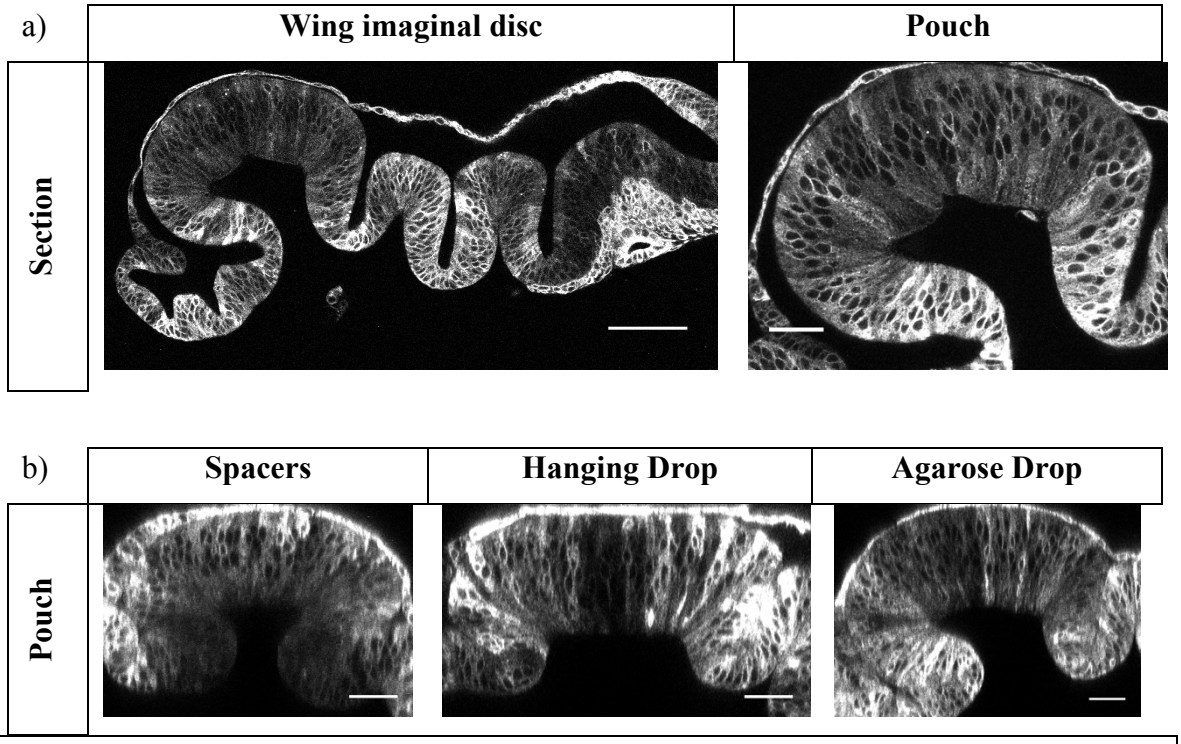


Figure 14: Preserving tissue shape. Tubulin-Gal4, UAS-CD8-GFP larvae were fixed and stained with anti-Lamin. a) Wing imaginal discs were embedded in gelatin albumin and sectioned (40µm) using a vibratome (n=1) with the help of Andrew Bailey. b) Wing imaginal discs were mounted with two layers of tape (n=1) or 250µm gelatin albumin spacers (n=1), a poly-lysine hanging drop (n=3) or an agarose drop (n=3). Scale bars 50µm (disc) and 20µm (pouch). Further examples of mounting strategies are shown in Supplementary Figure 4. Examples of successful mounting and common mistakes during agarose embedding are shown in Supplementary Figure 5.

3.2. Nuclei staining was optimised

Standard staining protocols with 0.1% triton before primary and secondary antibody staining did not label the middle of the pouch (Figure 15, A). The triton concentration before primary antibody binding was increased to 0.5% and kept at 0.1% during primary and before secondary binding (Figure 15, B). This enhanced the staining, but was not sufficient for thorough staining. Increasing triton to 0.5% during all stages until wing imaginal disc dissection yielded a homogenous staining of nuclei (Figure 15, C).

As an alternative strategy, and with a long term view to carry out live imaging, a construct with a myristoylated mCherry and Lamin fused to Citrine linked by the self-cleaving 2A peptide was constructed and injected into *w1118* flies (Figure 16a). The Lamin signal was uniform within the disc and enabled visualisation of the cell membrane at the same time (Figure

16b); however, considerably more laser power had to be used compared to antibody staining (> 20% compared to <10%; Figure 16b). Subsequent experiments used this construct with or without Lamin antibody staining.

A uniform signal along the apical-basal axis was difficult to achieve because of the thickness of the tissue and the resulting light scattering. Mounting wing imaginal discs with Vectashield did not overcome this problem since it did not yield a uniform apical-basal signal (Figure 17). Clearing solutions are routinely used to make thick tissues, such as a mouse brain, transparent (Richardson and Lichtman, 2015). FocusClear, a soluble clearing-agent, was tested for its ability to clear imaginal discs because of its ease of use. The complete FocusClear kit, including the clearing solution, mounting media and immersion solution, yielded a uniform staining along the apical-basal axis (Figure 17). The mounting solution and immersion solution were necessary to yield a uniform signal (Figure 17), while FocusClear alone was comparable to Vectashield (Figure 17). The agarose embedding protocol enabled simple exchange of the clearing solution with the mounting solution.

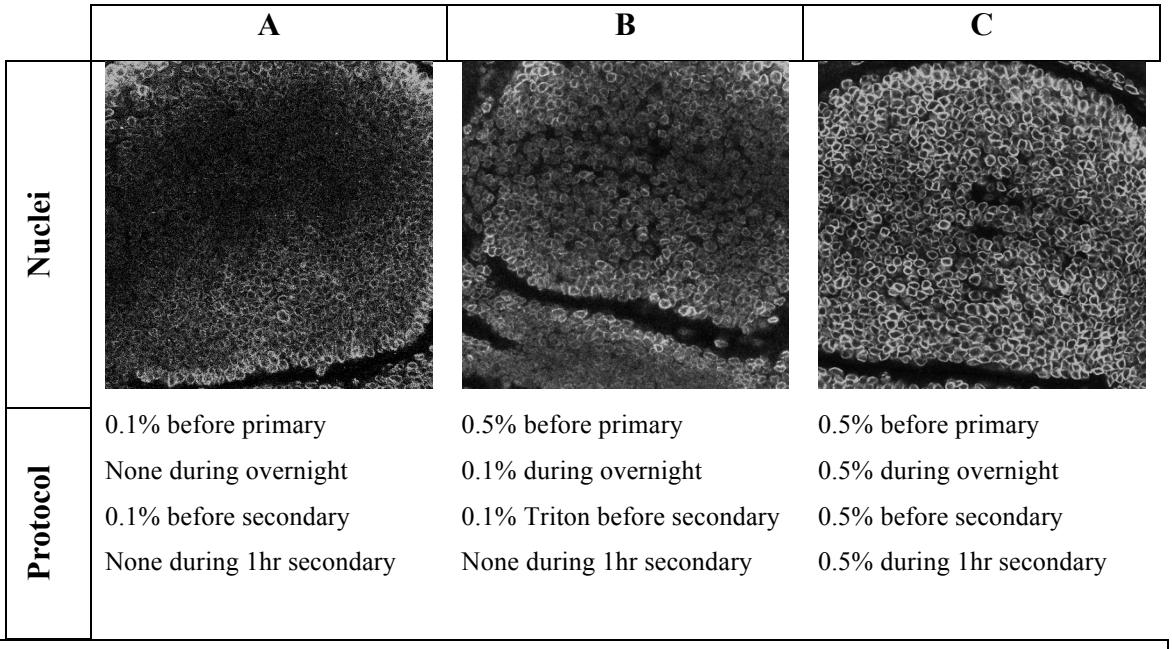


Figure 15: Increasing triton concentration resulted in a uniform Lamin staining. Third instar Tubulin-Myristoylated-mCherry larvae were fixed and stained with anti-Lamin and DAPI using a low triton concentration (A; n=1), increased triton concentration before primary antibody binding (B; n=1) and increased triton concentration during all stages (C; n=6). Wing imaginal discs were dissected and imaged using confocal microscopy.

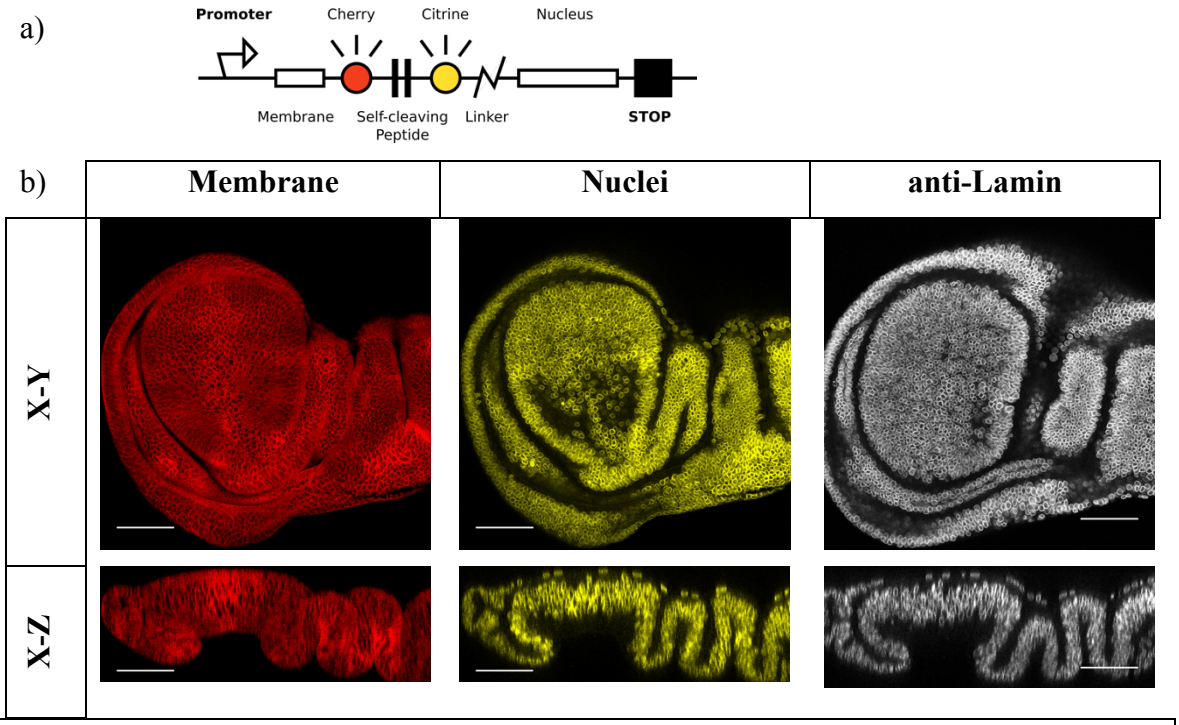


Figure 16: Construct enabled simultaneous imaging of nuclei and membrane. a) Schematic of construct. b) Mid third instar Tubulin-Myristoylated-mCherry-2A-Citrine-Lamin/TM3 larvae were fixed and left untreated (n=6) or stained with anti-Lamin (n=5). Their wing imaginal discs were dissected and embedded in a 1% agarose drop on a coverslip. Once settled, embedded tissues were supplemented with FocusClear kit reagents. Images were acquired on confocal microscope. Scale bar 50µm. Further examples are shown in Supplementary Figure 6.

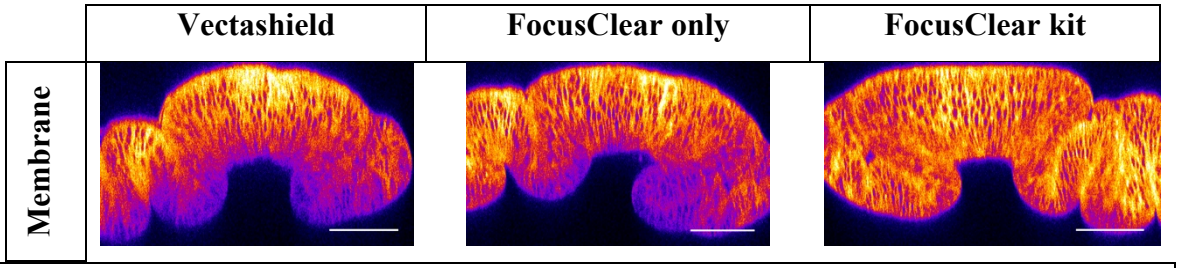


Figure 17: FocusClear enabled a homogenous signal along the apical-basal axis. Late third instar Tubulin-Myristoylated-mCherry-2A-Citrine-Lamin/TM3 larvae were fixed, their wing imaginal discs dissected and embedded in a 1% agarose drop on a coverslip. Embedded tissues were supplemented with Vectashield (n=2), FocusClear only (n=4) or all FocusClear kit reagents (n=3). Images were acquired on confocal microscope. Scale bar 50µm. Further examples are shown in Supplementary Figure 7.

3.3. Time course under optimal mounting conditions

The developed protocol involves staging larvae at the L2-L3 moult, staining nuclei with antibody, embedding the tissues in agarose, clearing with FocusClear and imaging with a 63x glycerol objective on a confocal microscope (Figure 18). With this protocol, the initial time-course (Figure 13) was repeated (Figure 19). The tissues showed their characteristic folds and the emerging dome structure of the pouch at the end of the third larval instar. Nuclei appeared increasingly stacked on top of each other and the tissue increased in thickness up to 50-60µm.

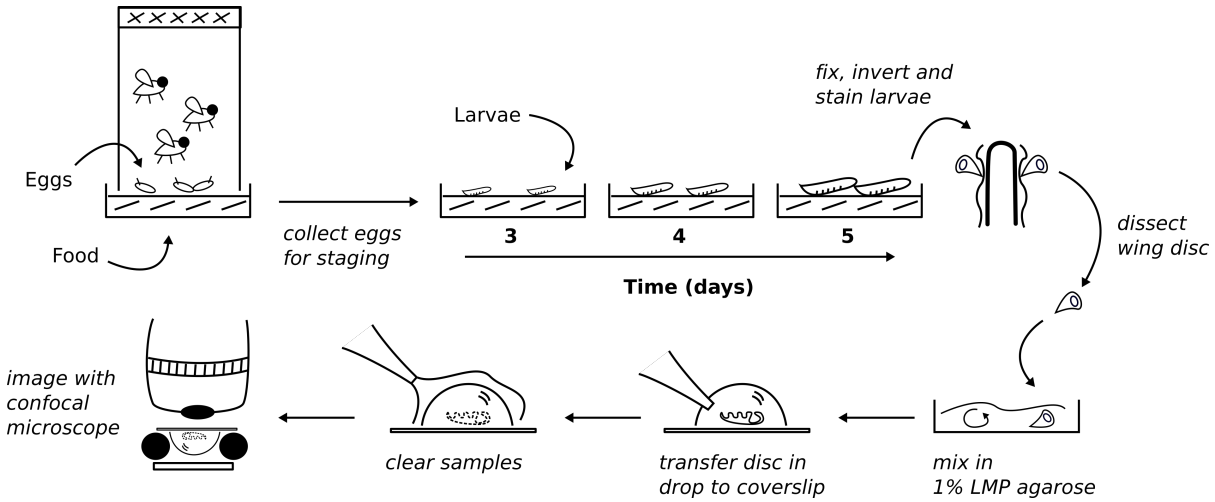


Figure 18: Developed imaging pipeline. Larvae were staged by morphological features of the L2-L3 moult, fixed, inverted and stained with Lamin antibody. Wing discs were dissected, mixed in 1% low melting point agarose and transferred in a drop onto the coverslip. Samples were cleared with FocusClear and subsequently imaged with a confocal microscope.

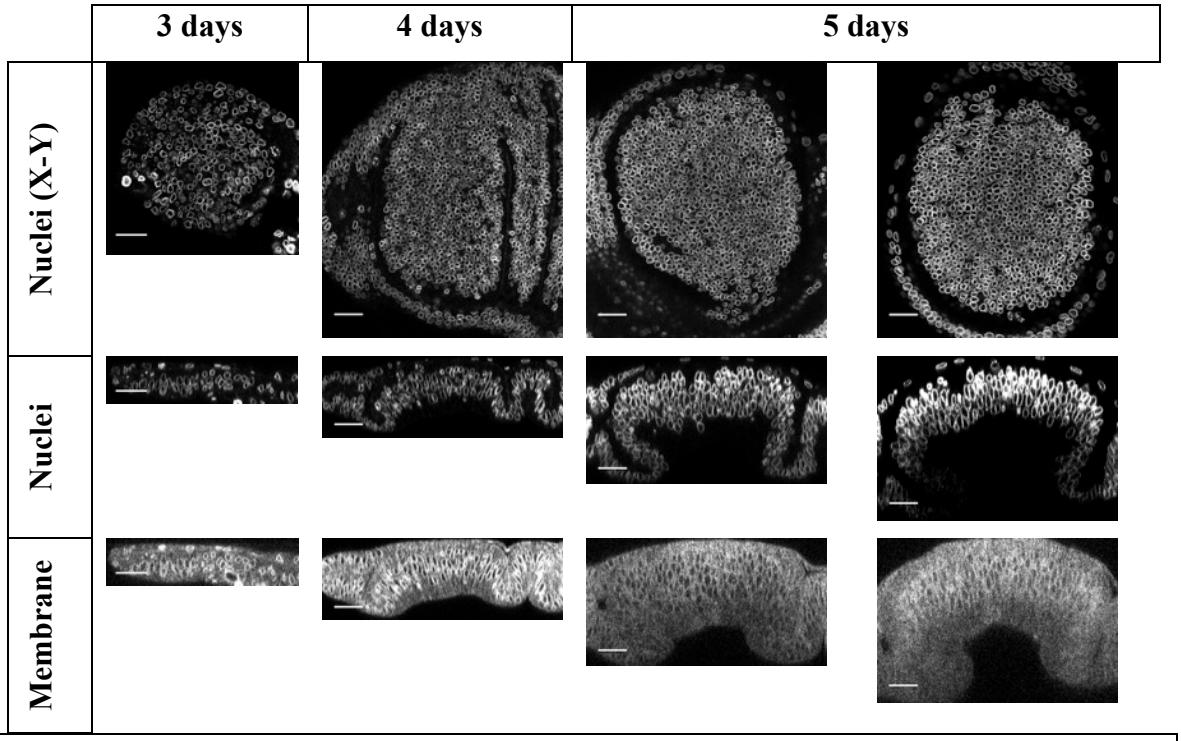


Figure 19: Time-course of wing imaginal disc growth with established protocol. Tubulin-Myristoylated-mCherry-2A-Citrine-Lamin/TM3 larvae were staged by morphological features for the L2-L3 moult and transferred to a new food dish. Larvae were fixed at 3 days (n=1), 4 days after egg laying (dAEL) (n=2) and at early and late wandering stage after 5 dAEL (n=4). Their wing imaginal discs were dissected and embedded in a 1% agarose drop on a coverslip. Once settled, embedded tissues were supplemented with FocusClear kit reagents. Images were acquired on confocal microscope. Scale bar 20µm. Further samples are shown in Supplementary Figure 9.

3.4. Optimisation of segmentation parameters

Staining for the nuclear envelope was expected to circumvent challenges often encountered using intra-nuclear staining to distinguish closely packed nuclei (Rajasekaran et al., 2016). I reasoned that, morphological filters used to segment cell membranes (Stegmaier et al., 2016), could be used to extract nuclei on each confocal plane and the resulting labels could be merged across planes. Based on this strategy, a user-guided segmentation pipeline was developed in Python (Figure 20; see Materials and Methods for implementation details).

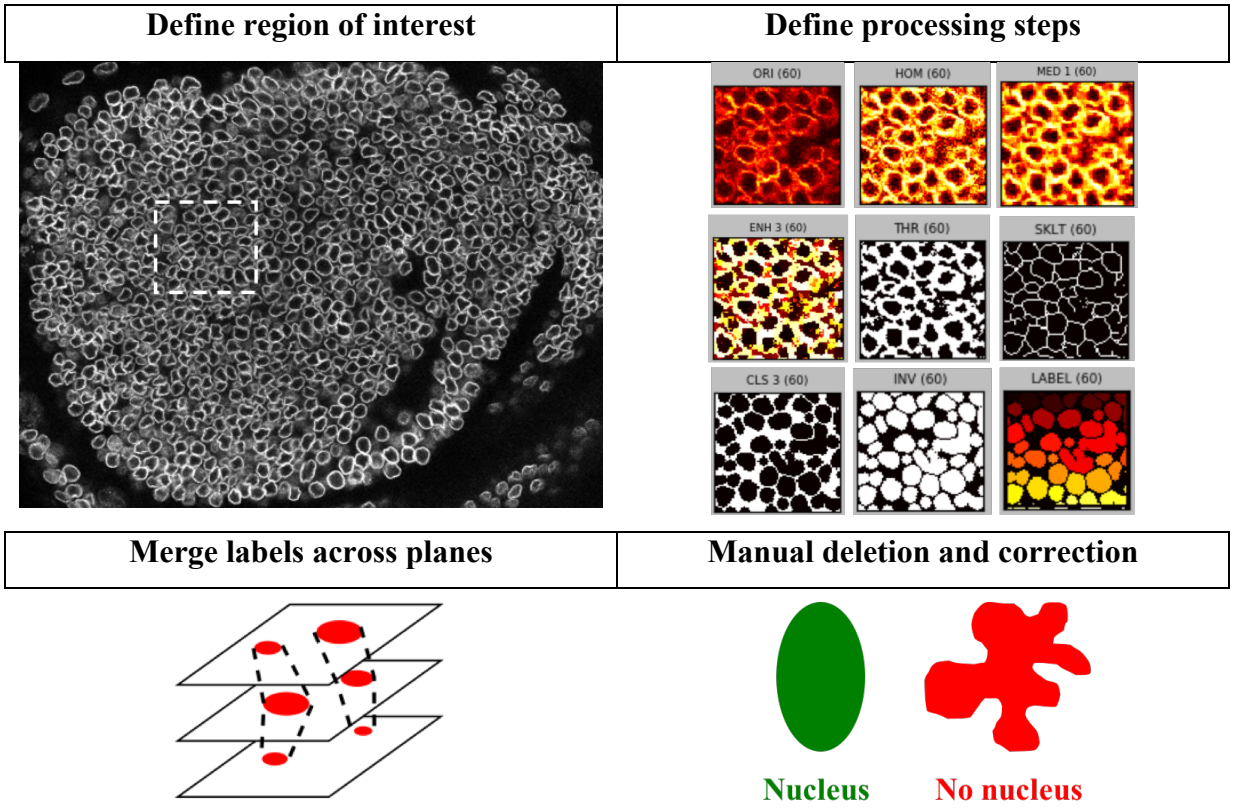


Figure 20: Segmentation workflow. The region of interest was chosen and respective processing steps were defined to extract labels from each plane. Individual labels were merged across planes resulting in potential nuclei. The segmentation was manually corrected by deleting non-nuclei and correcting remaining nuclei.

The sequence of morphological filters should enhance the Lamin signal and extract labels on each plane. Three regions of a 4-day sample were chosen at random to test the processing parameters. Different combinations were tested for their ability to extract distinct labels (Figure 21). The first steps homogenised the signal (Figure 21a) and enhanced the borders of nuclei with a median filter of 1 and an enhancement of 3 (Figure 21b). A skeleton was created from the nuclei using Otsu thresholding and skeletonise (Figure 21c). Smaller objects were removed and nuclei kept apart from each other using a closing of 3 (Figure 21d). Finally, the image was inverted, its borders corrected, converted to 16 bit and labels created (Figure 21e). The resulting labels represented nuclei and background. The images were corrected using the developed correction interface. Non-nuclei were removed and the remaining ones corrected for their start and stop planes (Figure 22). In rare cases where nuclei were fused together, one nucleus was corrected for its start and stop planes leaving the other unsegmented. Due to technical difficulties, the latter could not be added back to the segmentation by remerging.

The resulting segmentations for the three regions are shown in Figure 23. Segmented nuclei appeared rounder than the Lamin signal and flat at the top and bottom in cross-section. Nonetheless, the level of accuracy was judged sufficient for segmentation of the acquired time-course samples.

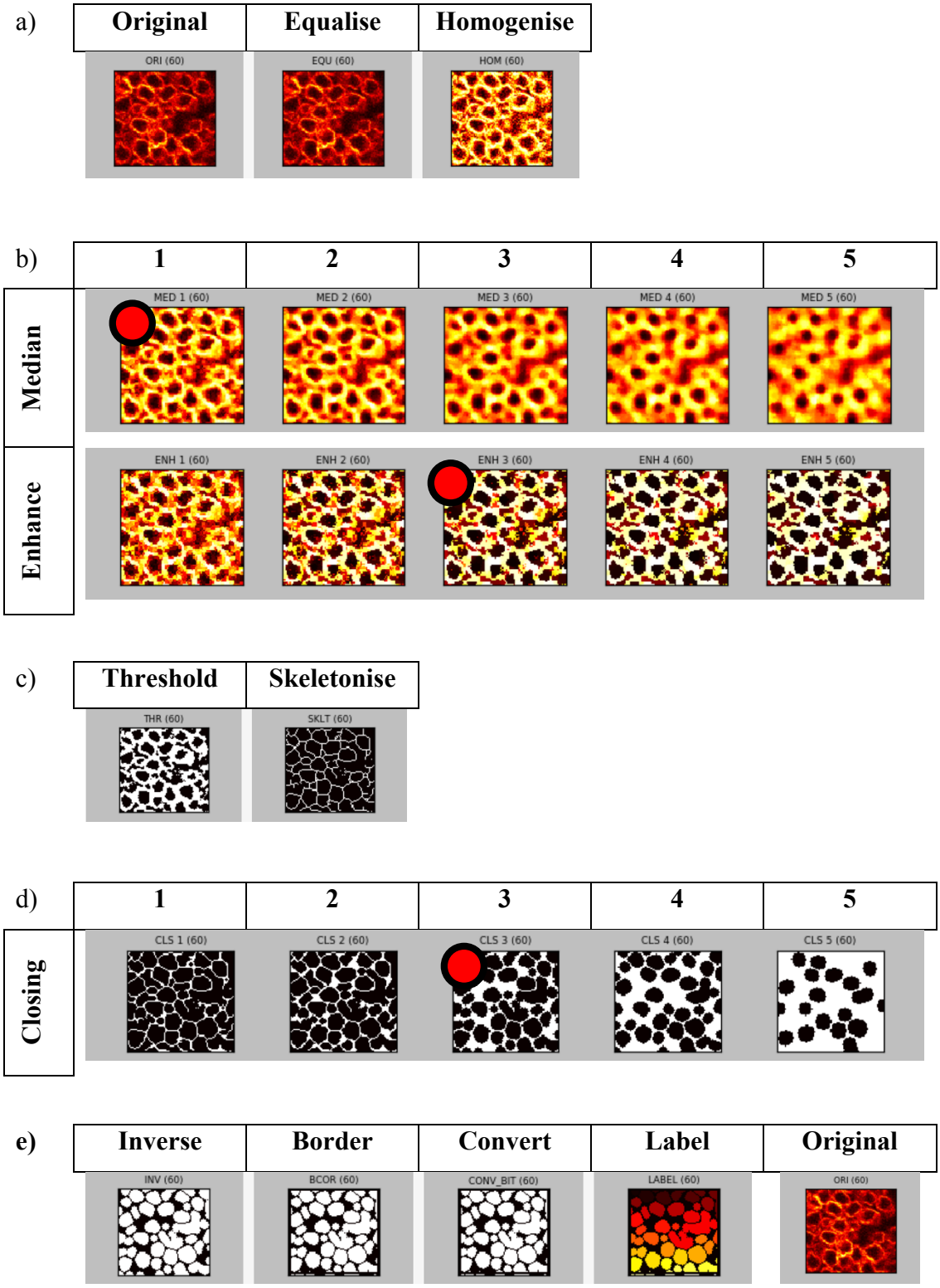


Figure 21: Testing parameters for morphological filters. The user interface allowed testing of a range of parameters for the selected filters to select the best sequence. a) Homogenised signal. b) Enhanced nuclei shapes. c) Extracted skeleton. d) Extracted blobs. e) Corrections and label creation. Original image is shown for comparison. Red circles indicate chosen parameter values.

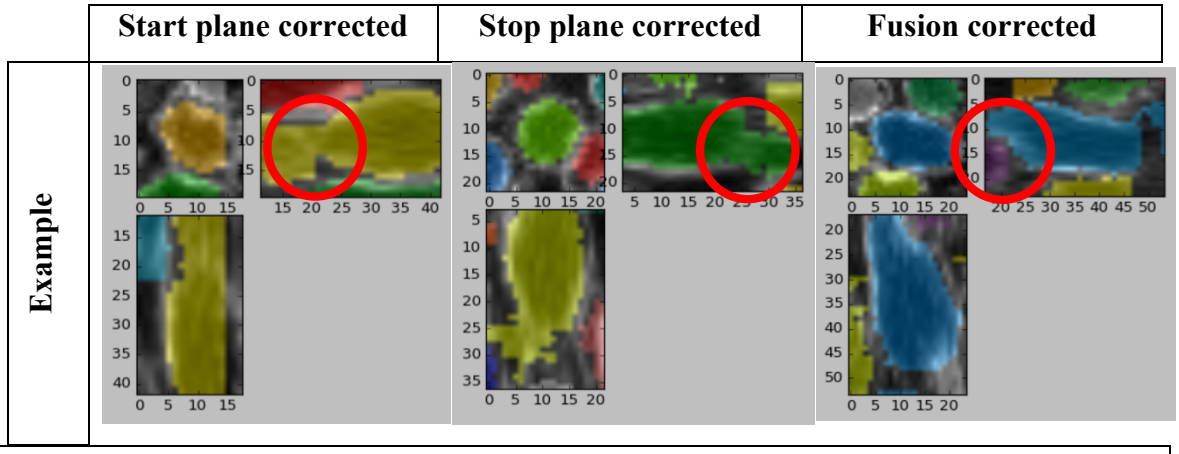


Figure 22: Typical correction for nuclei. a) Start plane too early. b) Stop plane too late. c) Purple and blue nuclei were fused.

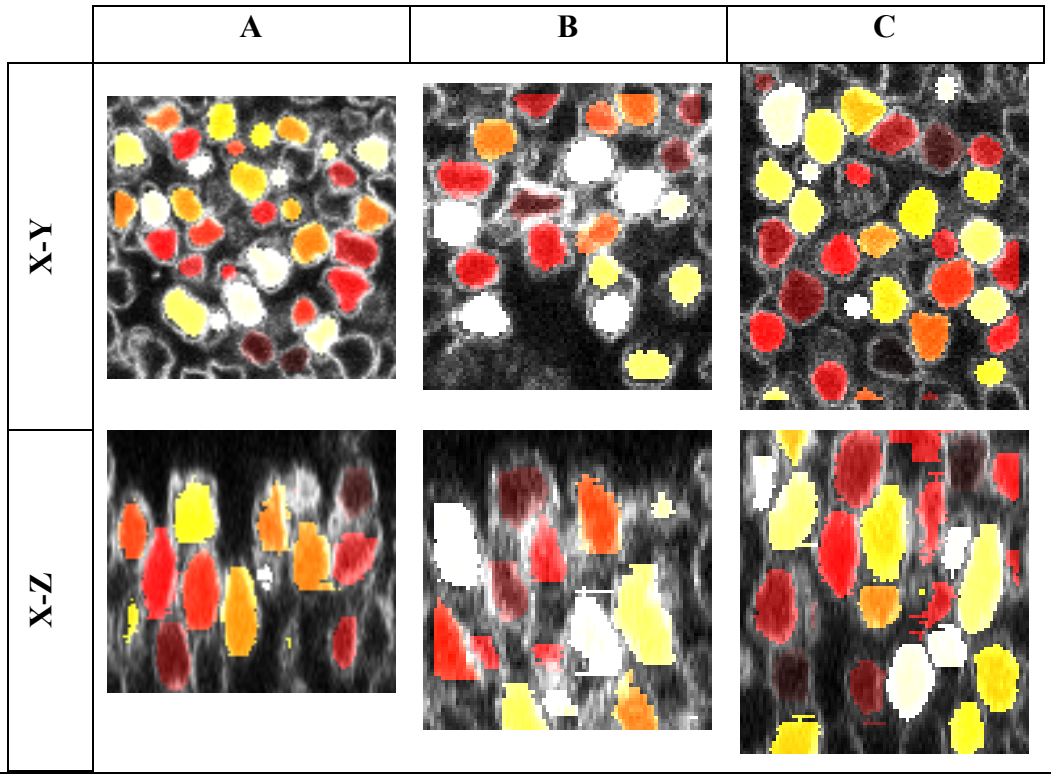
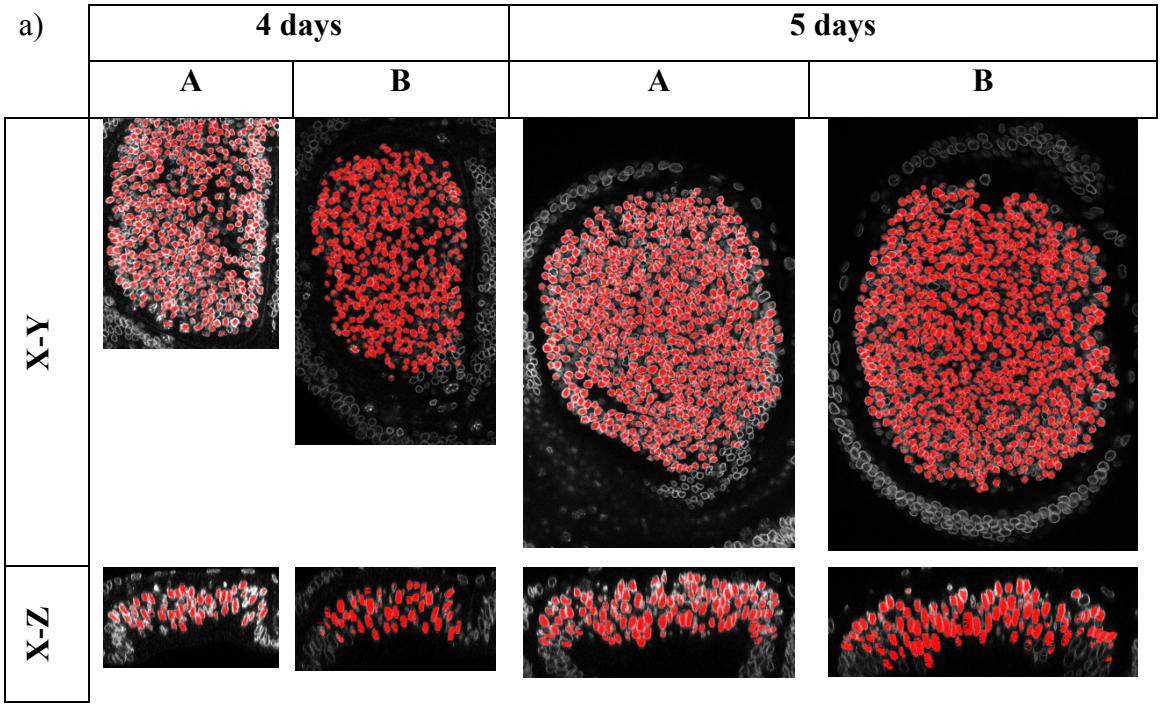


Figure 23: Segmentation for tested regions. Regions were chosen at random from a 4-day sample, nuclei segmented using the developed program and the resulting segmentation overlain with the Lamin signal.

3.5. Nuclear segmentation

Using the tested filters and parameters, two samples from 4 and 5 days were segmented (Figure 24a) resulting in 1,688 and 1,467 nuclei for 4-day samples and 4,008 and 3,791 nuclei for 5-day samples (Figure 24b). The resulting segmentations were checked by visual inspection of the overlay between the Lamin signal and the identified nuclei. Big nuclei failed to be segmented as the filtering parameters did not produce labels which could be sufficiently merged (Figure 25). Nuclei on the edge were removed because their segmentation was not accurate. Numbers of missing nuclei were estimated by visual inspection (Figure 24b). Although some of the biggest nuclei could not be segmented, missing nuclei were estimated to be less than around 30.

a)



b)

Nuclei:	1688	1467	4008	3791
Removed:	1948	4064	7748	7502
Corrected:	60	144	614	921
Missed:	< 10	< 10	< 20	< 30

Figure 24: Segmented nuclei from time-course. a) Lamin signal with segmented nuclei overlay in red. b) Numbers of identified nuclei after manual removal and correction of nuclei. Missing nuclei were estimated by visual inspection.

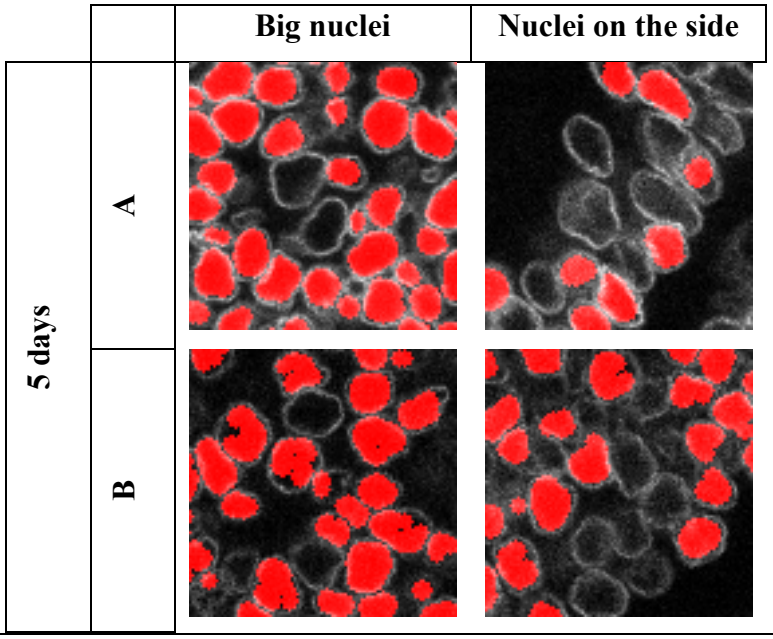


Figure 25: Examples of missed and excluded nuclei.

3.6. Quantification of nuclei packing

The segmented nuclei were analysed using a tiling approach. Images were divided into 50x50px tiles and the attributes of nuclei, whose centres were within a tile, were counted. Tiles were averaged by applying an offset of 10px resulting in five sample averages within 10x10px squares.

Increasing compression (Aegerter-Wilmsen et al., 2012) might result in decreased nuclei volume during later developmental stages. Therefore, the first focus was to quantify nuclei densities and volumes. Nuclei densities in 4-day samples were distributed evenly while fewer nuclei were present along the dorsal-ventral boundary of the anterior compartment in 5-day samples (Figure 26a). The volume in 4-day samples was distributed homogenously while 5-day samples showed an inverse pattern compared to nuclear densities; bigger nuclei were located at regions with fewer nuclei and vice versa (Figure 26a). Analysing the total volume, by summing all nuclear volumes, resulted in a homogenous distribution in 4- and 5-day samples (Figure 26a); again, indicating that nuclei densities and volumes complemented each other. While the average nuclei volume per tile appeared unaffected, the maximum nuclear volume reached in 5-day samples was higher (Figure 26b). Crucially, the total volume per tile increased in 5-day samples (Figure 26b).

An alternative approach to further analyse nuclei densities was developed by relating the nuclei volume to the tissue volume. The membrane signal was binarised and used to calculate the tissue volume (Figure 27a). Tissue volume per tile increased in one 5-day sample (Figure 27b). Nuclei volume was calculated by counting the pixels of the nuclear segmentation within a tile; therefore, nuclei were also partially counted. Nuclear volume per tile increased in 5-day samples (Figure 27) which was comparable to the previously calculated total volume using volumes of nuclei with their centres within a tile (Figure 26b). Interestingly, the volume fraction (nuclei volume per tissue volume) increased in 5-day samples (Figure 27). As an alternative measure of the nuclei volume fraction, total nuclei volume per stacking height (maximum apical distance of nuclei within a tile) was calculated (Figure 28). Stacking height was spatially uniform and increased to up to 40µm in 5-day samples (Figure 28b). Again, the nuclei volume fraction increased (Figure 28b), indicating that more nuclei volume is packed within a certain tissue volume.

Compression was suggested to occur in the middle of the pouch as growth progresses (Aegerter-Wilmsen et al., 2012). To approximate nuclei compression, the contact between nuclei was measured by quantifying the contact area of a nucleus with its neighbours relative to its surface area (Figure 29). The higher the relative contact, the more deformed and compressed nuclei appeared (Figure 29). Relative contact was spatially uniform across the samples (Figure 30a) and seemed higher in 5-day samples (Figure 30). Increasing contact was due to increasing number of neighbours, as the contact surface per neighbour was spatially uniform and the same across samples (Figure 30b). This indicated that nuclei gain contact by increasing their number of neighbours.

Using the apical distance, the distribution of nuclear volume (Figure 31) and contact (Figure 32) could also be measured along the apical basal-axis. Because nuclei undergo IKNM (Okamoto et al., 2013, Strzyz et al., 2015), bigger nuclei might predominantly be more basal than recently divided nuclei. Nuclei volume was, however, independent of apical distance (Figure 31). Further, nuclei might be more closely packed at the apical domain. Yet, contact between nuclei was also independent of apical distance (Figure 32). These results indicate that nuclei are packed uniformly in all dimensions and equilibrate their total volume distribution.

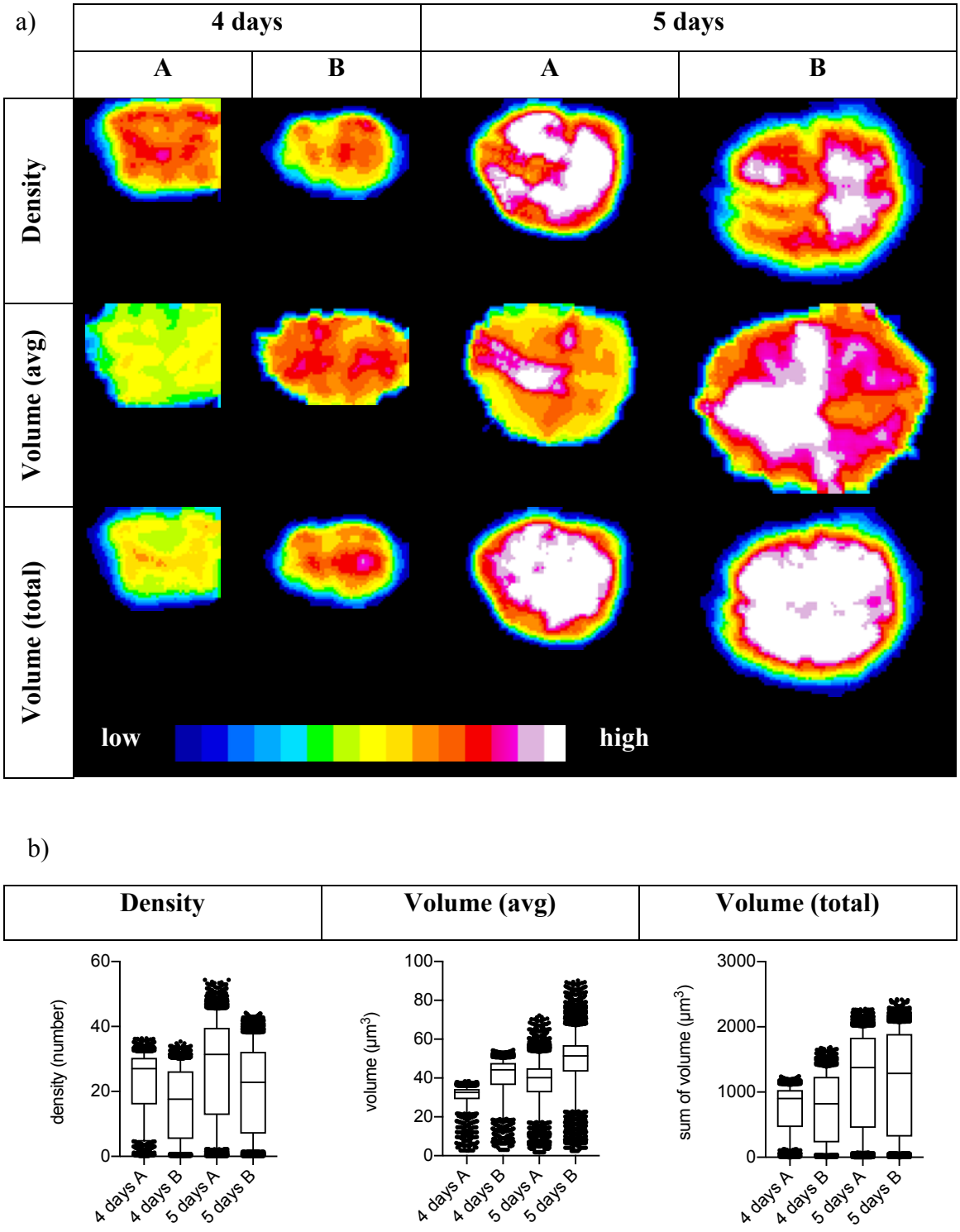


Figure 26: Total nuclei volume increases. a) Heatmaps of 4-day and 5-day samples with anterior left and posterior right. b) Quantification of heatmaps.

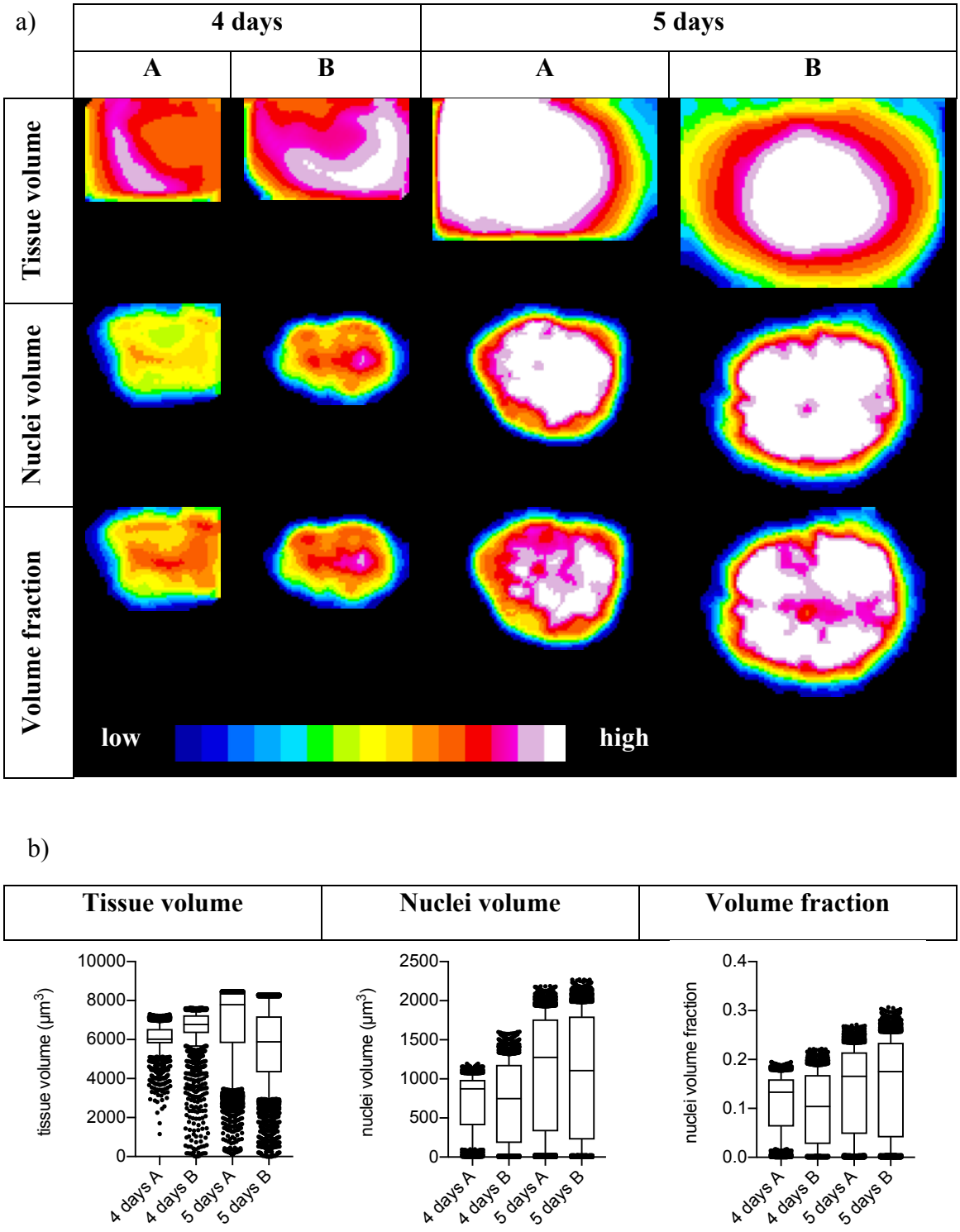
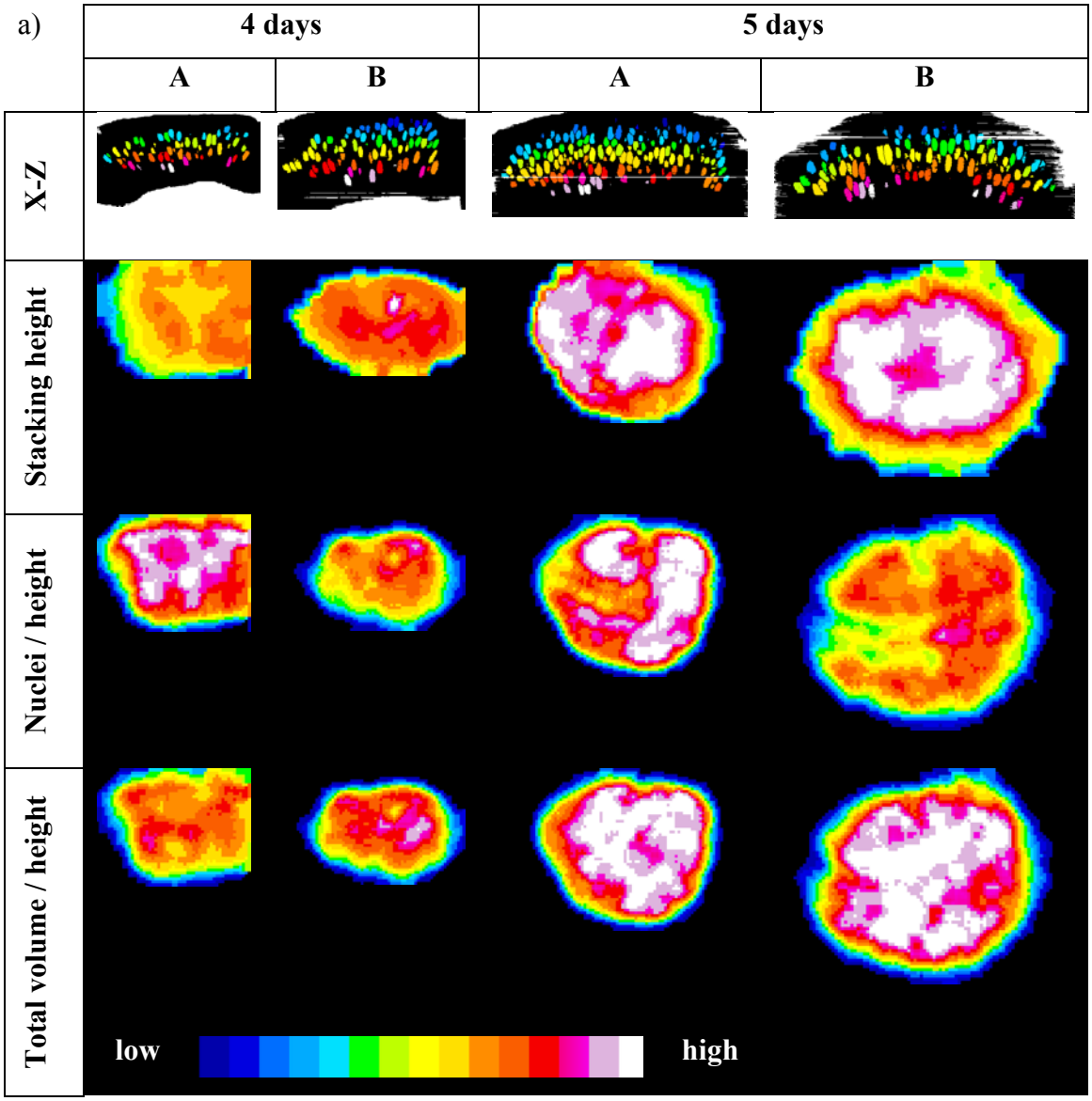


Figure 27: Nuclei volume fraction increased. a) Heatmaps of 4-day and 5-day samples with anterior left and posterior right. b) Quantification of heatmaps.

a)


4 days
5 days
A
B
A
B
X-Z
Stacking height
Nuclei / height
Total volume / height
low
high

b)

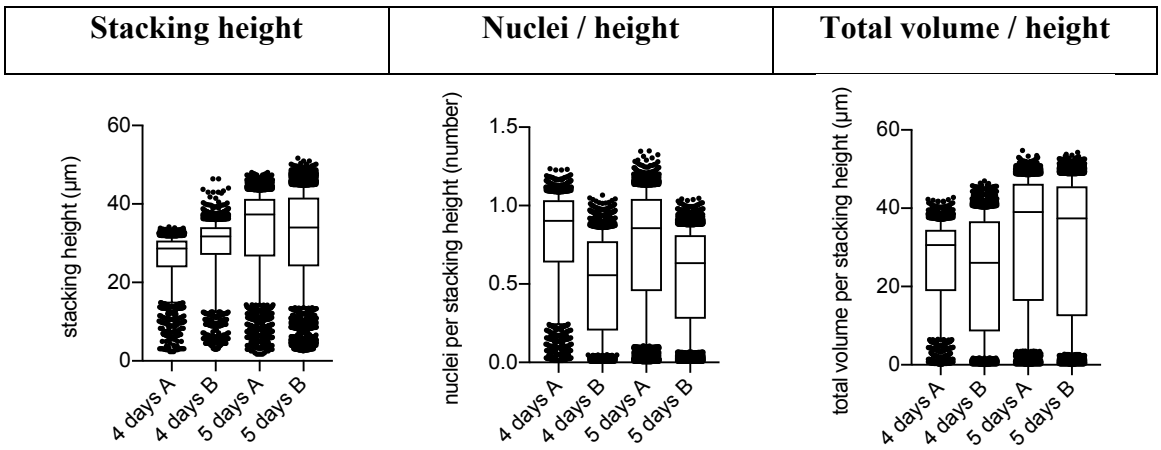

Stacking height
Nuclei / height
Total volume / height
stacking height (µm)
nuclei per stacking height (number)
total volume per stacking height (µm)
4 days A
4 days B
5 days A
5 days B

Figure 28: (previous page) Total nuclei volume per stacking height increased. a) Cross-sections of segmented nuclei coloured in relative apical distance. Heatmaps of 4-day and 5-day samples with anterior left and posterior right. b) Quantification of heatmaps.

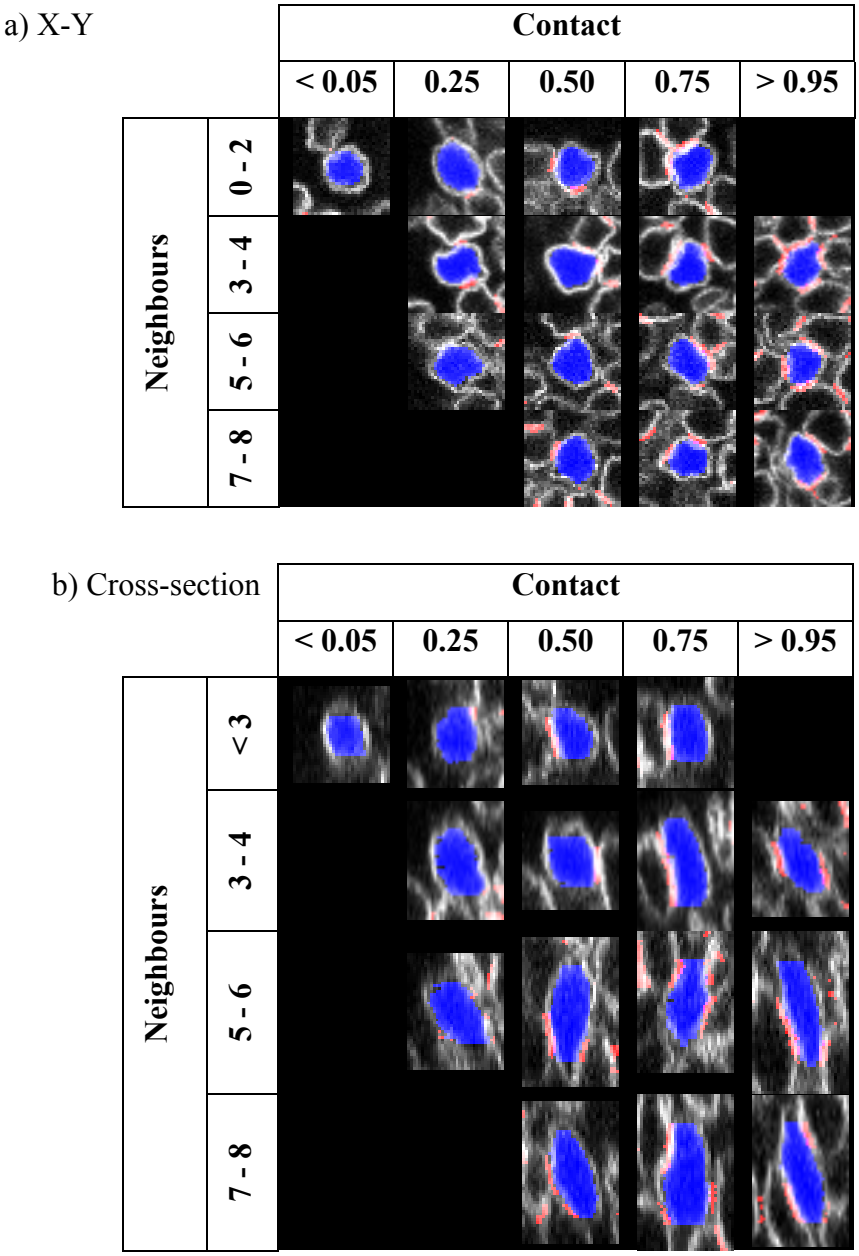
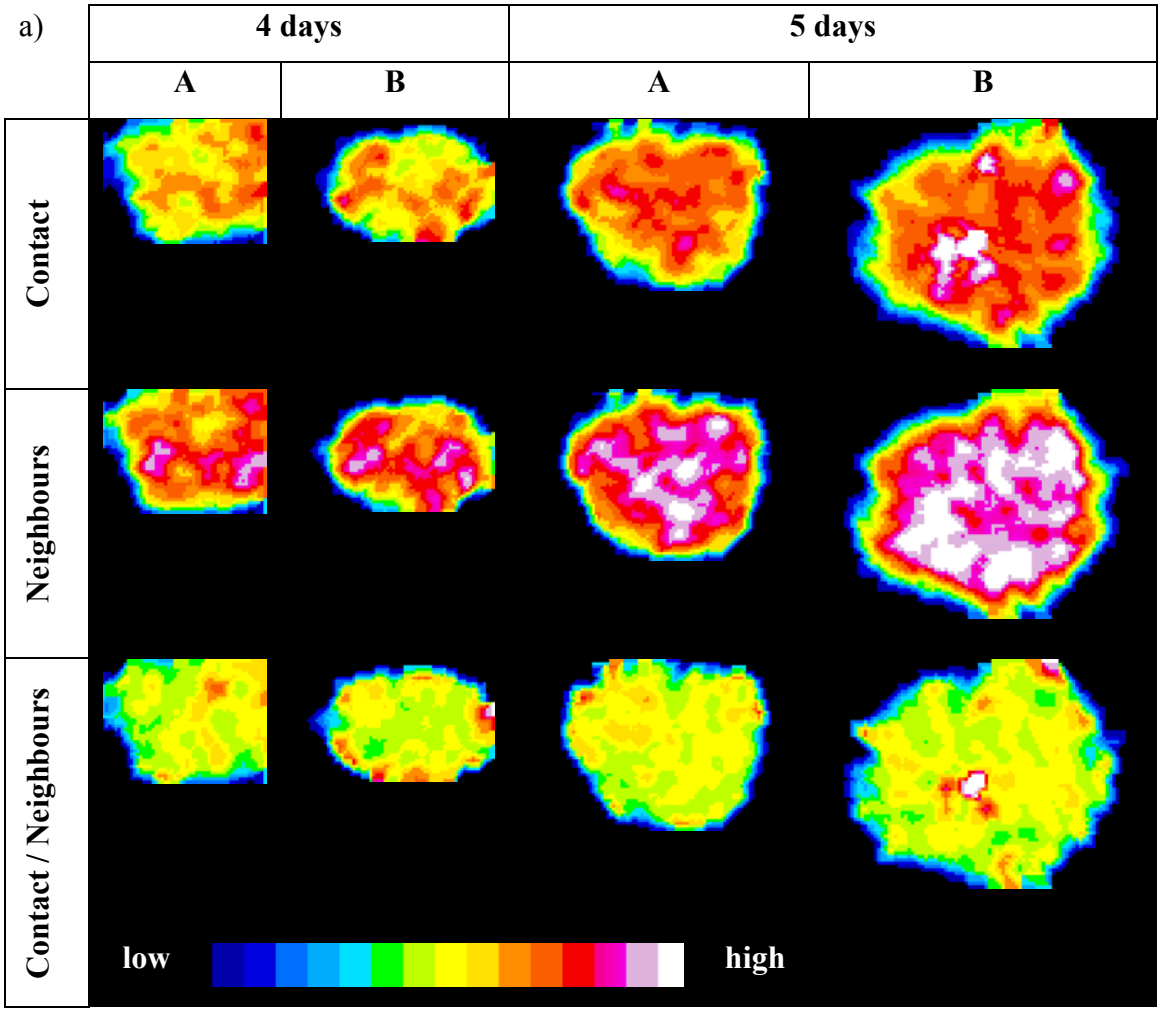


Figure 29: Contact of nuclei for 5 days A. Contact surface of nuclei was calculated by the ratio of contact surface to nuclei surface. Random examples from each timepoint was chosen. Blue indicates the nucleus and red the contact surface. a) X-Y section. b) Cross-section.



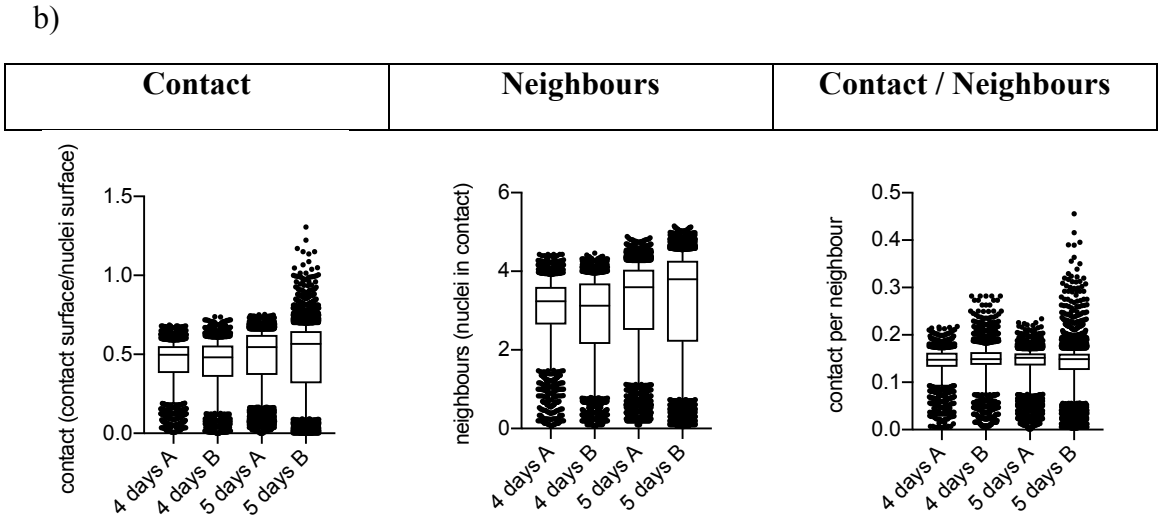


Figure 30: Nuclei contact increased. a) Heatmaps of 4-day and 5-day samples with anterior left and posterior right. b) Quantification of heatmaps.

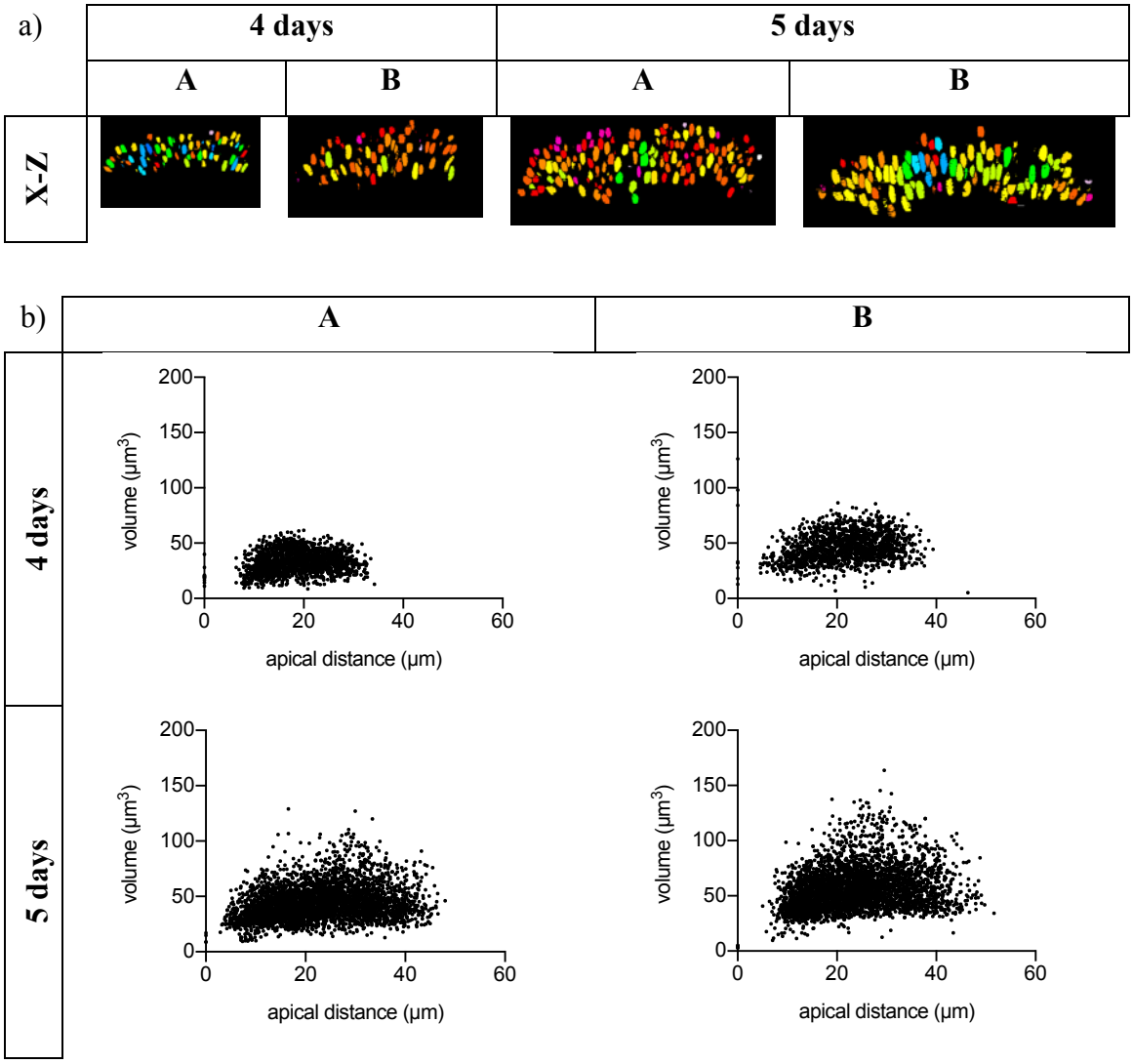


Figure 31: Nuclei volume was independent of apical distance. a) Cross-section of segmented nuclei coloured in relative nuclei volume. b) Apical distance versus average volume. Values taken from individual nuclei.

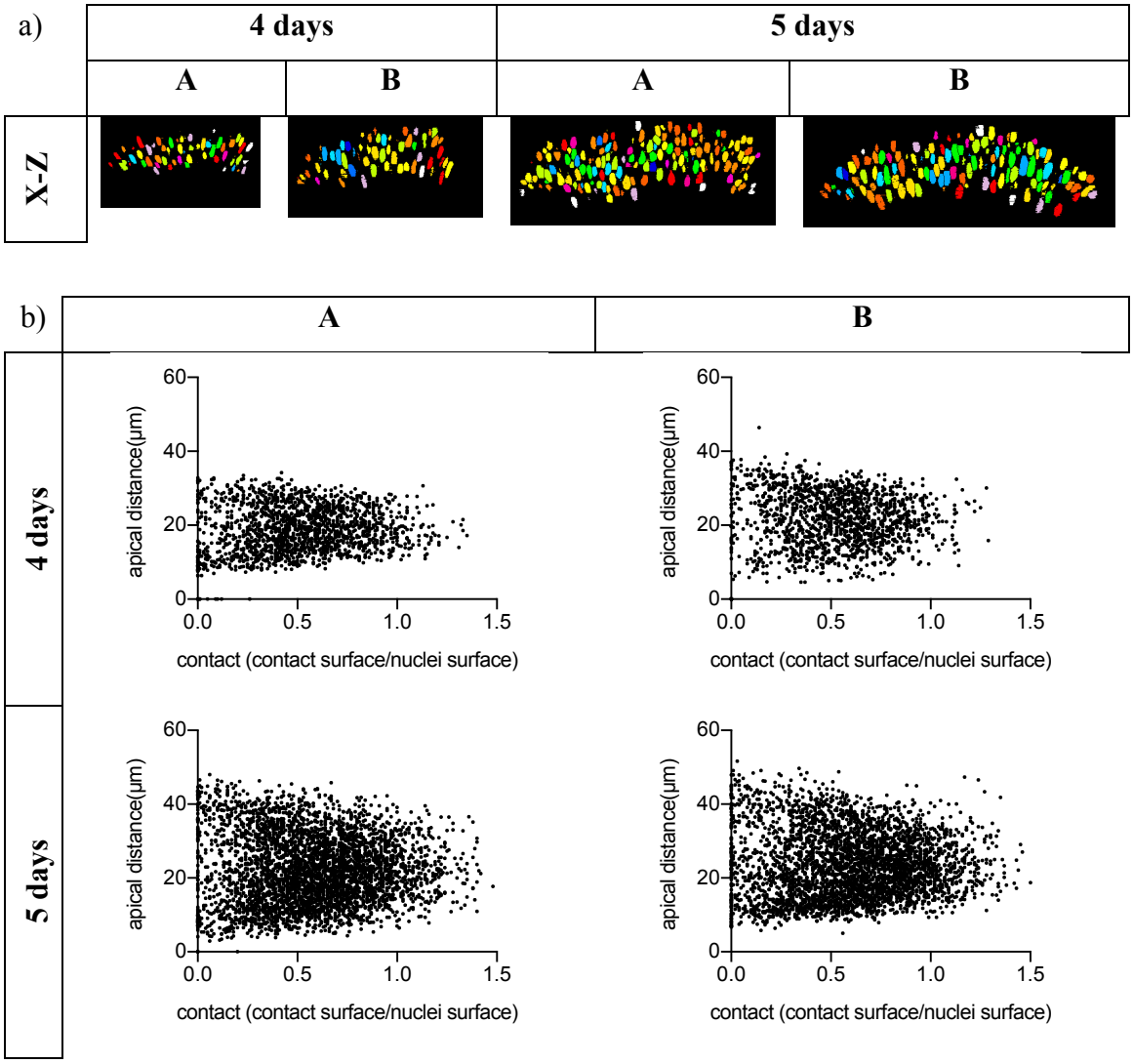


Figure 32: Contact was independent of apical distance. a) Cross-section of segmented nuclei coloured in relative nuclei contact. b) Apical distance versus compactness. Values taken from individual nuclei.

4. Discussion

My ambition was to extract nuclei packing parameters on a tissue-wide scale. The developed segmentation method could extract nuclei densities, volumes and positions from the pouch regions of mid and late third instar wing imaginal discs. My aim was to estimate mechanical compression during development and test the model that compression could contribute to the termination of growth (Aegerter-Wilmsen et al., 2012, Mao et al., 2013). Compression of nuclei might affect chromosome organisation (Wang et al., 2017) and thus cell proliferation (Versaevel et al., 2012). Interestingly, the measurements showed that nuclei volume fractions increased and contact between nuclei was closer. Studies in the neural epithelium of various species (Okamoto et al., 2013, Okamoto et al., 2014, Strzyz et al., 2015, Strzyz et al., 2016), but also of wing imaginal discs (Meyer et al., 2011), highlighted the requirement of nuclei to undergo IKNM for cell division to maintain tissue integrity. Nuclei packing might therefore be crucial to enable efficient IKNM.

The spatial nuclei volume distribution indicated that nuclei volume could reflect the cell cycle stage. Further, nuclei densities and volume complemented each other; nuclei were smaller at high densities and vice versa. The total nuclei volume was therefore spatially uniformly distributed, indicating that nuclei packed efficiently to equilibrate their volume. Nuclei volume and contact was also independent of their apical-basal positions, suggesting that packing of the total volume is equilibrated and uniform in all dimensions. Thus, in contrast to prevailing proposals that cells are primarily compressed in the middle of the pouch (Aegerter-Wilmsen et al., 2012), nuclei might be uniformly compressed as growth progresses. Closer packing of nuclei and uniform compression could act as a "roadblock" for IKNM (Figure 33) and might cause an increase in cell cycle length by steric hindrance (Okamoto et al., 2013, Okamoto et al., 2014).

The developed imaging and processing pipeline utilised conventional confocal microscopy and provided a user-friendly interface to acquire images of thick tissue samples and to segment and quantify nuclei in 3D. The pipeline might therefore be broadly applicable to analyse cell packing in other imaginal discs of the *Drosophila* larva or, for example, the cellular composition of *in vitro* cultured tumour spheroids (Evans, 2015).

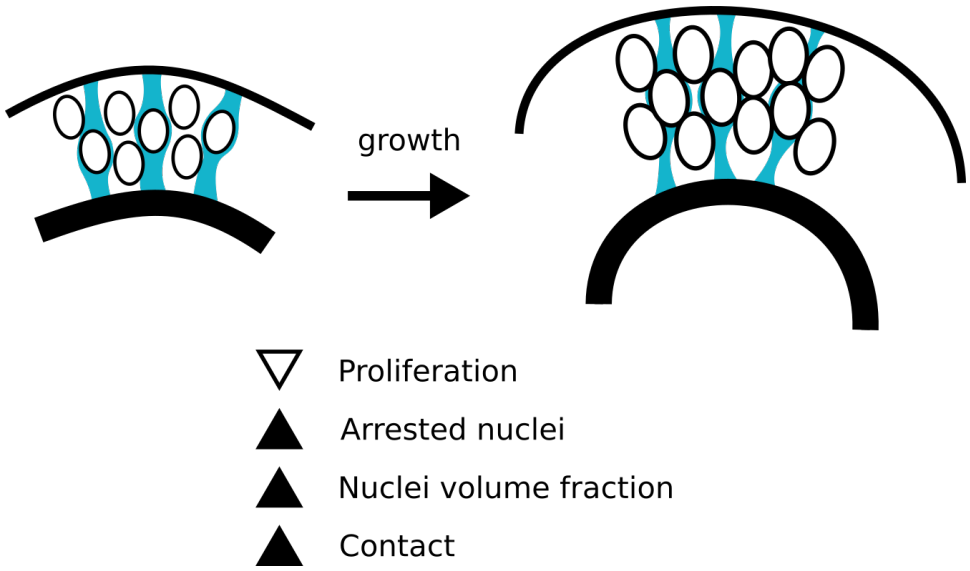


Figure 33: Nuclei pack uniformly closer during growth. As tissue growth proceeds, cells decrease in proliferation and arrest their cell cycle which causes an overall increase in nuclear volume. Tissue volume and stacking height does not increase proportionally to total nuclei volume resulting in an increasing nuclei volume fraction and closer contact. Total nuclei volume is uniformly distributed in all dimensions therefore compression forces might be equilibrated. This close packing could contribute to growth termination.

4.1. Nuclear volume has to be normalised

We hypothesised that nuclei could get deformed and decrease in volume as the compression in the pouch region increases (Aegerter-Wilmsen et al., 2012, Mao et al., 2013) and the growth rate decreases at late developmental stages (Johnston and Sanders, 2003). Nuclei numbers and volumes exhibited complementary spatial patterns in 5-day samples. Increased nuclei volume appeared to correlate with a smaller nuclear density and vice versa. Volume could be linked to the cell cycle stage, as cells at the dorsal-ventral boundary of the anterior compartment, which are arrested in G2 (Johnston and Edgar, 1998), showed the maximum volume. At the posterior side, cells arrest in G1 and have a comparatively smaller volume (Neufeld et al., 1998). To more accurately quantify nuclei volume distribution across discs, a cell cycle marker, such as FUCCI (Fluorescent Ubiquitination-based Cell Cycle Indicator) (Zielke et al., 2014), and a coordinate system using landmarks, such as Wingless and Patched expression (Harmansa et al., 2015) or the quadrant enhancer (Zecca and Struhl, 2007), could be used to correct and normalise nuclei volume for cell cycle stage and position. These

measurements could be supplemented with apical cell area measurements to correlate cellular compression to nuclei volume. These measurements could complement previous flow cytometry measurements (Neufeld et al., 1998) while adding information about spatial parameter distributions.

Nuclear volume ranged between 30-50μm^3 for all samples. Nuclear volume is generally believed to scale with cell size (Neumann and Nurse, 2007); however, this might depend on the species and tissue examined. The nucleolus, the major site of ribosome biogenesis, has been proposed to be a better proxy for cell size (Uppaluri et al., 2016). To verify nuclei volume as a proxy for cell volume in this tissue, nuclei and cell volume could be measured by flow cytometry (Rosner et al., 2013) or single cell clones within the disc (Widmann and Dahmann, 2009). Alternatively, using the nuclei data, the length of cells could be approximated using the centre of a nucleus to measure the apical and basal membrane distance. The apical distance of individual nuclei could further be used to quantify the maximum stretching of cells; longer cells might correlate with reduced apical cell area (Miyata et al., 2014). Nuclei position has so far not been considered in these situations but might have significant effects on the cell cycle and therefore tissue thickness.

4.2. The need for a topographical marker

During growth, the wing imaginal disc not only increases in thickness but also develops its characteristic folds (Figure 14a). These folds were used to define the pouch region in late stage samples, but could not be used in earlier samples. A genetic marker such as the quadrant enhancer (Zecca and Struhl, 2007), rotund or nubbin (Rodriguez Dd Ddel et al., 2002) would genetically and unambiguously define the pouch region. Defined tissue regions would aid initial removal of nuclei as well as calculations for nuclei volume fractions. The nuclei volume fraction was approximated by calculating the ratio of nuclei to tissue volume which might be inaccurate because not all nuclei were segmented within the tissue volume. As an alternative, the stacking height was used to define the available space for the total nuclei volume. These measurements might not only reflect nuclei packing, but could also provide an indication of the remaining cellular material. For example, studies comparing mouse and ferret neural epithelia indicated that in the latter less nuclei accumulated apically which correlated with increasing cellular material and apical tissue stiffness (Nagasaka et al., 2016).

To define changes in nuclei volume fractions, a controlled time-course for the growth of wing imaginal discs is necessary. Wing imaginal discs, although synchronised using the

L2-L3 moult, showed differential growth. Differences within 4- and 5-day samples prohibited the binning of samples. A well-timed reference growth curve of pouch volumes would be useful to stage discs according to pouch volume, rather than relying on morphological features, to compare and bin different samples. In this context, measurements of both wing imaginal discs from one individual could be used to account for within-sample variation. Also, the sex of the larvae should be taken into account, as females are generally bigger than males. A pouch specific driver would therefore aid nuclei selection, volume calculations and enhance sample comparison.

4.3. Estimating nuclei shape

Initial observations suggested that nuclei might be compressed with increasing density. *In vitro* tissue culture, showed that cells exert significant forces onto their environment during mitotic rounding (Sorce et al., 2015). Together with IKNM observed in the wing imaginal disc (Meyer et al., 2011) and neuroepithelium of zebrafish (Strzyz et al., 2015) and mouse (Okamoto et al., 2013), these forces and dynamics of nuclei might compress surrounding nuclei causing the observed decrease in rounded shapes. These shape changes could in turn affect chromosome organisation and cell proliferation (Versaevel et al., 2012). Similar compressed nuclei were observed between the less and more dense mouse and ferret neuroepithelium respectively (Okamoto et al., 2014, Nagasaka et al., 2016). My ambition was therefore to quantify nuclei stacking and shape. Due to technical issues, I could not extract these measurements. Instead, the apical distance and contact of nuclei was used to quantify the nuclei volume fraction and approximate how close nuclei pack.

To more accurately quantify shape, the segmentation would need further post-processing to better approximate the shape of the Lamin signal. A “balloon” method, based on expanding active contour fitting, was successfully applied to extract cell shapes in plant tissues (Federici et al., 2012). This method would not only allow a better way to extract shapes, but also compensate for missing membrane signals based on the tension of the active contour. Additionally, nuclei shape could be approximated by fitting ellipses to extract aspect ratios in 3D. Further, heterochromatin formation could be assessed by Heterochromatin Protein 1 staining (Maison and Almouzni, 2004) as it has been shown to increase in compressed nuclei (Versaevel et al., 2012). A recently published framework to extract nuclei shape and texture in histological tissue samples applied correction algorithms to extract the exact shape of nuclei (Verschuuren et al., 2017). While local thresholding and edge correction extracted nuclei

shapes accurately in 2D, the segmentation focussed on sparsely seeded cells and not tightly packed cells as in the wing imaginal disc; closely apposed nuclei could not be separated using this method. Although nuclei shape could not be assessed within this project, it might still be an important parameter to consider to understand optimal packing.

Nuclei shape could not only be used to approximate compression but also inform about the dynamics of nuclear migration. During IKNM nuclei have been proposed to be squeezed up via actomyosin contraction (Meyer et al., 2011, Strzyz et al., 2015), microtubule-dynein motor activity (Hu et al., 2013) or both subsequently (Spear and Erickson, 2012), depending on the thickness of the tissue; thicker tissues require microtubule motors to move nuclei apical until myosin takes over (Miyata et al., 2014). In 1935, Sauer (1935) studied and mapped nuclei shapes in the chick neural tube and tried to align the shapes according to their stages within the cell cycle. He described the characteristic "tear drop" shape of nuclei during apical movement. These shapes could be correlated with the dynamics of the motor and the contraction machinery to extract not only the forces imposed by surrounding nuclei, but also the forces exerted by the cytoskeleton on nuclei during the cell cycle.

4.4. Stacking could limit proliferation efficiency

Another aim was to quantify the stacking of nuclei into distinct layers. This quantification was attempted by counting nuclei in the apical direction of each nucleus. This strategy was however not successful and was not further optimised due to time constraints (data not shown). However, nuclei appeared to be stacked into four and six layers in mid and late stage samples respectively. This measure is an interesting aspect to further measure nuclei packing during growth. Studies in the mouse neuroepithelium showed that nuclei that do not undergo basal migration after mitosis cause apical congestion, leading to cell extrusion and premature maturation of neural progenitors (Okamoto et al., 2013). In a similar manner, if nuclei are closely packed they might not be able to migrate to the next stacking layer and thus have to wait. If this waiting time exceeded a maximum, cells could stop or slow down their cell cycle. To investigate this aspect, nuclei stacking would need to be reliably quantified.

The cell cycle might also determine how many nuclei layers are optimal for proliferation. Different tissues that produce more cells increase in thickness and in nuclei stacking (Miyata et al., 2014, Strzyz et al., 2016). In *Drosophila* wing imaginal discs, activation of dE2F, a transcription factor required for G1/S transition, decreased cell size while repression caused an increase in cell size (Neufeld et al., 1998). dE2F could be used as a tool to modulate

the cell cycle length to test its effects on nuclei packing; speeding up the cell cycle might reduce stacking while slowing it down might increase stacking.

Thickness might however not depend on stacking, as shown by a study in the developing mouse intestine (Grosse et al., 2011). Blocking of cell cycle progression resulted in conversion of the pseudostratified epithelium to columnar organisation, while retaining tissue thickness. Blocking myosin II and microtubules with Blebbistatin and Nocodazole on the other hand, decreased tissue thickness while retaining pseudostratification and, the authors propose, retaining the number of nuclei layers. Cells, however, might fail to stretch out again because they are inhibited in motor activity and therefore forming rounder structures. Cells still undergo mitosis apically with Blebbistatin treatment but are blocked in cell cycle progression with Nocodazole. This study (Grosse et al., 2011) also showed that cell cycle progression is required for nuclei stacking. Cells arrested in S-phase by the DNA crosslinking reagent Mytomycin C caused a columnar organisation. Thus, cell height is not only dependent on stacking, but also the proper functioning of the cytoskeleton.

Whether stacking decreases due to disruption of myosin or actin in the wing imaginal disc has not been investigated. But, for example, disruption of Cdc42, required for actin polarisation, lead to a decrease in cell height (Eaton et al., 1995). How cell cycle speed, which affects cell size (Neufeld et al., 1998), might affect stacking has not been investigated. These experiments are in contrast with studies in the wing imaginal disc, which show that contraction of myosin causes decreasing cell height (Widmann and Dahmann, 2009). Nuclei within these discs still appeared pseudostratified; yet, the authors did not comment or investigate this point. As a control for another tissue, the leg imaginal discs exhibits a similar tight packing of nuclei (McClure and Schubiger, 2005). This comparison could indicate how transferable the measures obtained from the wing imaginal disc are to other tissues.

4.5. Confocal imaging and tissue clearing have limitations

To address these biological questions, the imaging pipeline has to be improved to more accurately capture the 3D packing of nuclei in respect to tissue volume and thickness. The presented pipeline was based on conventional confocal microscopy with a high numerical aperture 63x glycerol objective and used tissue clearing to image through the whole thickness of the pouch. The nuclear signal was sufficient for segmentation within the first 50-60µm which covered most of the nuclei within the pouch. Nuclei at the edge of the dome structure, which appeared tilted in the imaging plane, could not be segmented due to their reduced signal quality. Spherical aberrations, often observed with deep imaging, were not observed using the glycerol objective, which matched the refractory index of the FocusClear reagents.

The nuclei segmentation was however flat at the top and bottom; therefore, nuclei did not assume a well-rounded shape. This could be overcome by imaging from multiple angles, for example with a light-sheet microscope, which would enable imaging from two sides and sample rotation. Two light-sheet systems were tested (home-build and Zeiss Z1; data not shown) but the tissue penetration and voxel resolution of 500nm was less compared to confocal microscopy and the systems were not available long enough for parameter optimisation. A light-sheet system, such as the Zeiss Z1, that is compatible with tissue clearing approaches would be favourable. Tissue embedding enabled the application and exchange of the tissue clearing solution used. Tissue clearing enhanced the signal contrast and homogeneity across the apical-basal axis significantly and was simple compared to other techniques involving different lipid exchange steps or long incubation times (Richardson and Lichtman, 2015). However, the DAPI signal was not usable for segmentation after clearing because its signal was too diffuse. Alternative DNA or nuclear markers could be tested to aid nuclei selection. Although the signal was increased, photo-bleaching was readily observed and the discs could only be sampled once (Supplementary Figure 8).

While the agarose embedding worked well for mid to late stages of wing imaginal disc development, it was difficult to mount earlier discs. Later discs readily sank to the bottom of the agarose drop, while earlier discs had to be encouraged with a tungsten needle by circling around the disc or slight pushing. Tissue embedding enabled the sample to be positioned close to the coverslip to use most of the 280µm working distance of the glycerol objective. Conversely, using spacers and conventional mounting media, the discs sometimes moved during imaging if the sample was not close enough to the coverslip to capture the whole 100-150µm ot the thick sample.

4.6. Strengths and weaknesses of the segmentation

These technical considerations could aid the subsequent segmentation and correction of nuclei. The developed program could segment nuclei with morphological filters and merged them in 3D, as done similarly in *Drosophila* embryos using RACE (Stegmaier et al., 2016). Although the interface I developed enabled convenient nuclei selection, removal and editing, the correction took approximately 1-3 days depending on the sample. This way of processing however enabled visual cross-checking of the results. The resulting segmentation was good enough to extract the described parameters such as densities, volumes and position.

Multiple tools exist to segment cells and nuclei (Dufour et al., 2017, Heller et al., 2016). Different segmentation methods were tested for their ability to extract nuclei, such as RACE (Stegmaier et al., 2016), the machine learning program ilastik (Kreshuk et al., 2011) and EDGE4D (Khan et al., 2014). The difficulty to use established programs, such as Epitools (Heller et al., 2016), was that these programs were optimised for epithelial cells. These cells can be extracted by watershed segmentation as their membranes oppose each other. In my case, the Lamin signal of nuclei represented touching "donut" objects with space in-between. Using watershed, this in-between space was filled when the watershed leaked over the Lamin signal. Morphological filters were simpler and enabled extraction of individual nuclei labels. A set sequence of morphological filters might not apply to all regions of an image because of inhomogeneous signal intensities. In these cases, adaptive binarisation (Su et al., 2013) and local thresholding (Verschuuren et al., 2017) have been used; however, the tissue clearing method enabled imaging with homogenous signal intensities and the chosen morphological filters worked well to extract most nuclei shapes.

Existing programs that are able to extract nuclei, such as RACE (Stegmaier et al., 2016) and EDGE4D (Khan et al., 2014), do not provide an interface to correct the resulting segmentation easily. Epitools (Heller et al., 2016), for example, provides an interface to manually correct seeds and redraw the segmented cell borders. This approach was however not practical to correct thousands of nuclei in an efficient manner. Therefore, I developed an interface to efficiently inspect the segmentation visually. The user can navigate with shortcuts which enabled the deletion of false nuclei within a day. Further, the user has the ability to check the cross-sections of nuclei in a gallery mode and adjust their start and stop planes. This assisted checking of segmented objects has not been implemented in any of the other tested segmentation programs. The developed pipeline therefore supports the segmentation and correction for any 3D object that can be extracted with morphological filters.

The parameters for the morphological filters were tested using smaller samples of one 4-day sample. Most of the program was initially developed using these smaller regions. The main challenge during upscaling of the approach to the whole pouch was to adapt data storage and handling. Nuclei were initially stored in simple lists, which provided convenient access of individual nuclei but prohibited efficient retrieval of, for example, nuclei within a certain spatial range. The data storage was transferred to Pandas data-frames. Most of the processing should be optimised to be run on a clustered server and use threading and concurrent data access. Despite these shortcomings, the processing pipeline was, if not efficient, effective to process the segmentation of nuclei.

The resulting data was visualised and analysed by tiling the segmented imaged into squares and subsequent averaging of the tiles. Nuclei were retrieved based on their positions and the data represented in heatmaps and quantified with respective plots. Due to the low sample number, two samples for 4- and 5-day, most of the observations were qualitative rather than quantitative. Statistical tests were therefore omitted. This approach could however identify the spatial distribution of the extracted features and their general trends.

4.7. Conclusions

The developed imaging pipeline and accompanying segmentation program was able to extract nuclei densities, volumes and positions of 4- and 5-day samples from the pouch regions of *Drosophila* wing imaginal discs. Further improvements have to be made to the pipeline to extract more accurate nuclei shapes and enable more efficient data processing. Despite this, the project was able to highlight the importance of quantifying tissue-wide nuclei parameters. The measurements indicated that nuclei might be uniformly compressed during growth. Nuclei volume distribution and contact between neighbouring nuclei could therefore be important for cell cycle dynamics and growth.

5. References

AEGERTER-WILMSEN, T., AEGERTER, C. M., HAFEN, E. & BASLER, K. 2007. Model for the regulation of size in the wing imaginal disc of Drosophila. *Mech Dev,* 124**,** 318-26.

AEGERTER-WILMSEN, T., HEIMLICHER, M. B., SMITH, A. C., DE REUILLE, P. B., SMITH, R. S., AEGERTER, C. M. & BASLER, K. 2012. Integrating force-sensing and signaling pathways in a model for the regulation of wing imaginal disc size. *Development,* 139**,** 3221-31.

ALDAZ, S., ESCUDERO, L. M. & FREEMAN, M. 2010. Live imaging of Drosophila imaginal disc development. *Proc Natl Acad Sci U S A,* 107**,** 14217-22.

BAFFET, A. D., HU, D. J. & VALLEE, R. B. 2015. Cdk1 Activates Pre-mitotic Nuclear Envelope Dynein Recruitment and Apical Nuclear Migration in Neural Stem Cells. *Dev Cell,* 33**,** 703-16.

BARBIER DE REUILLE, P., ROUTIER-KIERZKOWSKA, A. L., KIERZKOWSKI, D., BASSEL, G. W., SCHUPBACH, T., TAURIELLO, G., BAJPAI, N., STRAUSS, S., WEBER, A., KISS, A., BURIAN, A., HOFHUIS, H., SAPALA, A., LIPOWCZAN, M., HEIMLICHER, M. B., ROBINSON, S., BAYER, E. M., BASLER, K., KOUMOUTSAKOS, P., ROEDER, A. H., AEGERTER-WILMSEN, T., NAKAYAMA, N., TSIANTIS, M., HAY, A., KWIATKOWSKA, D., XENARIOS, I., KUHLEMEIER, C. & SMITH, R. S. 2015. MorphoGraphX: A platform for quantifying morphogenesis in 4D. *Elife,* 4**,** 05864.

BEAUZAMY, L., LOUVEAUX, M., HAMANT, O. & BOUDAOUD, A. 2015. Mechanically, the Shoot Apical Meristem of Arabidopsis Behaves like a Shell Inflated by a Pressure of About 1 MPa. *Front Plant Sci,* 6**,** 1038.

CAMPAS, O., MAMMOTO, T., HASSO, S., SPERLING, R. A., O'CONNELL, D., BISCHOF, A. G., MAAS, R., WEITZ, D. A., MAHADEVAN, L. & INGBER, D. E. 2014. Quantifying cell-generated mechanical forces within living embryonic tissues. *Nat Methods,* 11**,** 183-9.

CHAKRABORTY, A., PERALES, M. M., REDDY, G. V. & ROY-CHOWDHURY, A. K. 2013. Adaptive geometric tessellation for 3D reconstruction of anisotropically developing cells in multilayer tissues from sparse volumetric microscopy images. *PLoS One,* 8**,** e67202.

CHO, S., IRIANTO, J. & DISCHER, D. E. 2017. Mechanosensing by the nucleus: From pathways to scaling relationships. *Journal of Cell Biology,* 216**,** 305-315.

CHUNG, K., WALLACE, J., KIM, S. Y., KALYANASUNDARAM, S., ANDALMAN, A. S., DAVIDSON, T. J., MIRZABEKOV, J. J., ZALOCUSKY, K. A., MATTIS, J., DENISIN, A. K., PAK, S., BERNSTEIN, H., RAMAKRISHNAN, C., GROSENICK, L., GRADINARU, V. & DEISSEROTH, K. 2013. Structural and molecular interrogation of intact biological systems. *Nature,* 497**,** 332-7.

DUFOUR, A. C., JONKER, A. H. & OLIVO-MARIN, J. C. 2017. Deciphering tissue morphodynamics using bioimage informatics. *Philos Trans R Soc Lond B Biol Sci,* 372.

EATON, S., AUVINEN, P., LUO, L., JAN, Y. N. & SIMONS, K. 1995. CDC42 and Rac1 control different actin-dependent processes in the Drosophila wing disc epithelium. *J Cell Biol,* 131**,** 151-64.

ETOURNAY, R., MERKEL, M., POPOVIC, M., BRANDL, H., DYE, N. A., AIGOUY, B., SALBREUX, G., EATON, S. & JULICHER, F. 2016. TissueMiner: A multiscale analysis toolkit to quantify how cellular processes create tissue dynamics. *Elife,* 5.

EVANS, C. L. 2015. Three-dimensional in vitro cancer spheroid models for photodynamic therapy: strengths and opportunities. *Frontiers in Physics,* 3.

FABROWSKI, P., NECAKOV, A. S., MUMBAUER, S., LOESER, E., REVERSI, A., STREICHAN, S., BRIGGS, J. A. & DE RENZIS, S. 2013. Tubular endocytosis drives remodelling of the apical surface during epithelial morphogenesis in Drosophila. *Nat Commun,* 4**,** 2244.

FEDERICI, F., DUPUY, L., LAPLAZE, L., HEISLER, M. & HASELOFF, J. 2012. Integrated genetic and computation methods for in planta cytometry. *Nat Methods,* 9**,** 483-5.

FISH, J. L., DEHAY, C., KENNEDY, H. & HUTTNER, W. B. 2008. Making bigger brains - the evolution of neural-progenitor-cell division. *Journal of Cell Science,* 121**,** 2783-2793.

GARDNER, R. J., HOBOLTH, A., JENSEN, E. B. & SORENSEN, F. B. 2005. Shape discrimination by total curvature, with a view to cancer diagnostics. *J Microsc,* 217**,** 49-59.

GROSSE, A. S., PRESSPRICH, M. F., CURLEY, L. B., HAMILTON, K. L., MARGOLIS, B., HILDEBRAND, J. D. & GUMUCIO, D. L. 2011. Cell dynamics in fetal intestinal epithelium: implications for intestinal growth and morphogenesis. *Development,* 138**,** 4423-32.

HARIHARAN, I. K. 2015. Organ Size Control: Lessons from Drosophila. *Dev Cell,* 34**,** 255-65.

HARMANSA, S., HAMARATOGLU, F., AFFOLTER, M. & CAUSSINUS, E. 2015. Dpp spreading is required for medial but not for lateral wing disc growth. *Nature,* 527**,** 317-22.

HELLER, D., HOPPE, A., RESTREPO, S., GATTI, L., TOURNIER, A. L., TAPON, N., BASLER, K. & MAO, Y. 2016. EpiTools: An Open-Source Image Analysis Toolkit for Quantifying Epithelial Growth Dynamics. *Dev Cell,* 36**,** 103-16.

HILDEBRAND, D. G. C., CICCONET, M., TORRES, R. M., CHOI, W., QUAN, T. M., MOON, J., WETZEL, A. W., SCOTT CHAMPION, A., GRAHAM, B. J., RANDLETT, O., PLUMMER, G. S., PORTUGUES, R., BIANCO, I. H., SAALFELD, S., BADEN, A. D., LILLANEY, K., BURNS, R., VOGELSTEIN, J. T., SCHIER, A. F., LEE, W. A., JEONG, W. K., LICHTMAN, J. W. & ENGERT, F. 2017. Whole-brain serial-section electron microscopy in larval zebrafish. *Nature,* 545**,** 345-349.

HU, D. J., BAFFET, A. D., NAYAK, T., AKHMANOVA, A., DOYE, V. & VALLEE, R. B. 2013. Dynein recruitment to nuclear pores activates apical nuclear migration and mitotic entry in brain progenitor cells. *Cell,* 154**,** 1300-13.

JOHNSON, G. R., BUCK, T. E., SULLIVAN, D. P., ROHDE, G. K. & MURPHY, R. F. 2015. Joint modeling of cell and nuclear shape variation. *Mol Biol Cell,* 26**,** 4046-56.

JOHNSTON, L. A. & EDGAR, B. A. 1998. Wingless and Notch regulate cell-cycle arrest in the developing Drosophila wing. *Nature,* 394**,** 82-4.

JOHNSTON, L. A. & SANDERS, A. L. 2003. Wingless promotes cell survival but constrains growth during Drosophila wing development. *Nat Cell Biol,* 5**,** 827-33.

JONES, A. R., FORERO-VARGAS, M., WITHERS, S. P., SMITH, R. S., TRAAS, J., DEWITTE, W. & MURRAY, J. A. H. 2017. Cell-size dependent progression of the cell cycle creates homeostasis and flexibility of plant cell size. *Nat Commun,* 8**,** 15060.

JULICHER, F. & EATON, S. 2017. Emergence of tissue shape changes from collective cell behaviours. *Semin Cell Dev Biol*.

KHAN, Z., WANG, Y. C., WIESCHAUS, E. F. & KASCHUBE, M. 2014. Quantitative 4D analyses of epithelial folding during Drosophila gastrulation. *Development,* 141**,** 2895-900.

KNUST, E., TEPASS, U. & WODARZ, A. 1993. crumbs and stardust, two genes of Drosophila required for the development of epithelial cell polarity. *Dev Suppl***,** 261-8.
KRAYNIK, A. M., REINELT, D. A. & VAN SWOL, F. 2003. Structure of random monodisperse foam. *Phys Rev E Stat Nonlin Soft Matter Phys,* 67**,** 031403.
KRESHUK, A., KOETHE, U., PAX, E., BOCK, D. D. & HAMPRECHT, F. A. 2014. Automated detection of synapses in serial section transmission electron microscopy image stacks. *PLoS One,* 9**,** e87351.
KRESHUK, A., STRAEHLE, C. N., SOMMER, C., KOETHE, U., CANTONI, M., KNOTT, G. & HAMPRECHT, F. A. 2011. Automated detection and segmentation of synaptic contacts in nearly isotropic serial electron microscopy images. *PLoS One,* 6**,** e24899.
LESTY, C., RAPHAEL, M., NONNENMACHER, L. & BINET, J. L. 1989. Two statistical approaches to nuclei shape and size in a morphometric description of lymph node sections in non-Hodgkin's lymphoma. *Cytometry,* 10**,** 28-36.
LEUNG, L., KLOPPER, A. V., GRILL, S. W., HARRIS, W. A. & NORDEN, C. 2011. Apical migration of nuclei during G2 is a prerequisite for all nuclear motion in zebrafish neuroepithelia. *Development,* 138**,** 5003-13.
MAISON, C. & ALMOUZNI, G. 2004. HP1 and the dynamics of heterochromatin maintenance. *Nat Rev Mol Cell Biol,* 5**,** 296-304.
MANDARAVALLY MADHAVAN, M. & SCHNEIDERMAN, H. A. 1977. Histological analysis of the dynamics of growth of imaginal discs and histoblast nests during the larval development ofDrosophila melanogaster. *Wilehm Roux Arch Dev Biol,* 183**,** 269-305.
MAO, Y., TOURNIER, A. L., HOPPE, A., KESTER, L., THOMPSON, B. J. & TAPON, N. 2013. Differential proliferation rates generate patterns of mechanical tension that orient tissue growth. *EMBO J,* 32**,** 2790-803.
MCCLURE, K. D. & SCHUBIGER, G. 2005. Developmental analysis and squamous morphogenesis of the peripodial epithelium in Drosophila imaginal discs. *Development,* 132**,** 5033-42.
MEABURN, K. J. 2016. Spatial Genome Organization and Its Emerging Role as a Potential Diagnosis Tool. *Front Genet,* 7**,** 134.
MEYER, E. J., IKMI, A. & GIBSON, M. C. 2011. Interkinetic nuclear migration is a broadly conserved feature of cell division in pseudostratified epithelia. *Curr Biol,* 21**,** 485-91.
MIYATA, T., OKAMOTO, M., SHINODA, T. & KAWAGUCHI, A. 2014. Interkinetic nuclear migration generates and opposes ventricular-zone crowding: insight into tissue mechanics. *Front Cell Neurosci,* 8**,** 473.
NAGASAKA, A., SHINODA, T., KAWAUE, T., SUZUKI, M., NAGAYAMA, K., MATSUMOTO, T., UENO, N., KAWAGUCHI, A. & MIYATA, T. 2016. Differences in the Mechanical Properties of the Developing Cerebral Cortical Proliferative Zone between Mice and Ferrets at both the Tissue and Single-Cell Levels. *Front Cell Dev Biol,* 4**,** 139.
NEUFELD, T. P., DE LA CRUZ, A. F., JOHNSTON, L. A. & EDGAR, B. A. 1998. Coordination of growth and cell division in the Drosophila wing. *Cell,* 93**,** 1183-93.
NEUMANN, F. R. & NURSE, P. 2007. Nuclear size control in fission yeast. *J Cell Biol,* 179**,** 593-600.
NIKOLAOU, N., LOWE, A. S., WALKER, A. S., ABBAS, F., HUNTER, P. R., THOMPSON, I. D. & MEYER, M. P. 2012. Parametric functional maps of visual inputs to the tectum. *Neuron,* 76**,** 317-24.
NORDEN, C. 2017. Pseudostratified epithelia - cell biology, diversity and roles in organ formation at a glance. *J Cell Sci,* 130**,** 1859-1863.

OKAMOTO, M., NAMBA, T., SHINODA, T., KONDO, T., WATANABE, T., INOUE, Y., TAKEUCHI, K., ENOMOTO, Y., OTA, K., ODA, K., WADA, Y., SAGOU, K., SAITO, K., SAKAKIBARA, A., KAWAGUCHI, A., NAKAJIMA, K., ADACHI, T., FUJIMORI, T., UEDA, M., HAYASHI, S., KAIBUCHI, K. & MIYATA, T. 2013. TAG-1-assisted progenitor elongation streamlines nuclear migration to optimize subapical crowding. *Nature Neuroscience,* 16**,** 1556-1566.

OKAMOTO, M., SHINODA, T., KAWAUE, T., NAGASAKA, A. & MIYATA, T. 2014. Ferret-mouse differences in interkinetic nuclear migration and cellular densification in the neocortical ventricular zone. *Neuroscience Research,* 86**,** 88-95.

OSTEN, P. & MARGRIE, T. W. 2013. Mapping brain circuitry with a light microscope. *Nat Methods,* 10**,** 515-23.

PAN, Y., HEEMSKERK, I., IBAR, C., SHRAIMAN, B. I. & IRVINE, K. D. 2016. Differential growth triggers mechanical feedback that elevates Hippo signaling. *Proc Natl Acad Sci U S A*.

PHILIP, J. T. & DAHL, K. N. 2008. Nuclear mechanotransduction: Response of the lamina to extracellular stress with implications in aging. *Journal of Biomechanics,* 41**,** 3164-3170.

POWER, R. M. & HUISKEN, J. 2017. A guide to light-sheet fluorescence microscopy for multiscale imaging. *Nat Methods,* 14**,** 360-373.

RAJASEKARAN, B., URIU, K., VALENTIN, G., TINEVEZ, J. Y. & OATES, A. C. 2016. Object Segmentation and Ground Truth in 3D Embryonic Imaging. *PLoS One,* 11**,** e0150853.

RICHARDSON, D. S. & LICHTMAN, J. W. 2015. Clarifying Tissue Clearing. *Cell,* 162**,** 246-57.

RODRIGUEZ DD DDEL, A., TERRIENTE, J., GALINDO, M. I., COUSO, J. P. & DIAZ-BENJUMEA, F. J. 2002. Different mechanisms initiate and maintain wingless expression in the Drosophila wing hinge. *Development,* 129**,** 3995-4004.

ROHDE, G. K., RIBEIRO, A. J. S., DAHL, K. N. & MURPHY, R. F. 2008. Deformation-based nuclear morphometry: Capturing nuclear shape variation in HeLa cells. *Cytometry Part A,* 73a**,** 341-350.

ROSNER, M., SCHIPANY, K. & HENGSTSCHLAGER, M. 2013. Merging high-quality biochemical fractionation with a refined flow cytometry approach to monitor nucleocytoplasmic protein expression throughout the unperturbed mammalian cell cycle. *Nat Protoc,* 8**,** 602-26.

RUJANO, M. A., SANCHEZ-PULIDO, L., PENNETIER, C., LE DEZ, G. & BASTO, R. 2013. The microcephaly protein Asp regulates neuroepithelium morphogenesis by controlling the spatial distribution of myosin II. *Nat Cell Biol,* 15**,** 1294-306.

RUSSELL, M. R., LERNER, T. R., BURDEN, J. J., NKWE, D. O., PELCHEN-MATTHEWS, A., DOMART, M. C., DURGAN, J., WESTON, A., JONES, M. L., PEDDIE, C. J., CARZANIGA, R., FLOREY, O., MARSH, M., GUTIERREZ, M. G. & COLLINSON, L. M. 2017. 3D correlative light and electron microscopy of cultured cells using serial blockface scanning electron microscopy. *J Cell Sci,* 130**,** 278-291.

SAUER, F. C. 1935. Mitosis in the neural tube. *The Journal of Comparative Neurology,* 62**,** 377-405.

SCHOENWOLF, G. C. & ALVAREZ, I. S. 1989. Roles of neuroepithelial cell rearrangement and division in shaping of the avian neural plate. *Development,* 106**,** 427-39.

SHRAIMAN, B. I. 2005. Mechanical feedback as a possible regulator of tissue growth. *Proc Natl Acad Sci U S A,* 102**,** 3318-23.

SMART, I. H. 1972a. Proliferative characteristics of the ependymal layer during the early development of the mouse diencephalon, as revealed by recording the number, location, and plane of cleavage of mitotic figures. *J Anat,* 113**,** 109-29.
SMART, I. H. 1972b. Proliferative characteristics of the ependymal layer during the early development of the spinal cord in the mouse. *J Anat,* 111**,** 365-80.
SORCE, B., ESCOBEDO, C., TOYODA, Y., STEWART, M. P., CATTIN, C. J., NEWTON, R., BANERJEE, I., STETTLER, A., ROSKA, B., EATON, S., HYMAN, A. A., HIERLEMANN, A. & MULLER, D. J. 2015. Mitotic cells contract actomyosin cortex and generate pressure to round against or escape epithelial confinement. *Nat Commun,* 6**,** 8872.
SPEAR, P. C. & ERICKSON, C. A. 2012. Apical movement during interkinetic nuclear migration is a two-step process. *Dev Biol,* 370**,** 33-41.
STEGMAIER, J., AMAT, F., LEMON, W. C., MCDOLE, K., WAN, Y., TEODORO, G., MIKUT, R. & KELLER, P. J. 2016. Real-Time Three-Dimensional Cell Segmentation in Large-Scale Microscopy Data of Developing Embryos. *Dev Cell,* 36**,** 225-40.
STRASSBURGER, K., LORBEER, F. K., LUTZ, M., GRAF, F., BOUTROS, M. & TELEMAN, A. A. 2017. Oxygenation and adenosine deaminase support growth and proliferation of ex vivo cultured Drosophila wing imaginal discs. *Development*.
STRZYZ, P. J., LEE, H. O., SIDHAYE, J., WEBER, I. P., LEUNG, L. C. & NORDEN, C. 2015. Interkinetic nuclear migration is centrosome independent and ensures apical cell division to maintain tissue integrity. *Dev Cell,* 32**,** 203-19.
STRZYZ, P. J., MATEJCIC, M. & NORDEN, C. 2016. Heterogeneity, Cell Biology and Tissue Mechanics of Pseudostratified Epithelia: Coordination of Cell Divisions and Growth in Tightly Packed Tissues. *Int Rev Cell Mol Biol,* 325**,** 89-118.
SU, B., LU, S. & TAN, C. L. 2013. Robust document image binarization technique for degraded document images. *IEEE Trans Image Process,* 22**,** 1408-17.
TAVERNA, E. & HUTTNER, W. B. 2010. Neural progenitor nuclei IN motion. *Neuron,* 67**,** 906-14.
UPPALURI, S., WEBER, S. C. & BRANGWYNNE, C. P. 2016. Hierarchical Size Scaling during Multicellular Growth and Development. *Cell Rep,* 17**,** 345-352.
VERSAEVEL, M., GREVESSE, T. & GABRIELE, S. 2012. Spatial coordination between cell and nuclear shape within micropatterned endothelial cells. *Nat Commun,* 3**,** 671.
VERSCHUUREN, M., DE VYLDER, J., CATRYSSE, H., ROBIJNS, J., PHILIPS, W. & DE VOS, W. H. 2017. Accurate Detection of Dysmorphic Nuclei Using Dynamic Programming and Supervised Classification. *PLoS One,* 12**,** e0170688.
WANG, Y., NAGARAJAN, M., UHLER, C. & SHIVASHANKAR, G. V. 2017. Orientation and Repositioning of Chromosomes Correlate with Cell Geometry-dependent Gene Expression. *Mol Biol Cell*.
WEBER, I. P., RAMOS, A. P., STRZYZ, P. J., LEUNG, L. C., YOUNG, S. & NORDEN, C. 2014. Mitotic position and morphology of committed precursor cells in the zebrafish retina adapt to architectural changes upon tissue maturation. *Cell Rep,* 7**,** 386-97.
WIDMANN, T. J. & DAHMANN, C. 2009. Dpp signaling promotes the cuboidal-to-columnar shape transition of Drosophila wing disc epithelia by regulating Rho1. *J Cell Sci,* 122**,** 1362-73.
ZECCA, M. & STRUHL, G. 2007. Control of Drosophila wing growth by the vestigial quadrant enhancer. *Development,* 134**,** 3011-20.
ZHENG, Z., LAURITZEN, J. S., PERLMAN, E., ROBINSON, C. G., NICHOLS, M., MILKIE, D., TORRENS, O., PRICE, J., FISHER, C. B., SHARIFI, N., CALLE-SCHULER, S. A., KMECOVA, L., ALI, I. J., KARSH, B., TRAUTMAN, E. T., BOGOVIC, J., HANSLOVSKY, P., JEFFERIS, G. S. X. E., KAZHDAN, M.,

KHAIRY, K., SAALFELD, S., FETTER, R. D. & BOCK, D. D. 2017. A Complete Electron Microscopy Volume Of The Brain Of Adult Drosophila melanogaster. *bioRxiv*.

ZIELKE, N., KORZELIUS, J., VAN STRAATEN, M., BENDER, K., SCHUHKNECHT, G. F., DUTTA, D., XIANG, J. & EDGAR, B. A. 2014. Fly-FUCCI: A versatile tool for studying cell proliferation in complex tissues. *Cell Rep,* 7**,** 588-98.

ZINK, D., FISCHER, A. H. & NICKERSON, J. A. 2004. Nuclear structure in cancer cells. *Nat Rev Cancer,* 4**,** 677-87.

6. Supplementary information

List of Code

Code 1: Initial script to start the segmentation program. 70
Code 2: Configuration for individual segmentations. 70
Code 3: Filter mapping of constants to corresponding classes (filter_mapping.csv). 70
Code 4: Example of filter class (processing/filter.py). 71
Code 5: Defined processing steps and corresponding parameters (processing.csv). 71
Code 6: Applying defined processing steps (processing/image.py). 71
Code 7: Storing of label properties (segmentation.py). 72
Code 8: Setting filter criteria for labels (nuc_seg.ini) 73
Code 9: Nuclei criteria (nuc_criteria.csv). 73
Code 10: Validation of parameter range (segmentation.py). 73
Code 11: Merging labels across planes based on overlap (segmentation.py) 74
Code 12: Calculating overlap (segmentation.py) 75
Code 13: Calculation of relevant nucleus parameters (nuclei.py). 75
Code 14: Applying corrections (correction.py). 78
Code 15: Calculating tissue volume (segmentation.py). 79

List of Supplementary Figures

Supplementary Figure 1: Staging by morphological features of moulting. 80
Supplementary Figure 2: Further examples of initial time-course of wing imaginal disc..... 81
Supplementary Figure 3: Further examples of initial time-course of nuclei. 82
Supplementary Figure 4: Further examples of mounting attempts. 83
Supplementary Figure 5: Examples of successful mounting and common mistakes. 84
Supplementary Figure 6: Examples of construct and anti-body stained discs..... 84
Supplementary Figure 7: Examples of Vectashield, FocusClear only and FocusClear kit. 85
Supplementary Figure 8: Examples of photobleaching after acquiring a narrow stack. 86
Supplementary Figure 9: Remaining wing imaginal discs of the repeated time-course..... 87

6.1. Sequence for Tubulin-Myristoylated-mCherry-2A-Citrine-Lamin

Myristoylated-mCherry-2A-Citrine-GGG-Lamin

ATGGTGAGCAAGGGCGAGGAGGATAACATGGCCATCATCAAGGAGTTCATGCGCTTCAAGGTGCACATGGAGGGC
TCCGTGAACGGCCACGAGTTCGAGATCGAGGGCGAGGGCGAGGGCCGCCCCTACGAGGGCACCCAGACCGCCAAG
CTGAAGGTGACCAAGGGTGGCCCCCTGCCCTTCGCCTGGGACATCCTGTCCCCTCAGTTCATGTACGGCTCCAAG
GCCTACGTGAAGCACCCCGCCGACATCCCCGACTACTTGAAGCTGTCCTTCCCCGAGGGCTTCAAGTGGGAGCGC
GTGATGAACTTCGAGGACGGCGGCGTGGTGACCGTGACCCAGGACTCCTCCCTGCAGGACGGCGAGTTCATCTAC
AAGGTGAAGCTGCGCGGCACCAACTTCCCCTCCGACGGCCCCGTAATGCAGAAGAAGACCATGGGCTGGGAGGCC
TCCTCCGAGCGGATGTACCCCGAGGACGGCGCCCTGAAGGGCGAGATCAAGCAGAGGCTGAAGCTGAAGGACGGC
GGCCACTACGACGCTGAGGTCAAGACCACCTACAAGGCCAAGAAGCCCGTGCAGCTGCCCGGCGCCTACAACGTC
AACATCAAGTTGGACATCACCTCCCACAACGAGGACTACACCATCGTGGAACAGTACGAACGCGCCGAGGGCCGC
CACTCCACCGGCGGCATGGACGAGCTGTACAAGGGCAGTGGAGAGGGCAGAGGAAGTCTGCTAACATGCGGTGAC
GTCGAGGAGAATCCTGGCCCAATGGTGAGCAAGGGCGAGGAGCTGTTCACCGGGGTGGTGCCCATCCTGGTCGAG
CTGGACGGCGACGTAAACGGCCACAAGTTCAGCGTGTCCGGCGAGGGCGAGGGCGATGCCACCTACGGCAAGCTG
ACCCTGAAGTTCATCTGCACCACCGGCAAGCTGCCCGTGCCCTGGCCCACCCTCGTGACCACCTTCGGCTACGGC
CTGATGTGCTTCGCCCGCTACCCCGACCACATGAAGCAGCACGACTTCTTCAAGTCCGCCATGCCCGAAGGCTAC
GTCCAGGAGCGCACCATCTTCTTCAAGGACGACGGCAACTACAAGACCCGCGCCGAGGTGAAGTTCGAGGGCGAC
ACCCTGGTGAACCGCATCGAGCTGAAGGGCATCGACTTCAAGGAGGACGGCAACATCCTGGGGCACAAGCTGGAG
ZTACAACTACAACAGCCACAACGTCTATATCATGGCCGACAAGCAGAAGAACGGCATCAAGGTGAACTTCAAGAT
CCGCCACAACATCGAGGACGGCAGCGTGCAGCTCGCCGACCACTACCAGCAGAACACCCCCATCGGCGACGGCCC
CGTGCTGCTGCCCGACAACCACTACCTGAGCTACCAGTCCAAACTGAGCAAAGACCCCAACGAGAAGCGCGATCA
CATGGTCCTGCTGGAGTTCGTGACCGCCGCCGGGATCACTCTCGGCATGGACGAGCTGTACAAGGGAGGCGGTAT
GTCGAGCAAATCCCGACGTGCTGGCACCGCCACGCCGCAGCCCGGCAACACCTCCACCCCCCGGCCGCCATCGGC
GGGTCCGCAGCCGCCGCCGCCGTCCACTCACTCGCAGACGGCCTCCAGCCCCCTCAGCCCCACCCGGCACTCGCG
CGTGGCCGAGAAGGTGGAGCTGCAGAACCTGAACGATCGCCTGGCCACCTACATTGACCGGGTGCGCAACCTGGA
GACGGAGAACTCCCGCCTCACCATCGAGGTGCAGACCACCAGGGACACGGTCACACGCGAGACCACCAACATCAA
GAACATCTTCGAGGCCGAGCTGCTGGAGACGCGCCGTCTGCTCGATGACACAGCTAGGGATCGCGCTCGTGCCGA
GATCGATATCAAGCGTCTCTGGGAGGAGAACGAGGAGCTCAAGAACAAGCTGGACAAGAAGACCAAGGAGTGCAC
CACTGCTGAGGGCAATGTCCGCATGTACGAGTCGCGCGCCAACGAGCTGAACAACAAATACAACCAGGCCAACGC
CGATCGGAAGAAGCTTAACGAAGACCTGAATGAGGCGCTAAAGGAGCTGGAGAGACTGCGTAAGCAGTTCGAGGA
AACGCGGAAGAACCTGGAACAGGAGACACTGTCGCGCGTTGACCTGGAGAACACCATTCAGAGTCTGCGCGAGGA
GCTCTCGTTCAAGGATCAGATCCATTCGCAGGAGATCAATGAGTCGCGCCGCATCAAACAGACAGAGTATAGCGA
GATCGACGGTCGCCTCAGCTCCGAGTACGATGCCAAGTTGAAGCAGTCGCTGCAGGAGCTGCGCGCCCAGTACGA
GGAGCAGATGCAGATTAATCGCGATGAAATCCAGTCCCTCTACGAGGACAAGATCCAACGACTGCAAGAGGCCGC
CGCACGCACATCCAATTCCACGCACAAGTCCATCGAGGAGCTGCGCTCCACTCGTGTGCGTATCGATGCGCTCAA
CGCCAATATCAACGAACTGGAGCAAGCCAATGCCGACCTCAATGCGCGGATCCGTGATCTGGAGCGCCAGCTGGA
CAACGATCGCGAACGCCACGGTCAAGAGATAGACCTTCTCGAGAAGGAGCTCATTCGGCTGCGCGAAGAGATGAC
GCAACAGCTCAAGGAGTACCAGGACCTTATGGACATCAAGGTCTCCCTGGATTTGGAAATCGCCGCATACGACAA
GCTGCTGGTGGGCGAGGAGGCTCGTTTGAACATCACCCCAGCCACCAACACGGCCACAGTGCAGTCCTTTAGCCA
GTCGCTGCGCAACTCCACGCGAGCCACGCCATCGCGTCGCACTCCCTCTGCTGCCGTGAAGCGCAAACGCGCCGT
GGTCGACGAGTCGGAGGATCACAGCGTCGCCGATTACTATGTGTCCGCCAGTGCCAAGGGCAACGTGGAGATCAA
GGAGATCGATCCCGAGGGCAAGTTCGTAAGGCTGTTCAACAAGGGCAGCGAGGAGGTGGCCATCGGTGGCTGGCA
GCTGCAGCGGCTAATCAACGAGAAAGGTCCTTCGACCACTTACAAGTTCCATCGATCGGTGAGGATCGAGCCAAA
TGGCGTGATCACCGTTTGGTCGGCGGACACCAAGGCCTCGCACGAGCCGCCATCGAGCCTTGTGATGAAGTCACA
GAAGTGGGTCTCCGCCGACAACACTAGGACGATTTTGCTGAACTCCGAGGGCGAGGCCGTGGCCAATCTGGATCG
CATCAAGCGCATTGTGTCCCAACACACATCCTCCTCCCGGCTGAGTCGTCGTCGCAGCGTGACCGCCGTGGACGG
CAATGAGCAGCTCTACCACCAGCAGGGCGATCCTCAGCAGTCAAACGAGAAGTGCGCCATTATGTAA

6.2. Code

Code 1: Initial script to start the segmentation program. In this example, the program would silently process the images, merge nuclei, filter nuclei and show the correction interface.

Line	Code
1	`# define steps`
2	`# 0: do not execute; 1: GUI; 2: silent processing; 3: silent processing and force reload`
3	`processing = dict()`
4	`processing['start'] = 0`
5	`processing['process'] = 2`
6	`processing['merge'] = 2`
7	`processing['nuclei'] = 2`
8	`processing['select'] = 1`

Code 2: Configuration for individual segmentations. Each segmentation was stored with experiment number (N1-19) and the used image (19). The dimensions were defined by setting the minimum and maximum values for X, Y, Z coordinates. The channels were defined as strings.

Line	Code
1	`# ID;exp;date;file;Z-min;Z-max;Y-min;Y-max;X-min;X-max;channels`
2	`N1-19-19;N1-19;20160706;N1-19-20160624-wd72-A0-pouch-iso.tif;0;122;10;497;11;504;DAPI;MEMBRANE;LAMIN`

Code 3: Filter mapping of constants to corresponding classes (filter_mapping.csv). Each row defined a string as identifier, a corresponding function within "processing/filter.py" and the required function parameters.

Line	Code
1	`#Keyword;Class;Params[...]`
2	`EQU;Equalise`
3	`HOM;Homogenise;size`
4	`MED;Median;size`
5	`[...]`

Code 4: Example of filter class (processing/filter.py). Every class had a function "apply" which required an image and corresponding parameters as input and returned the processed image. The example shows a median filter.

Line Code

```
1   class Median(Filter):
2       """
3       Median of the image
4       """
5
6       def apply(self, img, param=None):
7           """
8           see Filter.apply()
9           """
10          return rank.median(img, disk(param['size']))
```

Code 5: Defined processing steps and corresponding parameters (processing.csv). For every experiment, the processing steps were defined by strings and their respective parameters.

Line Code

```
1   #ID;processing-steps[...]
2   N1-19-19;EQU;HOM=10;MED=1;ENH=5;GAUSS=200,n;THR=OTSU,100,3D;
    SKLT;CLS=bin,3;INV=3D;BCOR=3;CONV_BIT=16,3D;LABEL=1,no3D
```

Code 6: Applying defined processing steps (processing/image.py). Processing steps were defined in a list which were iteratively applied to the image data and the result returned.

Line Code

```
1   @staticmethod
2   def apply_filters(processing_steps, image_data, verbose=False):
3       """
4       Apply processing steps to image
5
6       :param processing_steps:
7       :param image_data:
8       :return:
9       """
10
11      # read filter mapping
12      filter_mapping = ImageProcessing.get_filter_mapping()
13
14      [...]
15
16      for step in processing_steps:
17          [...]
18          # get mapping
19          filter_map = filter_mapping[step[0]]
20
21          # initialise class
22          filter_class = eval(filter_map['class'])
23          filter = filter_class()
```

```
24
25          # build parameter list
26          params = dict()
27
28          for param in range(1, len(step)):
29              params[filter_map['params'][param - 1]] = step[param]
30
31          [...]
32
33          # is 3D required for filter?
34          if '3D' in params.keys() and params['3D'] == '3D':
35              filtered_image = filter.apply(filtered_image, params)
36          else:
37              # go through all slices individually
38              for z, frame in enumerate(filtered_image):
39                  filtered_image[z] = filter.apply(frame, params)
40
41          [...]
42
43      return filtered_image
```

Code 7: Storing of label properties (segmentation.py). Label properties were retrieved for each plane in concurrent threads for each plane using the skimage framework.

Line Code

```
1   def get_label_props(self):
2       """
3       Return properties of labels in a list in each plane of the stack
4       :return:
5       """
6       [...]
7           self.stacks.labels_props = list(range(0,
8   len(self.stacks.labels)))
9
10          while z < len(self.stacks.labels):
11              print('\t%i' % z)
12              labels_threads = []
13
14              # start threads
15              for i in range(0, max_threads):
16                  if z < len(self.stacks.labels):
17                      thread =
18  threading.Thread(target=self.get_labels_props_for_z, args=(z,))
19                      thread.start()
20                      labels_threads.append(thread)
21
22                      z += 1
23
24              # wait to finish
25              for thread in labels_threads:
26                  thread.join()
```

Code 8: Setting filter criteria for labels (nuc_seg.ini). Parameters from labels as well as auxiliary properties can be used for filtering labels.

```
Line  Code
1     [FilterCriteria]
2     LABELS = area,circularity,edge_dist
3     NUCLEI = volume,depth,surface,nuc_edge_dist,nuc_proba
```

Code 9: Nuclei criteria (nuc_criteria.csv). Criteria were saved for each segmentation in the format: [min]-[max].

```
Line  Code
1     #Criteria to accept nuclei during segmentation and merging
2     ID;area;circularity;eccentricity;Lamin_donut_ratio;edge_dist;
      volume;depth;surface;nuc_edge_dist;donut_ratio;nuc_proba
3     N1-19-19;20.0-350.0;None-4.0;None;None;2.0-;None;None;
      None;None;None;None
```

Code 10: Validation of parameter range (segmentation.py).

```
Line  Code
1     def is_param_in_criteria_range(self, cur_object, param):
2         """
3         Is the label in range of parameters?
4
5         :param cur_object:
6         :param param:
7         :return:
8         """
9         in_range = True
10
11        if cur_object is not None:
12            if param in cur_object:
13                # too high?
14                if self.nuc_criteria[param]['MAX'] is not None:
15                    if self.nuc_criteria[param]['MAX'] > 0 \
16                        and cur_object[param] >
      self.nuc_criteria[param]['MAX']:
17                        in_range = False
18
19                # too low?
20                if self.nuc_criteria[param]['MIN'] is not None:
21                    if self.nuc_criteria[param]['MIN'] > 0 \
22                        and cur_object[param] <=
      self.nuc_criteria[param]['MIN']:
23                        in_range = False
24        else:
25            in_range = False
26
27        return in_range
```

Code 11: Merging labels across planes based on overlap (segmentation.py).

Line	Code

```
1   def merge_labels(self):
2       """
3       Merge potential nuclei based on their selection criteria
4       :return:
5       """
6       # delete labels that do not fit the selection criteria
7       self.filter_planes()
8       [...]
9
10      # go through stack and merge labels
11      # take one label at a time and merge down
12      # as far you can and delete the labels that
13      # you used on the way
14      for raw_z, plane_labels in enumerate(self.stacks.labels_props):
15          for raw_id, raw_label in enumerate(plane_labels):
16              cur_label = None
17              [...]
18
19              while cur_label is not None:
20                  [...]
21
22                  # set overlap for the next planes
23                  has_overlap = False
24
25                  # get the next label within the merge depth
26                  for y in range((z + 1), (z + cfg.merge_depth + 1)):
27                      if y < len(merge_stack)\
28                              and merge_stack[y] is not None\
29                              and has_overlap is False:
30                          # to store highest overlap for this plane
31                          highest_overlap = -1
32                          highest_overlap_ID = -1
33                          highest_overlap_Z = -1
34
35                          # go through the labels of the next plane
36                          for next_id in range(0, len(merge_stack[y])):
37                              # take a label
38                              next_label = merge_stack[y][next_id]
39                              [...]
40
41                              overlap =
    Segmentation.calc_overlap(self.stacks.labels[0], cur_label,
    next_label)
42
43                              # was this the highest overlap?
44                              if overlap > highest_overlap:
45                                  highest_overlap = overlap
46                                  highest_overlap_ID = next_id
47                                  highest_overlap_Z = y
48
49                              # is the overlap sufficient for merging?
50                              if overlap > cfg.merge_min_overlap:
51                                  # there is an overlap
52                                  has_overlap = True
53
54                                  # create nucleus
```

```
55                                      if nID < 0:
57                                          nID = nuclei.create_nucleus(z,
    cur_label)
58                                      else:
59                                          nuclei.add_to_nucleus(y,
    next_label, nID)
60                                          [...]
61
62          self.set_nuclei(nuclei)
```

Code 12: Calculating overlap (segmentation.py). Overlap is calculated by taking the overlap between two labels and dividing by the smaller area of the two.

Line Code

```
1   @staticmethod
2   def calc_overlap(tpl_img, cur_label, next_label):
3       """
4       Caluclate overlap between two labels
5
6       :param tpl_img:
7       :param cur_label:
8       :param next_label:
9       :return:
10      """
11      # get AND sum
12      AND_sum = Segmentation.calc_AND_img(tpl_img, cur_label,
13  next_label).sum()
14
15      # Calculate overlap
16      min_cur_next = min(cur_label['area'], next_label['area'])
17
18      overlap = (AND_sum / min_cur_next) * 100
19
20      return overlap
```

Code 13: Calculation of relevant nucleus parameters (nuclei.py).

Line Code

```
1   def calc_nucleus_params(self, nID, ext_donuts=False,
2                           ext_apical_dist=True, ext_elps=False,
3                           extended_params=False, classifier_params
4                           =False):
5       """
6       Calculate parameters for nucleus
7
8       :param nID:
9       :param extended_params:
10      :param ext_donuts:
11      :param ext_apical_dist:
12      :param ext_elps:
13      :param extended_params:
14      :param classifier_params:
15      :return:
16      """
17      # volume
```

```
18      nucleus_volume = self.get_nucleus_areas(nID)[:, 1].sum()
19
20      self.set_nucleus_volume(nucleus_volume, nID)
21      [...]
22
23      # calculate direction vector of nucleus
24      vec_top = nucleus_centroids[0]
25      vec_bottom = nucleus_centroids[-1]
26
27      vec_direction = np.array([
28          vec_bottom[0] - vec_top[0],
29          vec_bottom[1] - vec_top[1],
30          vec_bottom[2] - vec_top[2]
31      ])
32
33      # adjust vector to z and prepare for saving
34      if vec_direction[0] > 0:
35          vec_direction = np.array([
36              vec_direction[0]/vec_direction[0],
37              vec_direction[1]/vec_direction[0],
38              vec_direction[2]/vec_direction[0]
39          ])
40
41      self.set_nucleus_direction(vec_direction, nID)
42
43      if ext_apical_dist is True and vec_direction[0] > 0:
44          # calculate apical distance
45          # go from nucleus centre up and check if there is still a
    membrane signal
46          is_in_membrane_dim = True
47          cur_rel_z = 0
48          next_pos = nucleus_centre
49          last_pos_on_membrane = None
50
51          # for counting nuclei_in_direction
52          nuclei_in_direction_list = list()
53
54          while is_in_membrane_dim is True:
55              # is point on membrane signal?
57              if self.segmentation.stacks.membin[next_pos[0],
    next_pos[1], next_pos[2]] > 0:
58                  last_pos_on_membrane = next_pos
59
60              # get the nucleus at this position
61              nID_at_pos = self.get_nID_by_pos(next_pos)
62              if nID_at_pos is not None:
63                  nuclei_in_direction_list.append(nID_at_pos)
64
65              # calculate next position
66              cur_rel_z += 1
67
68              next_pos = (
69                  int(nucleus_centre[0] - (cur_rel_z *
    vec_direction[0])),
70                  int(nucleus_centre[1] - (cur_rel_z *
    vec_direction[1])),
71                  int(nucleus_centre[2] - (cur_rel_z *
    vec_direction[2]))
72              )
73
74              # test if next point is in membrane dimensions
```

```
75              for i in range(3):
76                  if next_pos[i] < 0 or next_pos[i] >=
    self.segmentation.stacks.membin.shape[i]:
77                      is_in_membrane_dim = False
78
79          # calculate distance to last position and nucleus centre
80          apical_distance = self.calc_3D_distance(nucleus_centre,
    last_pos_on_membrane)
81
82          self.set_nucleus_apical_distance(apical_distance, nID)
83
84          # get unique list of nuclei in direction and count
85          nuclei_in_direction_set = set(nuclei_in_direction_list)
86
87          count_offset = 0
88          # remove yourself from the list
89          if nID in nuclei_in_direction_set:
90              count_offset = 1
91
92          nuclei_in_direction_count = len(nuclei_in_direction_set)
93          self.set_nucleus_nuclei_in_direction(
                nuclei_in_direction_count, nID)
```

Code 14: Applying corrections (correction.py).

Line	Code

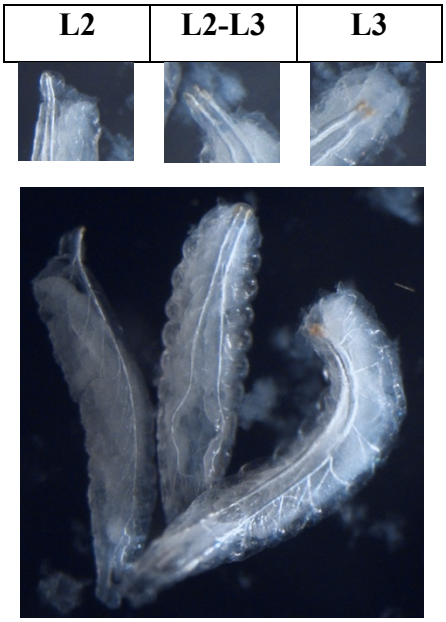
```
1   def apply_corrections(self, save=True, do_remerge=True):
2       """
3       Go through correction lists and apply changes
4
5       :return:
6       """
7       # do remerges
8       if self.corr_remerge is not None and do_remerge is True:
9           print('REMERGE for %i' % len(self.corr_remerge))
10
11          for remerge in self.corr_remerge:
12              # remerge nID
13              if self.segmentation.nuclei.is_nucleus_in_nuclei(remerge)
14                  and
    self.segmentation.nuclei.get_nucleus_volume(remerge) < 0:
15                  self.segmentation.nuclei.remerge_nucleus(remerge, 0,
    (self.segmentation.stacks.Lamin.shape[0] - 1), merge_depth=True,
    force_raw_labels_props=True)
16              else:
17                  print('attemped REMERGE %i' % remerge)
18
19      # resort z values
20      self.segmentation.nuclei.sort_vals_by_z()
21
22      # delete non-nuclei
23      if self.corr_nonuc is not None:
24          print('NONUC for %i' % len(self.corr_nonuc))
25
26          for to_delete in self.corr_nonuc:
27              if
    self.segmentation.nuclei.is_nucleus_in_nuclei(to_delete):
28                  self.segmentation.nuclei.reject_nucleus(to_delete)
29              else:
30                  print('attempted NONUC %i' % to_delete)
31
32      # go through z corrections
33      if self.corr_fila is not None:
34          print('FILA for %i' % len(self.corr_fila))
35
36          for fila in self.corr_fila:
37              # remerge nID
38              if
    self.segmentation.nuclei.is_nucleus_in_nuclei(fila[0]):
39                  self.segmentation.nuclei.remerge_nucleus(fila[0],
    int(float(fila[1][0])), int(float(fila[1][1])),
    force_raw_labels_props=True)  # force to use raw labels
40              else:
41                  print('attemped FILA %i' % fila[0])
42
43      # update segmentation
44      self.segmentation.update(save=save, calc_nuclei_params=False)
45
46      # update stacks
47      self.update_correction_stacks()
```

Code 15: Calculating tissue volume (segmentation.py). Membrane signal was thresholded and the remaining holes filled.

Line	Code

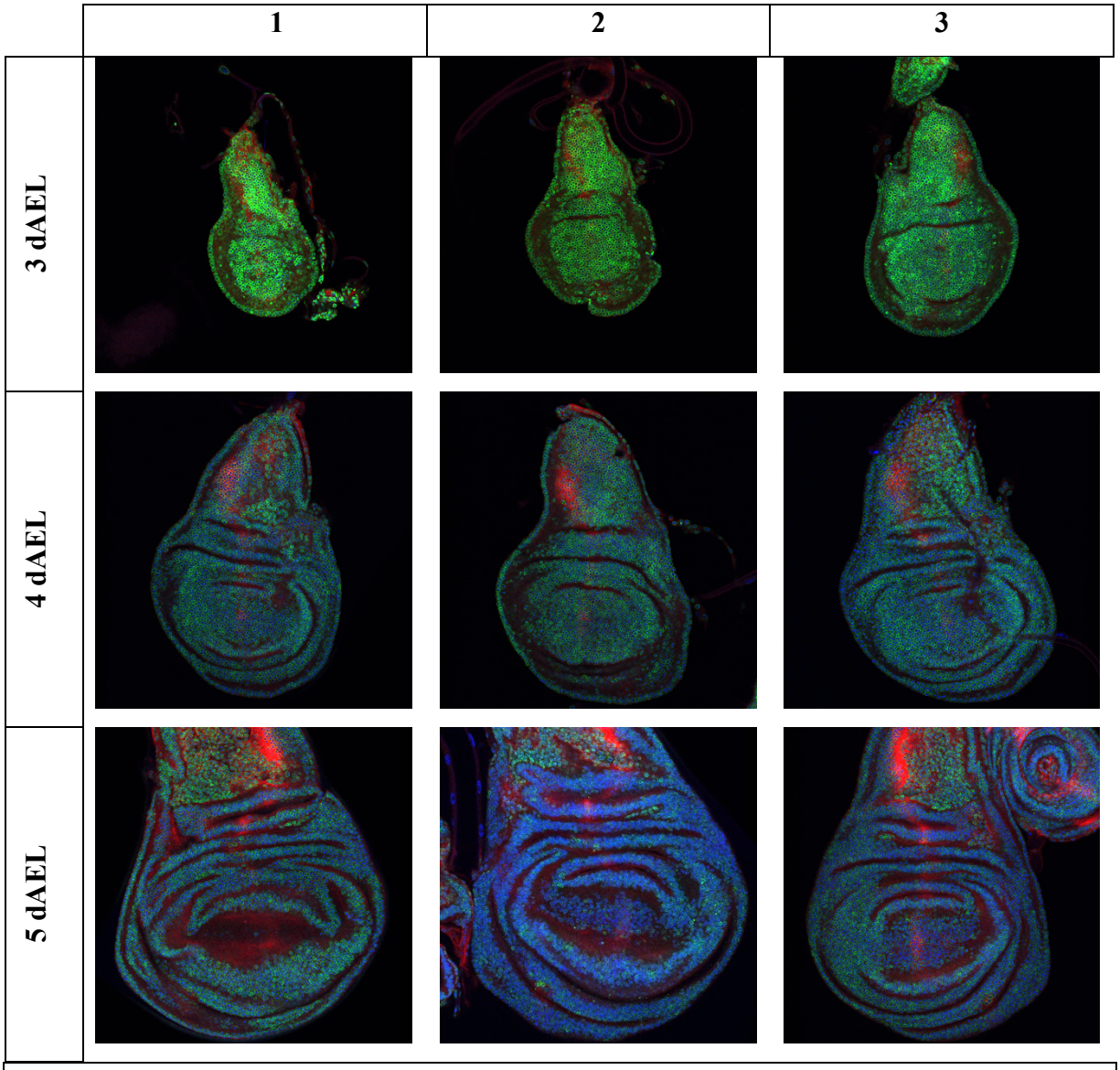
```
1   def create_membin(self):
2       """
3       Create binary version of the membrane channel
4
5       :return:
6       """
7       # define processing steps to create binary membrane mask
8       processing_steps = [
9               ['EQU'],
10              ['THR', 'OTSU', 100, '3D'],
11              ['CLS', 'bin', 2],
12              ['FILL'],
13              ['OPN', 'bin', 2],
14              ['CONV_BIT', 16, '3D']
15      ]
16
17      # apply processing steps
18      self.stacks.membin = ImageProcessing.apply_filters(
19          processing_steps, self.stacks.membrane,
    verbose=cfg.general_verbose)
20
21      ImageHandler.save_stack_as_tiff(self.stacks.membin,
    self.get_results_dir().tmp + cfg.file_stack_membin)
```

6.3. Morphological features of moulting

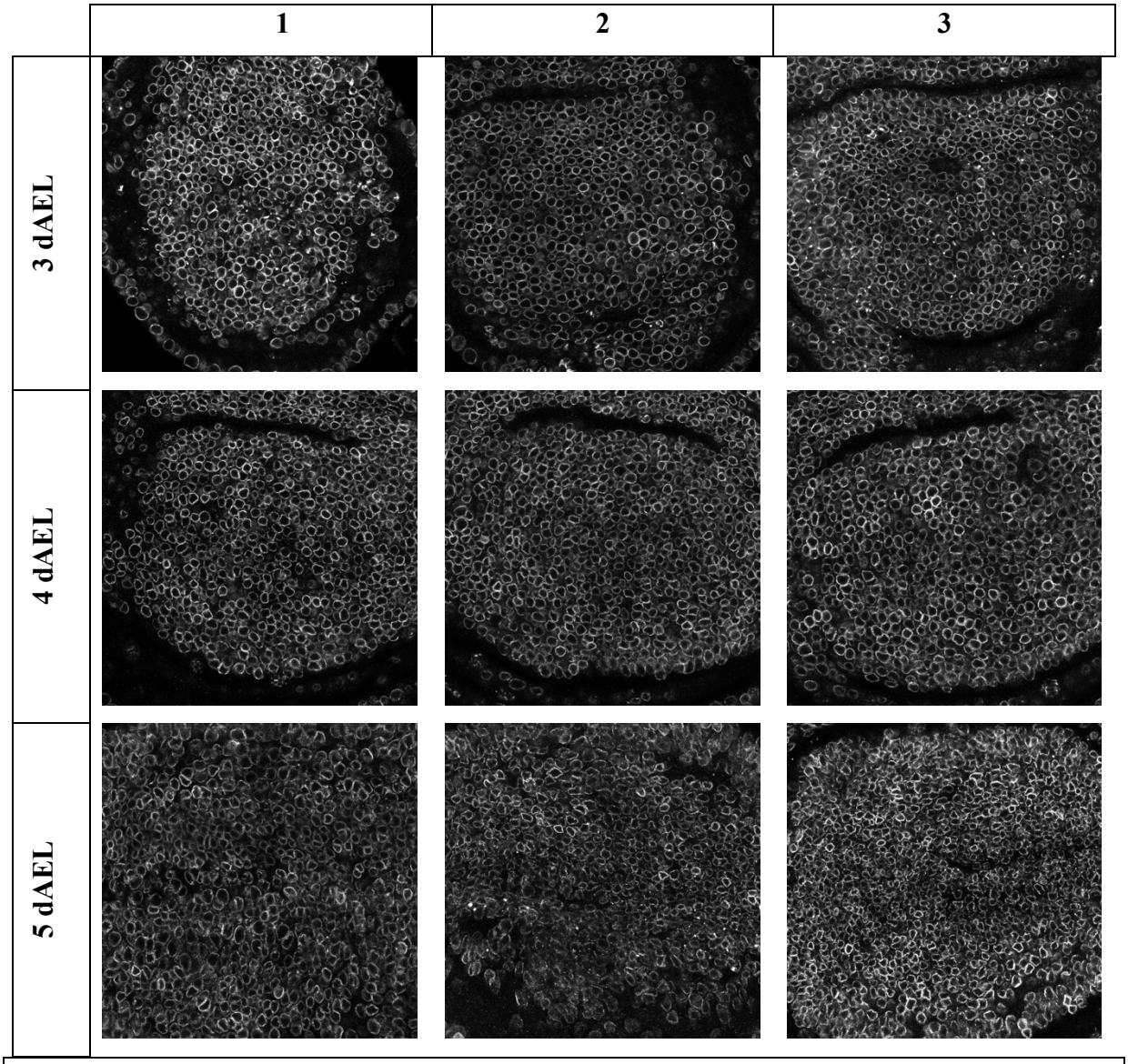


Supplementary Figure 1: Staging by morphological features of moulting. Larvae were staged by using the posterior end as a guide. L2 larvae have a clear posterior, while L3 have a big yellow spot which is beginning to appear in L2-L3 as a yellow "shadow".

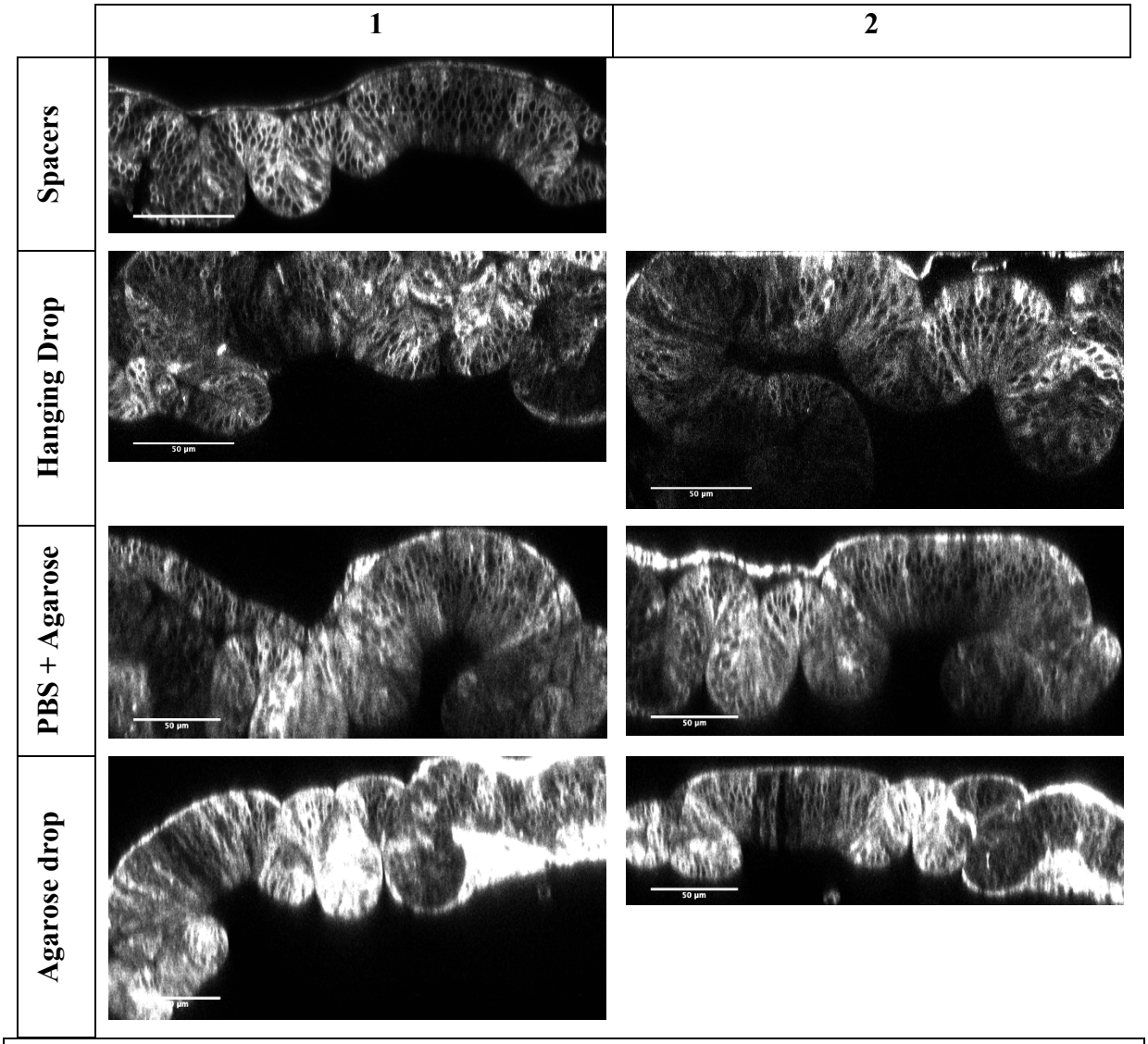
6.4. Images



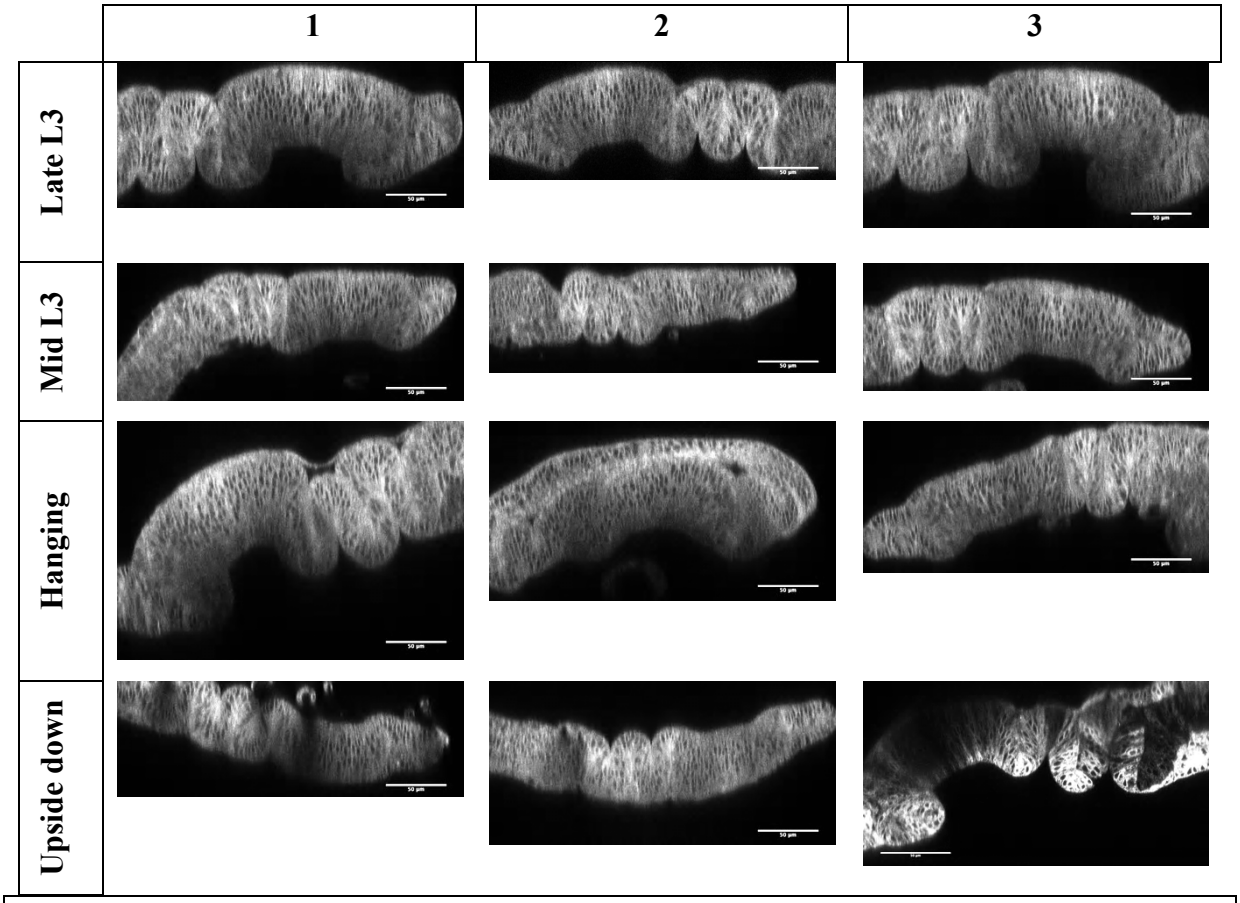
Supplementary Figure 2: Further examples of initial time-course of wing imaginal disc. Myristoylated-mCherry in red, DAPI in blue and anti-Lamin in green.



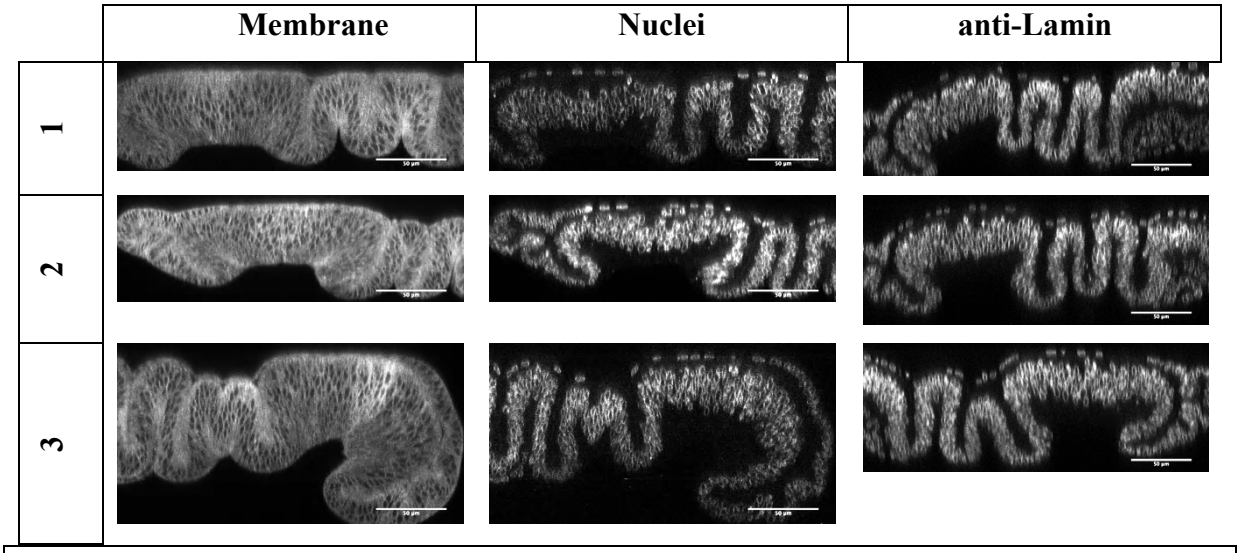
Supplementary Figure 3: Further examples of initial time-course of nuclei. Nuclei stained with Anti-Lamin.



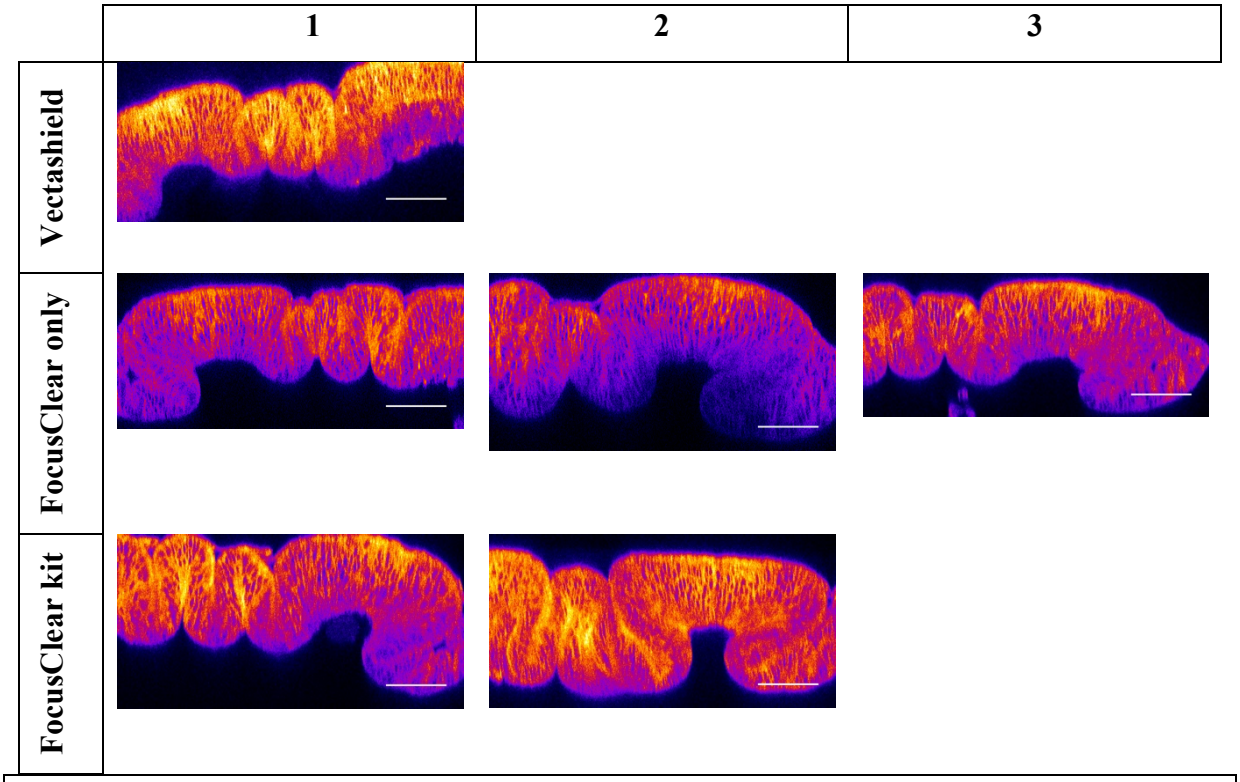
Supplementary Figure 4: Further examples of mounting attempts. Tubulin-Gal4 > UAS-CD8-GFP. Scale bar 50µm.



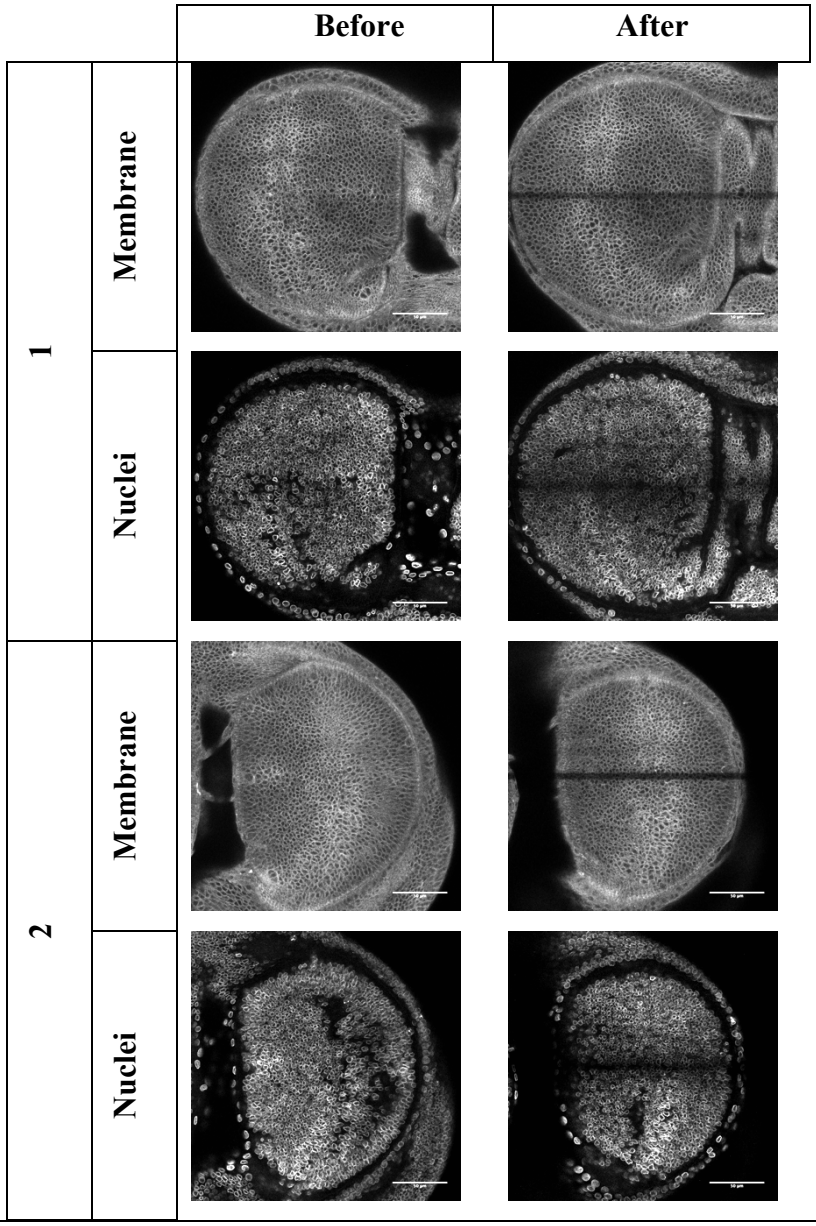
Supplementary Figure 5: Examples of successful mounting and common mistakes. Tubulin-Myristoylated-mCherry or Tubulin-Gal4, UAS-CD8-GFP. Note: the image of the last disc in "Upside down" was flipped highlighting that the signal decreases significantly, if the disc is mounting not with the apical side up. Scale bar 50µm.



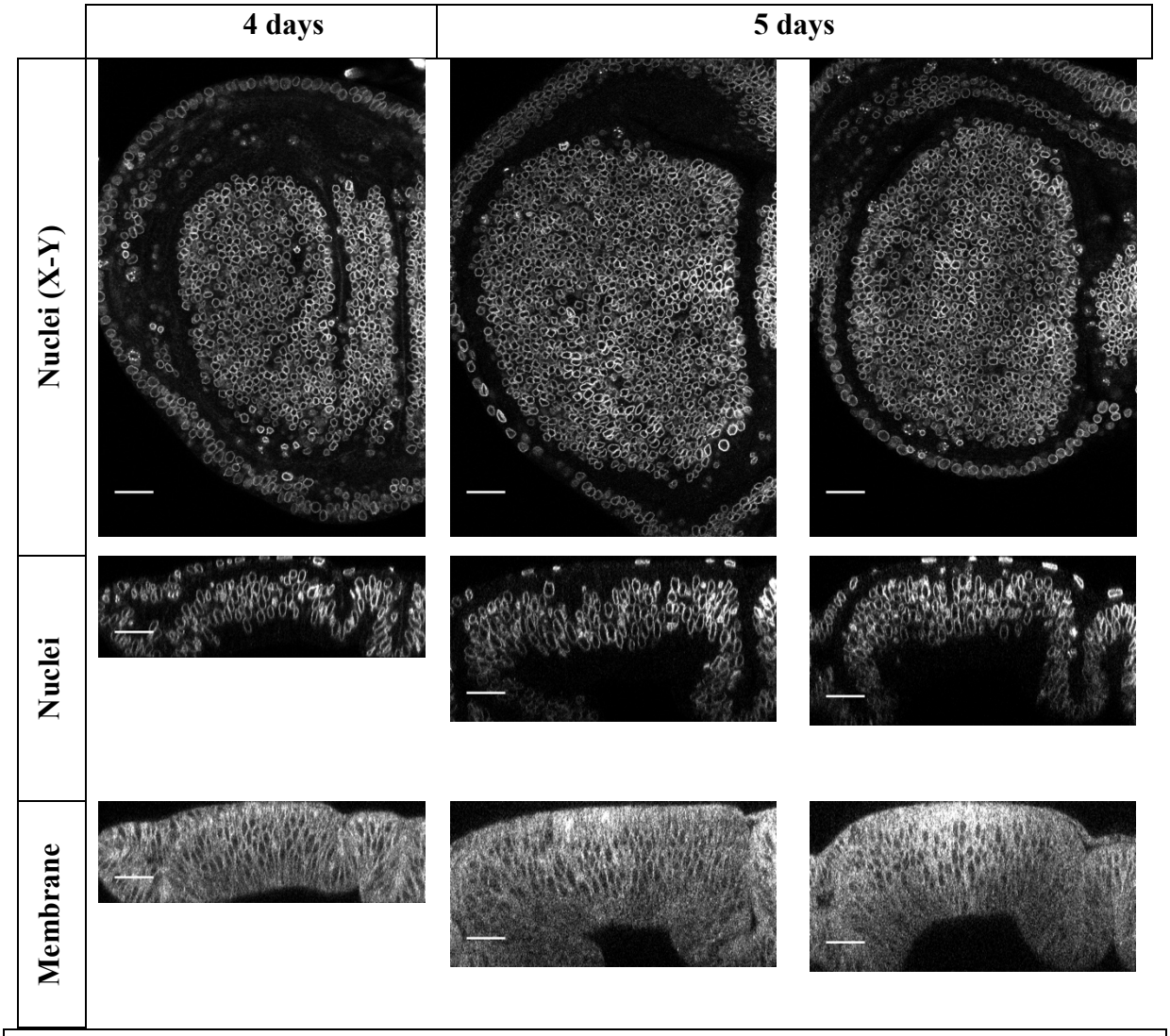
Supplementary Figure 6: Examples of construct and anti-body stained discs. Tubulin-Myristoylated-mCherry-2A-Citrine-Lamin/TM3 +/- anti-Lamin.



Supplementary Figure 7: Examples of Vectashield, FocusClear only and FocusClear kit. Tubulin-Myristoylated-mCherry-2A-Citrine-Lamin/TM3.



Supplementary Figure 8: Examples of photobleaching after acquiring a narrow stack. Tubulin-Myristoylated-mCherry-2A-Citrine-Lamin/TM3.



Supplementary Figure 9: Remaining wing imaginal discs of the repeated time-course.